Defense Threat Reduction Agency
8725 John J. Kingman Road, MS 6201
Fort Belvoir, VA 22060-6201

DTRA-TR-14-38

TECHNICAL REPORT

Composite-Nanoparticles Thermal History Sensors

Approved for public release; distribution is unlimited.

May 2014

HDTRA1-10-1-0001

Gang Chen and
Zhifeng Ren

Prepared by:
Massachusetts Institute of Technology
77 Massachusetts Avenue
Cambridge, MA 02139

DESTRUCTION NOTICE:

Destroy this report when it is no longer needed.
Do not return to sender.

PLEASE NOTIFY THE DEFENSE THREAT REDUCTION AGENCY, ATTN: DTRIAC/ J9STT, 8725 JOHN J. KINGMAN ROAD, MS-6201, FT BELVOIR, VA 22060-6201, IF YOUR ADDRESS IS INCORRECT, IF YOU WISH THAT IT BE DELETED FROM THE DISTRIBUTION LIST, OR IF THE ADDRESSEE IS NO LONGER EMPLOYED BY YOUR ORGANIZATION.

REPORT DOCUMENTATION PAGE

Form Approved
OMB No. 0704-0188

1. REPORT DATE *(DD-MM-YYYY)*	**2. REPORT TYPE**	**3. DATES COVERED** *(From - To)*
00-05-2014	Technical	Feb. 22, 2010 - May 21, 2013

4. TITLE AND SUBTITLE

Composite-Nanoparticles Thermal History Sensors

5a. CONTRACT NUMBER

5b. GRANT NUMBER
HDTRA1-10-1-0001

5c. PROGRAM ELEMENT NUMBER

6. AUTHOR(S)

Gang Chen (MIT) and Zhifeng Ren (Univ. of Houston)

5d. PROJECT NUMBER

5e. TASK NUMBER

5f. WORK UNIT NUMBER

7. PERFORMING ORGANIZATION NAME(S) AND ADDRESS(ES)

Massachusetts Institute of Technology
77 Massachusetts Avenue
Cambrudge, MA 02139

Department of Physics and TcSUH
University of Houston
Houston, TX 77204

8. PERFORMING ORGANIZATION REPORT NUMBER

9. SPONSORING / MONITORING AGENCY NAME(S) AND ADDRESS(ES)

Defense Threat Reduction Agency
8725 John J. Kingman Road STOP 6201
Fort Belvoir, VA 22060
PM/Suhithi Peiris

10. SPONSOR/MONITOR'S ACRONYM(S)

DTRA

11. SPONSOR/MONITOR'S REPORT NUMBER(S)

DTRA-TR-14-38

12. DISTRIBUTION / AVAILABILITY STATEMENT

Approved for public release; distribution is unlimited.

13. SUPPLEMENTARY NOTES

14. ABSTRACT

In the three years of this grant, thermal history dependences of the photoluminescence spectrum of several types of core-shell quantum dots (QDs) were studied as well as structural determination on transmission electron microscopy (TEM). These quantum dots (QDs) were studied in a broad temperature range from room temperature to over 500 degrees Celsius. Photoluminescnece (PL) of core/shell CdSe/ZnS QDs in different sizes was used as a tool to examine their interfacial mass diffusion processes due to temperature change. The PL of core/shell CdSe/ZnS QDs in size of ~5 nm shows strong dependence on their temperature history. The PL signal could be detected after QD samples were heated up to 500 degrees Celsius in a time frame of seconds. The blue-shift of the PL spectra with increasing temperature and heating time provides an optical route to read out the thermal history. A quantitative relationship between peak-shift and heating temperature has been established on CdSe QDs. We showed that the heating history can be read out by the combination of two kinds of quantum dots.

15. SUBJECT TERMS

nanostructure, photoluminescence, temperature, agent-defeat, spectrum

16. SECURITY CLASSIFICATION OF:			**17. LIMITATION OF ABSTRACT**	**18. NUMBER OF PAGES**	**19a. NAME OF RESPONSIBLE PERSON**
a. REPORT	**b. ABSTRACT**	**c. THIS PAGE**	SAR		Suhithi Peiris
Unclassified	Unclassified	Unclassified			**19b. TELEPHONE NUMBER** *(include area code)* 703-767-4732

CONVERSION TABLE

Conversion Factors for U.S. Customary to metric (SI) units of measurement.

MULTIPLY →	BY →	TO GET
← TO GET	← BY	← DIVIDE
angstrom	1.000 000 x E -10	meters (m)
atmosphere (normal)	1.013 25 x E +2	kilo pascal (kPa)
bar	1.000 000 x E +2	kilo pascal (kPa)
barn	1.000 000 x E -28	meter^2 (m^2)
British thermal unit (thermochemical)	1.054 350 x E +3	joule (J)
calorie (thermochemical)	4.184 000	joule (J)
cal (thermochemical/cm^2)	4.184 000 x E -2	mega joule/m^2 (MJ/m^2)
curie	3.700 000 x E +1	*giga bacquerel (GBq)
degree (angle)	1.745 329 x E -2	radian (rad)
degree Fahrenheit	$t_k = (t^\circ f + 459.67)/1.8$	degree kelvin (K)
electron volt	1.602 19 x E -19	joule (J)
erg	1.000 000 x E -7	joule (J)
erg/second	1.000 000 x E -7	watt (W)
foot	3.048 000 x E -1	meter (m)
foot-pound-force	1.355 818	joule (J)
gallon (U.S. liquid)	3.785 412 x E -3	meter^3 (m^3)
inch	2.540 000 x E -2	meter (m)
jerk	1.000 000 x E +9	joule (J)
joule/kilogram (J/kg) radiation dose absorbed	1.000 000	Gray (Gy)
kilotons	4.183	terajoules
kip (1000 lbf)	4.448 222 x E +3	newton (N)
kip/inch^2 (ksi)	6.894 757 x E +3	kilo pascal (kPa)
ktap	1.000 000 x E +2	newton-second/m^2 ($N-s/m^2$)
micron	1.000 000 x E -6	meter (m)
mil	2.540 000 x E -5	meter (m)
mile (international)	1.609 344 x E +3	meter (m)
ounce	2.834 952 x E -2	kilogram (kg)
pound-force (lbs avoirdupois)	4.448 222	newton (N)
pound-force inch	1.129 848 x E -1	newton-meter (N-m)
pound-force/inch	1.751 268 x E +2	newton/meter (N/m)
pound-force/foot^2	4.788 026 x E -2	kilo pascal (kPa)
pound-force/inch^2 (psi)	6.894 757	kilo pascal (kPa)
pound-mass (lbm avoirdupois)	4.535 924 x E -1	kilogram (kg)
pound-mass-foot^2 (moment of inertia)	4.214 011 x E -2	kilogram-meter^2 ($kg-m^2$)
pound-mass/foot^3	1.601 846 x E +1	kilogram-meter^3 (kg/m^3)
rad (radiation dose absorbed)	1.000 000 x E -2	**Gray (Gy)
roentgen	2.579 760 x E -4	coulomb/kilogram (C/kg)
shake	1.000 000 x E -8	second (s)
slug	1.459 390 x E +1	kilogram (kg)
torr (mm Hg, 0^0 C)	1.333 22 x E -1	kilo pascal (kPa)

*The bacquerel (Bq) is the SI unit of radioactivity; 1 Bq = 1 event/s.

**The Gray (GY) is the SI unit of absorbed radiation.

Table of Content

Objectives

This project aims at developing composite nanostructure-based (core-shell nanoparticles, heterostructure nanowires, and nano-flakes) temperature history sensors for recording the thermal environment that biological agent simulants experience during the testing of agent-defeat weapons. Such nanocomposite nanostructures transform the time-dependent temperature environment into the spatial mass-diffusion profile that can be interrogated after the experiment. The nanostructures are chosen so that they can be attached to bio-agent simulant during the experiments without interfering with their functionality. Tasks include developing the composite nanostructure synthesis method, the mass-diffusion diagnosis method, analytical tools that map the mass-diffusion profile into temperature history.

Status of effort

During the time period of February 22, 2010 to May 21 2013, thermal history dependences of the photoluminescence spectrum of several types of core-shell quantum dots (QDs) were studied as well as structural determination on transmission electron microscopy (TEM). These quantum dots (QDs) were studied in a broad temperature range from room temperature to over 500 °C. Photoluminescence (PL) of core/shell CdSe/ZnS QDs in different sizes was used as a tool to exam their interfacial mass diffusion processes due to the temperature change.

The PL of core/shell CdSe/ZnS QDs in size of ~5 nm shows strong dependence on their temperature history. The PL signal could be detected after QD samples were heated up to 500 °C in a time frame of seconds. The blue-shift of the PL spectra with increasing temperature and heating time provides an optical route to read out the thermal history. A quantitative relationship between peak-shift and heating temperature has been established on CdSe QDs. We showed that the heating history can be read out by the combination of two kinds of quantum dots.

Accomplishments

In the past three years, our efforts have been geared towards two directions. One is the quantitative relationship between PL spectrum and heating temperature to investigate the thermal history of the quantum dots, such as the temperature dependence of PL peak of quantum dots. The other is the quantitative optical study to develop a relatively simple readout mechanism of the thermal history. Optical studies using photoluminescence technique is to characterize nanoparticles and link their optical properties to their structure and structural changes. The characteristics of PL peak shift can be described by simple models that link to the thermal mass diffusion. With ~5 nm sized QDs, the sensitivity of heating has been tested on QDs with a diameter of 5 nm in tens of milliseconds with temperature up to about 500 °C.

1. Fast heating of quantum dots

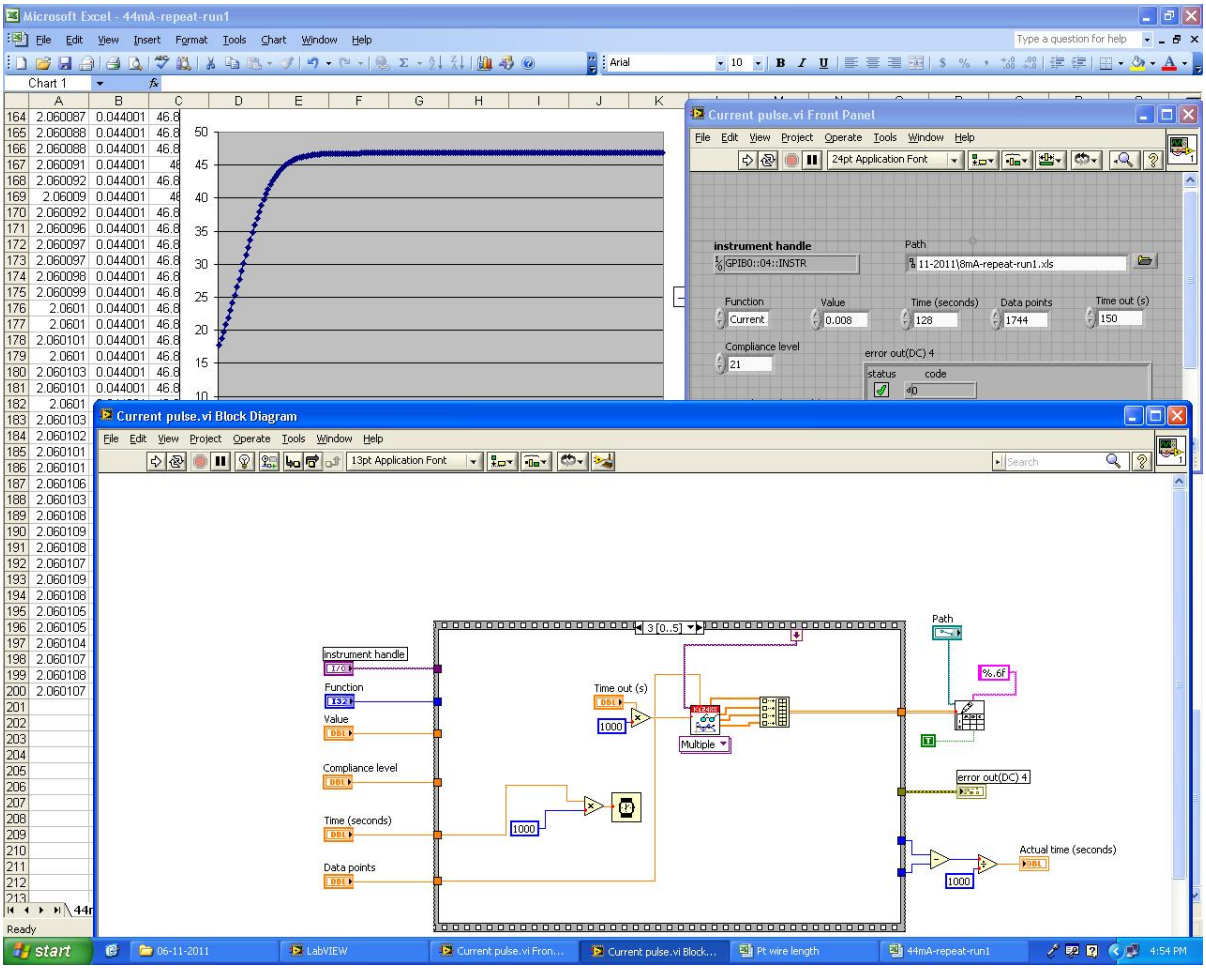

***Figure 1-1**. Labview VI to fast heat QDs.*

In order to simulate the thermal heating of an explosive, quantum dots were fast heated on Pt hotwires. A programed Labview VI was used to control a pulsed electric current (DC) and the duration, as shown in Figure 1-1. We programed and improved the Labview VI to record all the heating process, including the heating ramp up, holding, and cooling down. The fast heating procedures were more accurately controlled and recorded.

The quantum dots were deposited on Pt hotwires first. When a DC current was passing through the hotwire, the quantum dots were fast heated for a certain time. In all heating experiments, the Pt hotwires were heated by a pulsed DC current (the heating time is 0.5 s - 128 s) in air. The temperature of the Pt hotwires was measured from the electrical resistance of the Pt hotwires. All the heating parameters, such as the applied DC current, applied electric voltage, and electric resistance of the Pt wires, heating time, were recorded by the Labview VI.

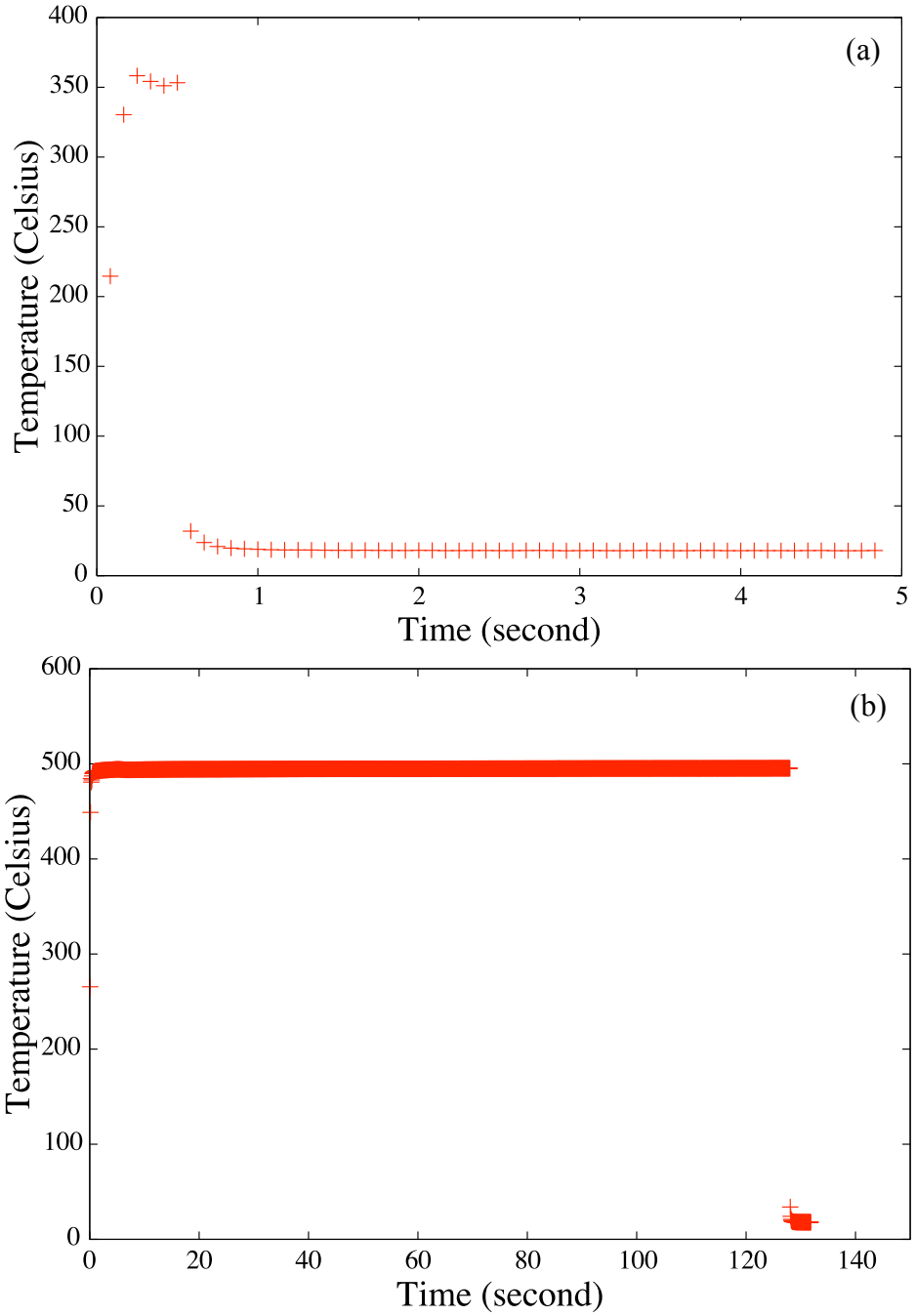

***Figure 1-2**. Temperature-time curve of a pulsed fast heating in air. (a) Temperature: 350 °C; Heating duration: 0.5 s. (b) Temperature: 500 °C; Heating duration: 128 s.*

The temperature ramp up time of the Pt hotwire is on the order of several tens of milliseconds (Figure 1-2). The temperature could cool down to room temperature in several milliseconds. Compared with the whole heating events, such as several seconds in laboratory or even longer in explosions, the ramp time and cooling time can be ignored during the overall temperature measurements.

2. Photoluminescence measurements of CdSe quantum dots

In order to measure the photoluminescence (PL) spectrum of the heated quantum dots accurately, we measured the photoluminescence spectrum under a weak laser. The obtained data were repeatable.

2.1. Experimental setup of photoluminescence measurements

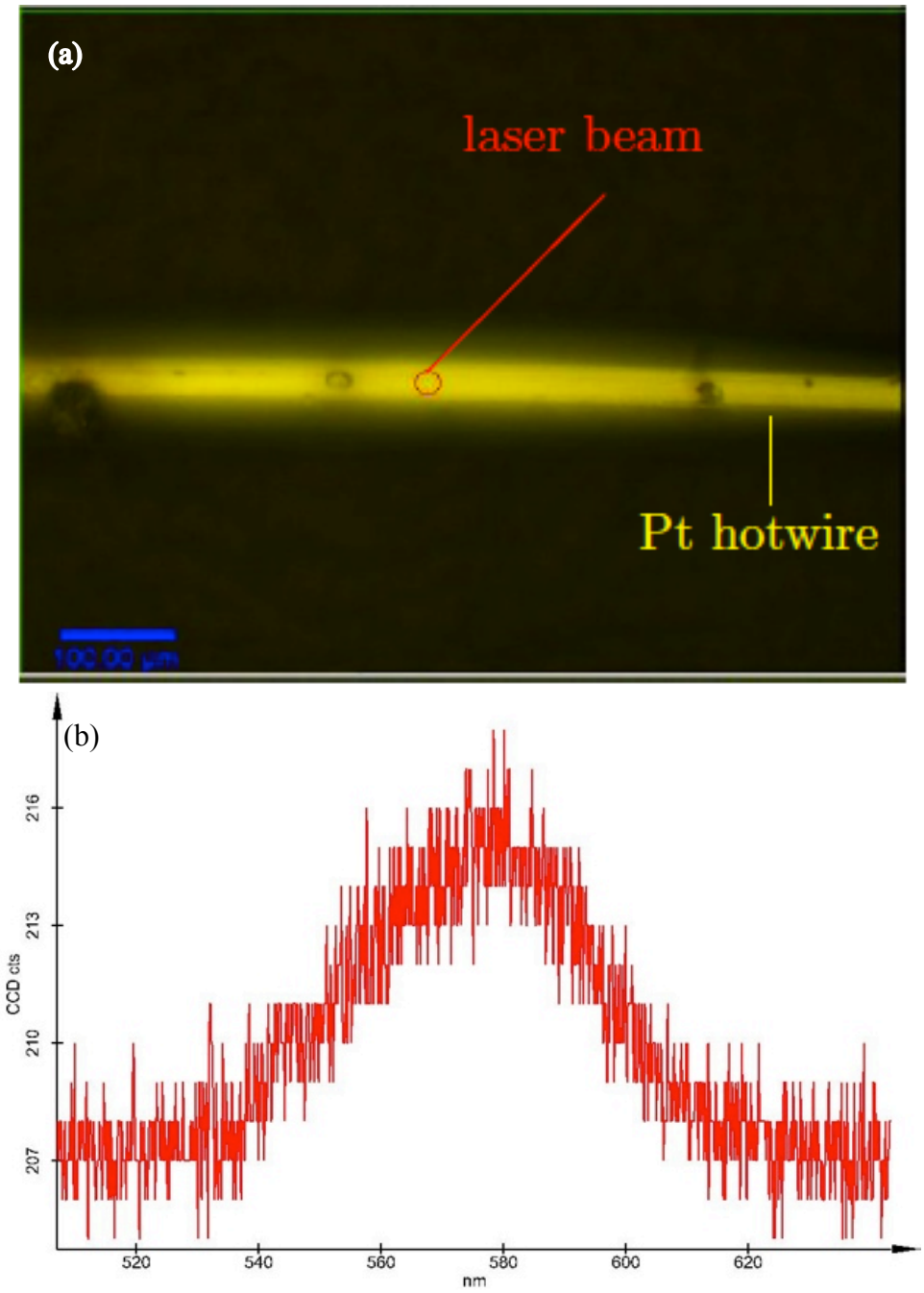

Figure 2-1. *(a) Optical image of a Pt hotwire deposited with QDs. (b) PL spectrm of QDs deposited on Pt hotwires.*

Figure 2-1a shows an optical image of a Pt hotwire during photoluminescence measurements. A weak laser beam was focused on the Pt hotwire surface to activate the photoluminescence spectrum. Figure 2-1b is a typical PL spectrum of CdSe quantum dots. In order to limit the heating effect of laser irradiation, the laser intensity was kept as low as possible while a PL peak is measurable. In our experiments, the PL peak intensity is controlled between 250 counts and 210 counts while the background intensity is about 207 counts.

2.2. Laser irradiation effect of photoluminescence measurements

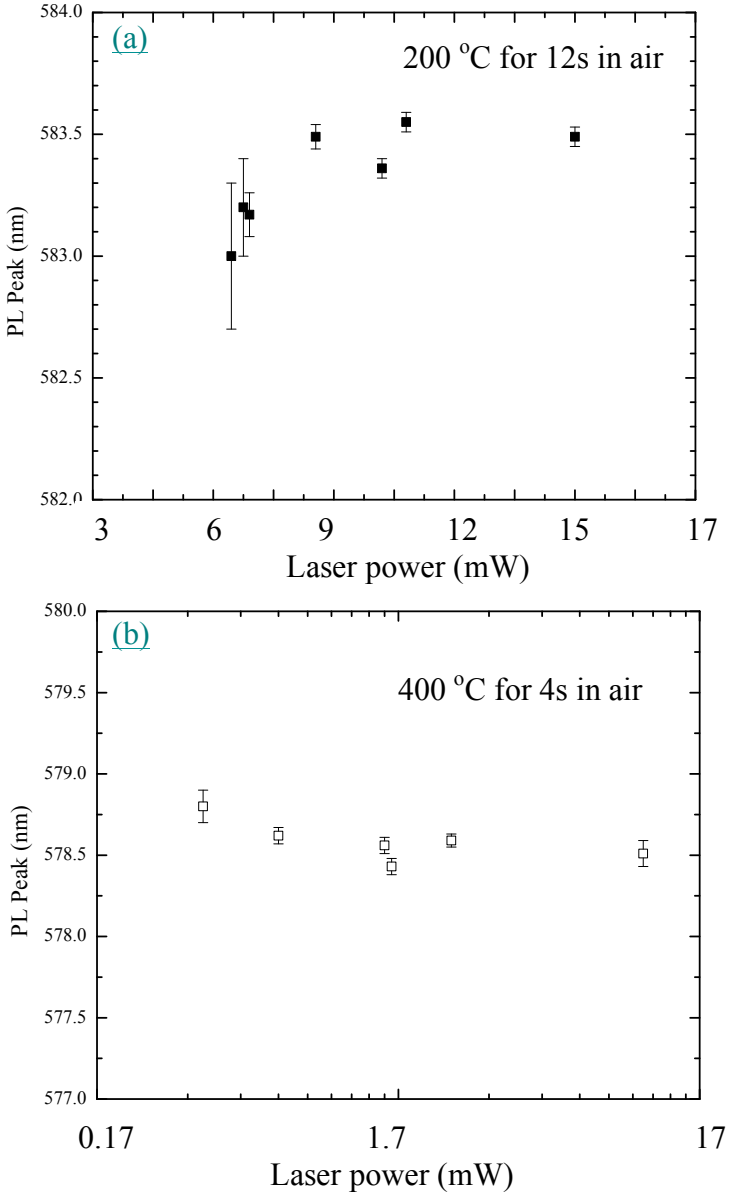

Figure 2-2. *PL peak at various measurement conditions. (a) QDs were heated at 200 °C for 128 s in air. (b) QDs were heated at 400 °C for 4 s in air.*

It was reported that the laser irradiation during PL measurement heated the samples and affected PL peak positions. In our experiments, the laser heating effect would also affect PL peak positions, causing the PL peak position unrepeatable. In order to accurately control the experimental parameters and obtain repeatable data, we studied how the intensity of laser and the measurement time affect PL peak positions.

In order to achieve the goal, we measured PL of QDs at weak laser intensity. The effect of laser irradiation was controlled and minimized. Below we show that the PL measurements do not affect PL spectrum during our measurements. First, we measured PL spectrum at a certain integration time. Figure 2-2 shows PL peaks of two heated QD samples. The laser intensity was manually controlled from 0 mW to 17 mW. PL measurements indicated the PL peak position is a constant with laser intensity. This means that the effect of laser irradiation is below our PL measurement errors of 1 cm^{-1}. Therefore the used laser power is low enough not to affect our experimental resolution.

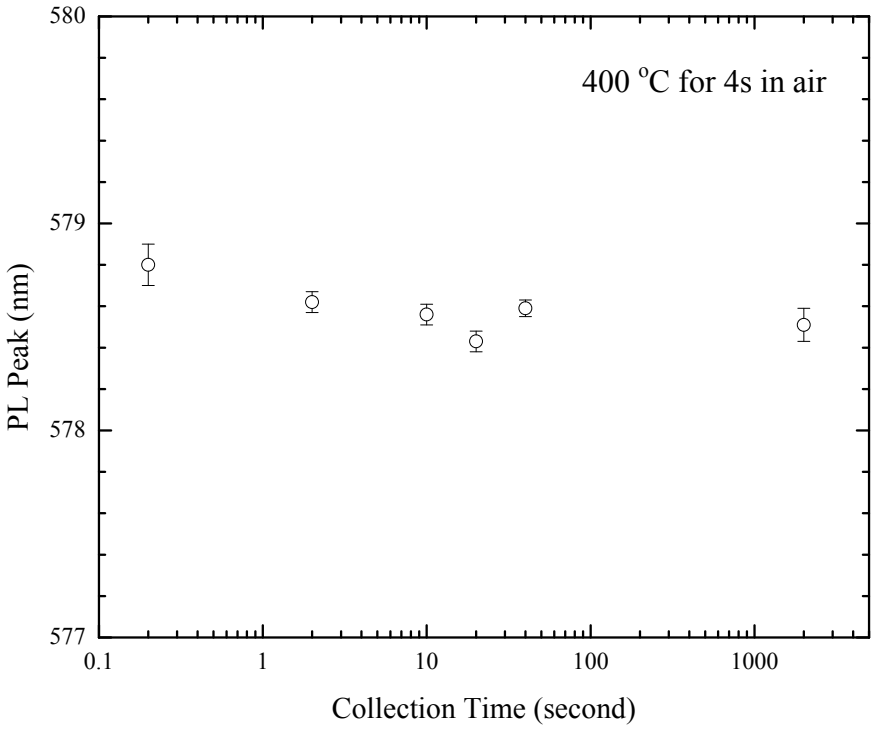

Figure 2-3. *Effect of integration time on PL peak. QDs were heated at 400 °C for 4 s in air.*

At the same time, we decreased the laser intensity as low as possible (PL peak count is about 250) and measured PL spectrum at different integration time. The PL peak position is independent on the measurement time when the PL integration time is 0.2 - 2000 seconds, as shown in Figure 2-3.

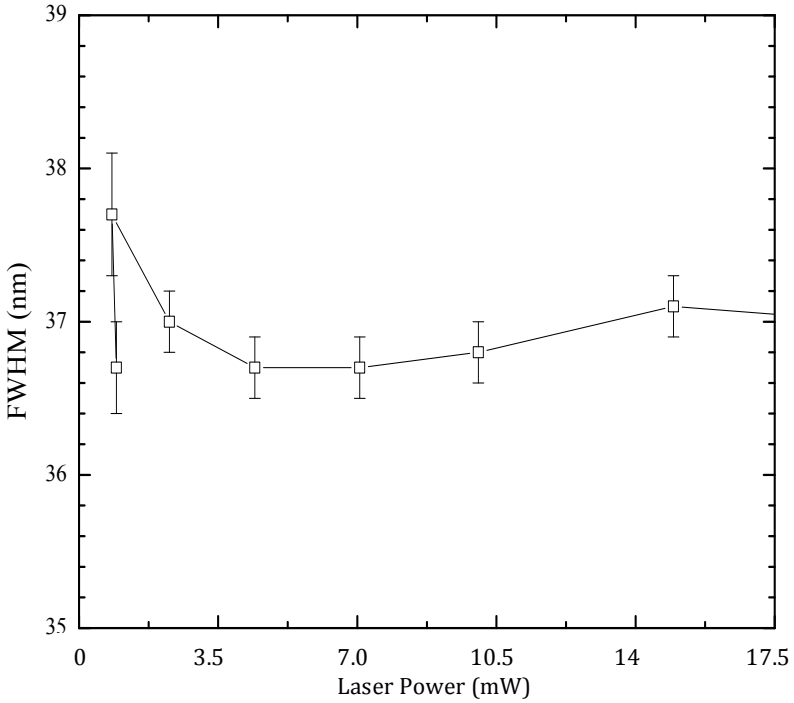

Figure 2-4. *Laser power effect on FWHM.*

We analyzed the full-width-at-half-maximum (FWHM) of the PL peaks measured at a series of measurement conditions. Figure 2-4 plots the FWHM under different laser power. FWHM is independent on the laser power either.

Therefore based on our experimental setup, the heating effect of laser can be ignored in all of our experiments. In order to avoid any potential effect of laser heating effects, we still chose a weak laser intensity (~2 – 4 mW or less) and a short integration time (less than 1 second) in all of our PL measurements.

Additionally, PL spectra of heated QDs were measured at the center of the Pt hotwires to make sure that the PL signal comes from the uniformly heated QDs. Usually at least 3 - 5 PL spectra were collected from different locations of one Pt hotwire.

Based on the updated experimental setup, the PL data were very repeatable during the entire project.

3. PL spectra of CdSe QDs

From Feb 2010 to May 2013, PL of four kinds of core/shell CdSe/ZnS QDs in size of ~5 nm were measured and all these PL spectra showed a strong dependence on QDs' temperature history. The PL spectrum could be detected after samples were heated up to 800 ^{o}C in air. The

blue-shift of the PL spectra with increasing temperature and heating time provide optical routes to read out the thermal history.

3.1. PL spectra of QDs with peak wavelength of 620 nm

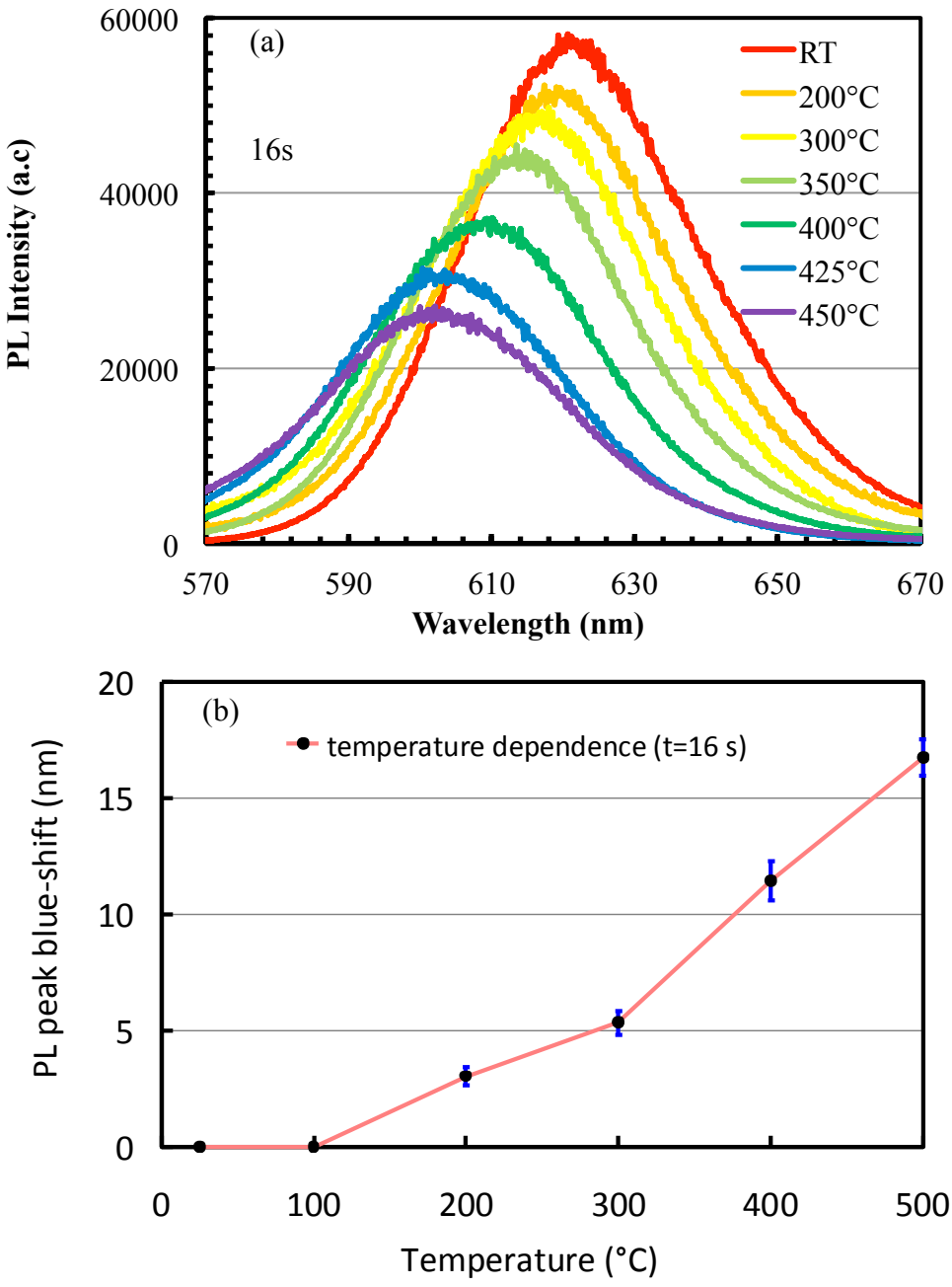

Figure 3-1. *PL spectra for heating on the timescale of seconds. (a) PL spectra with increasing temperature for heating event of 16s duration. There is a noticeable blue-shift in peak PL wavelength from 200 °C and above. (b) PL blue-shift as a function of heating temperature for CdSe/ZnS quantum dots. There is clear evidence that the PL peak wavelength blue-shifts with temperature.*

The PL peak of the 1st kind of QDs is 620 nm before being heated. Figure 3-1a shows the temperature dependent PL spectra of the QDs with peak wavelength of 620 nm after heating. The samples were heated on hotwires in ambient air, and quickly cooled down to room temperature in milliseconds. The spectra were measured at room temperature. A series of temperatures up to 450 ^{o}C were tested as indicated in the figure.

Figure 3-1b show the PL peak shift with heating temperature. The PL peak shift was the difference between PL peak wavelength of heated QDs and that of unheated QDs. The PL peaks shift to higher energy after QDs were heated. The higher heating temperature, the more shifts.

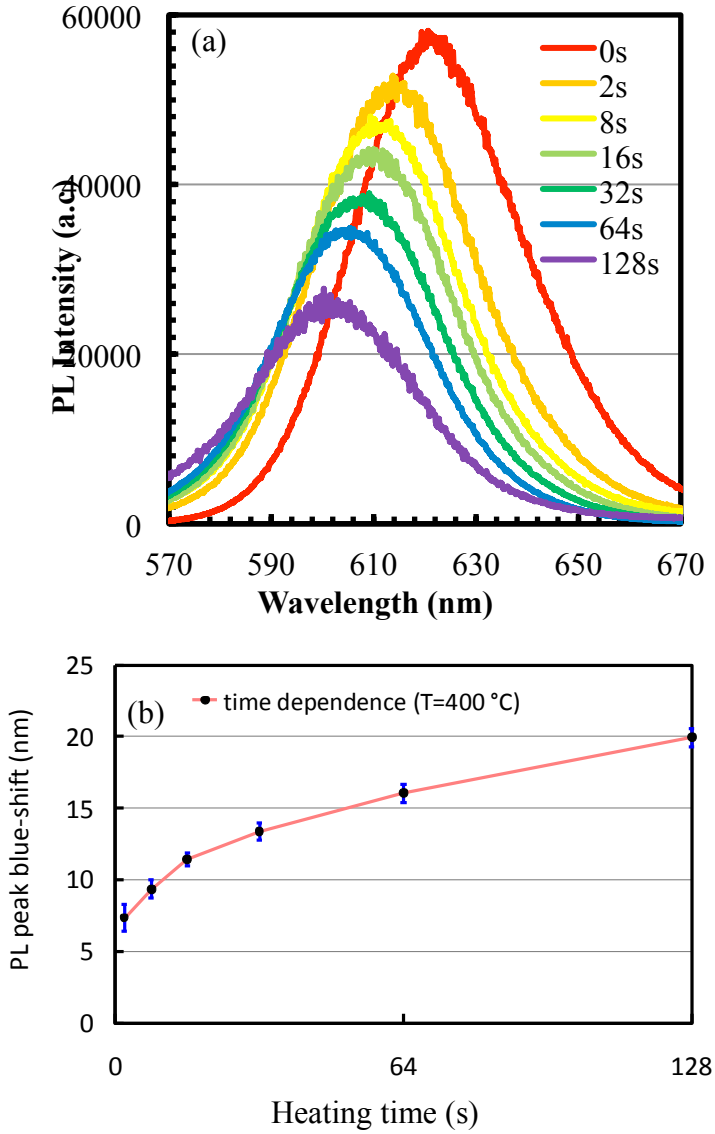

Figure 3-2. *(a) PL spectra with increasing heating time for temperature at 400 °C. There is a noticeable blue-shift in peak PL wavelength with increasing heating time. (b) PL blue-shift as a function heating time for CdSe/ZnS quantum dots. PL peak wavelength decreases with increasing annealing time.*

The PL shift also depends on heating time. Figure 3-2a shows PL spectra of heated QDs for different heating duration. The PL peak shifts with heating time, as shown in Figure 3-2b.

The relationship between confined band-gap energy of the 1st QDs with heating temperature, T, and heating time, t, can be expressed as

$$|\Delta E_g(T,t)| = \left[2\pi^2 \left(\frac{a_B^2}{a_1^3} \right) - 1.786 \left(\frac{a_B}{a_1^2} \right) \right] R_y^* \sqrt{D_{0,1}} \exp\left(-\frac{E_{0,1}}{2k_B T} \right) t^{n1} \qquad (3-1)$$

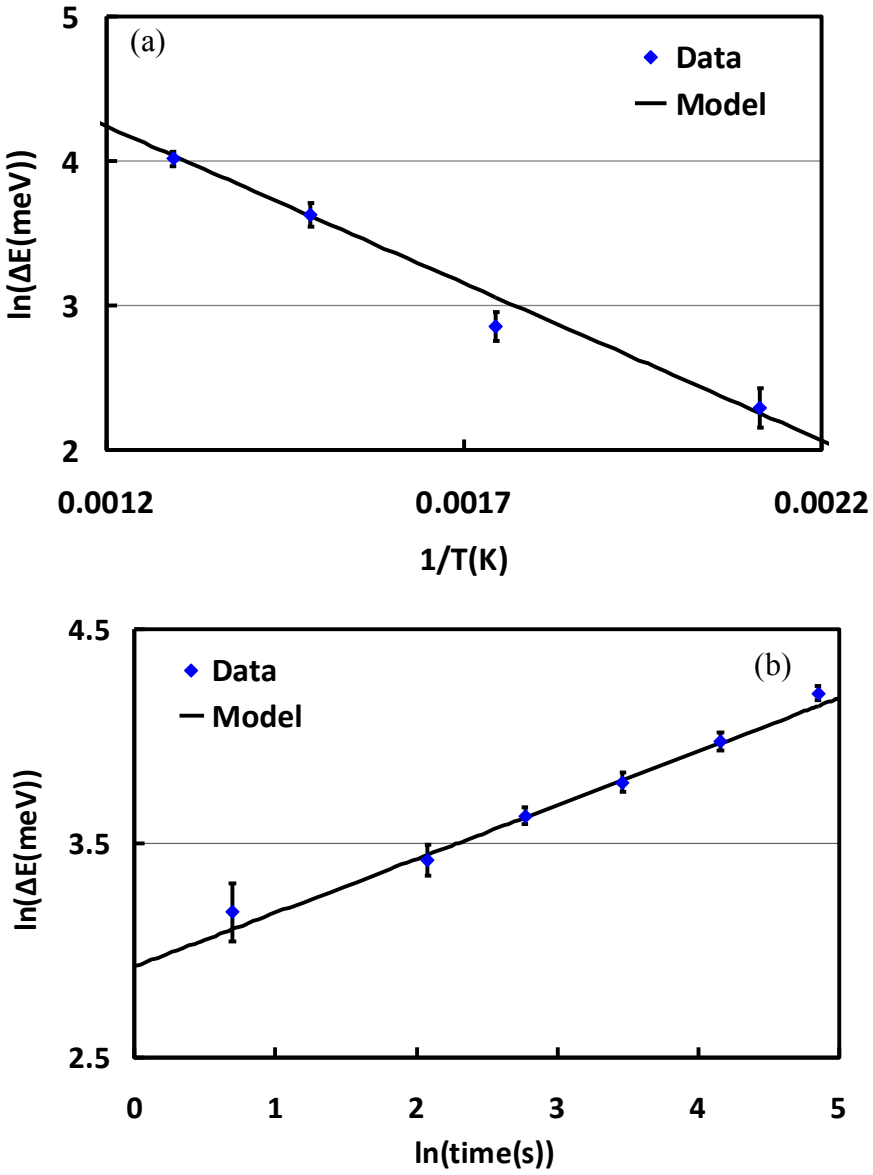

Figure 3-3. *PL blue-shift of 1st QDs. (a) ln(ΔE)-1/T. (b) ln(ΔE)-lnt.*

In order to experimentally detect the parameters a_1, $D_{0,1}$ and $E_{0,1}$, Figure 3-3 plots the relationship between the confined band-gap energy with heating temperature T and time t. From Figure 3-3, we obtained a_1 = 5.7 nm, $E_{0,1}$ = 0.375 eV, n_1 = 0.25 and $D_{0,1}$=7.55 × 10^{-20} m^2/s for the first kind of QDs.

3.2. PL spectra of QDs with peak wavelength of 576 nm

The wavelength of 2rd kind of QDs is 576 nm before heating. The QDs were deposited on hotwire as described before. The hotwires were then heated up to a certain temperature (from 200 ^{o}C to 500 ^{o}C) in less than 140 milliseconds, then kept at the temperature for a certain heating time (from 0.5 seconds to 128 seconds). The hotwires were cooled down to room temperature in less than 70 milliseconds. Such a fast heating is an ideal case to study the thermal effect on QDs.

Table 3-1. *Heated CdSe/ZnS QDs in air. The PL peak of the unheated QDs is 576 nm.*

Time (s)	0.5	1	2	4	8	16	32	64	128
500 °C	×	×	×	×	×	×	×	×	×
450 °C	×	×	×	×	×	×	×	×	×
400 °C	×	×	×	×	×	×	×	×	×
350 °C	×	×	×	×	×	×	×	×	×
300 °C	×	×	×	×	×	×	×	×	×
200 °C	×	×	×	×	×	×	×	×	×

Table 3-1 lists all the QDs heated in air at series of heating temperature and heating time. There are total 54 samples fast heated in air. Then PL spectra of these QDs were measured on a WiTEC Raman microscope.

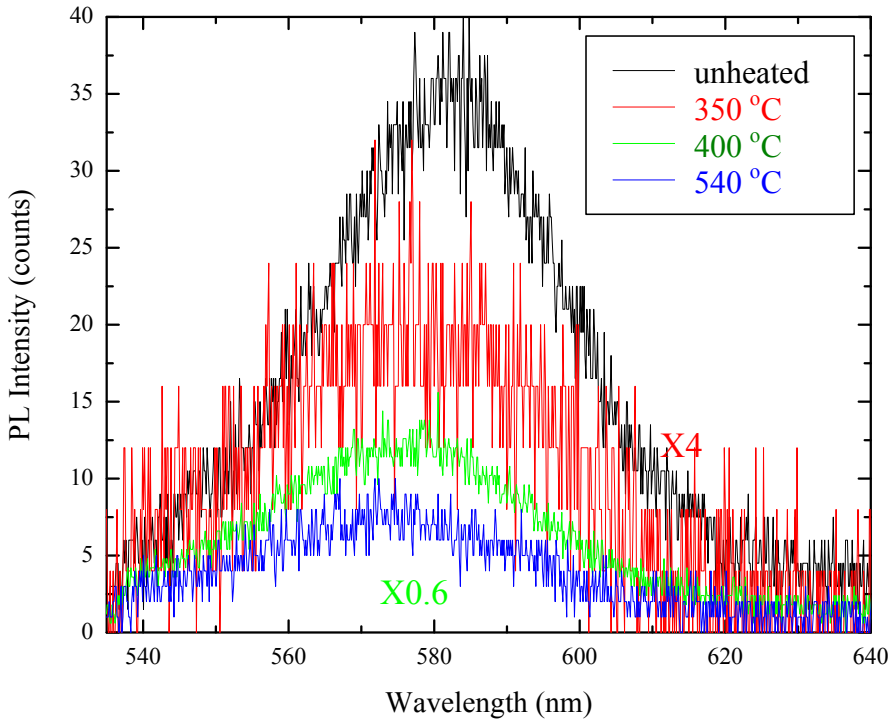

Figure 3-4. *PL spectra of QDs heated at different temperatures for 1 s. Each spectrum was recorded at room temperature. The PL peak wavelength of the unheated QDs is 576 nm.*

PL spectra of the fast heated QDs were measured under the measurement conditions discussed in Section 2. Figure 3-4 shows typical PL spectra of the CdSe QDs heated for 1 s in air. The spectra were measured after the samples were cooled to room temperature. A series of temperatures up to 450 °C were tested as indicated in the figure. PL signals were readily detectable with the heating temperature up to 450 °C. Below 150 °C, the PL peak wavelength changes very little. Between 150 - 450 °C, the PL peak exhibits a blue-shifting with increasing heating temperature. The PL peak shift provides the fingerprints of irreversible structural changes during the thermal exposure that the QDs experienced. The sensing range of the temperature depends on the size of QDs used. For this kind of QDs, the PL can be detected after 0.5 seconds heating up to 500 °C.

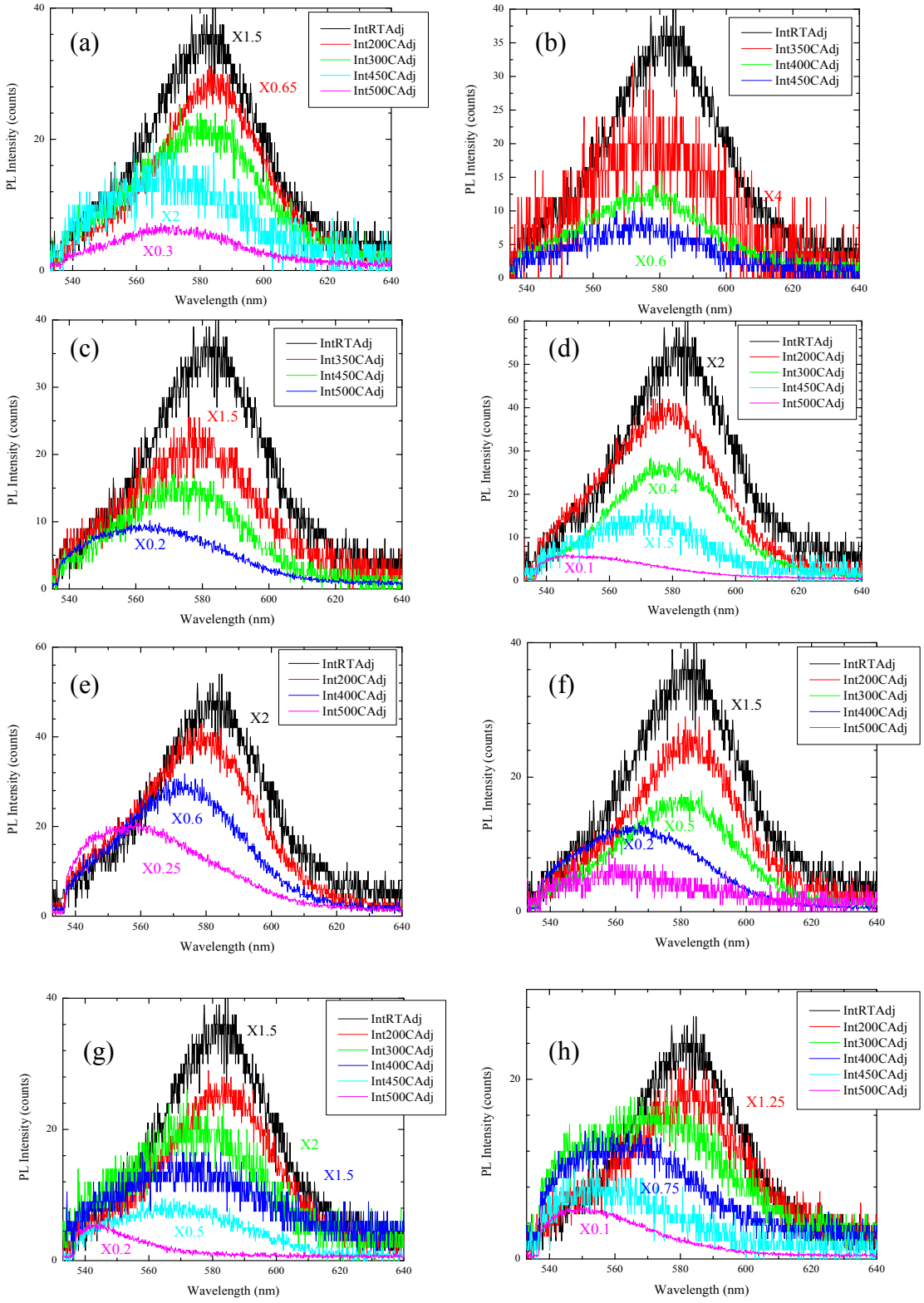

Figure 3-5. *PL spectrum of heated QDs in air. (a) 0.5 s. (b) 1 s. (c) 2 s. (d) 4 s. (e) 8 s. (f) 16 s. (g) 32 s. (h) 64 s.*

With the similar procedure in the temperature-dependent studies shown in Figure 3-4, Figure 3-5 shows PL spectrum of the 2nd QDs after heating for different heating times. A PL blue-shift with heating temperature was observed on all of these cases with different heating time.

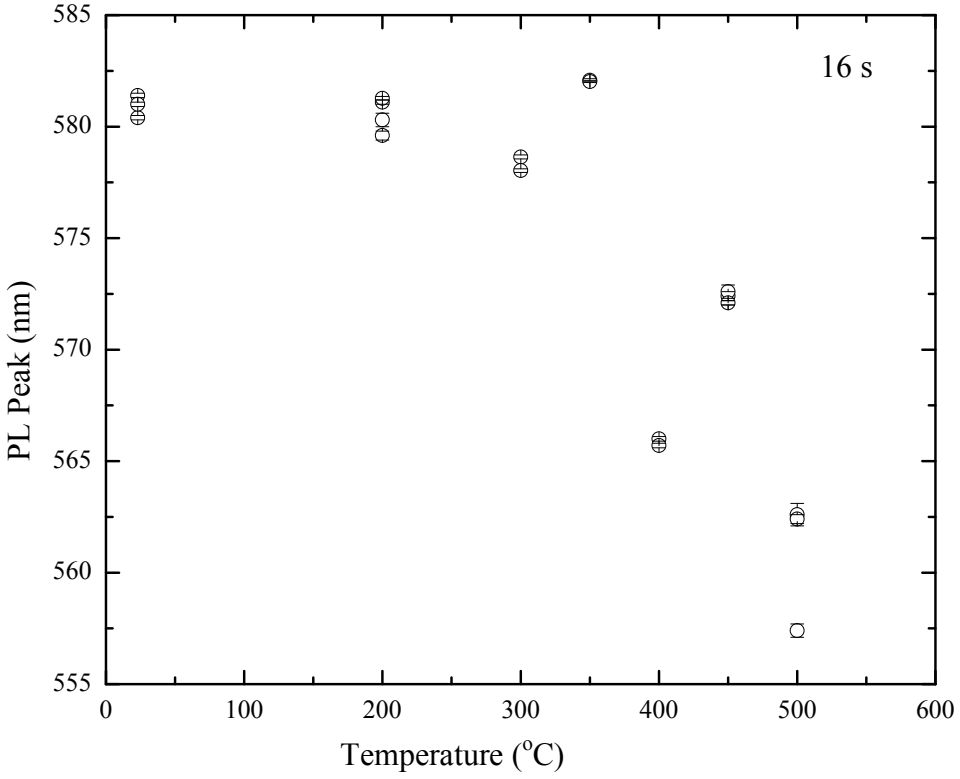

Figure 3-6. *PL blue-shift as a function of heating temperature T for the 2nd kind of CdSe/ZnS quantum dots. Heating time t = 16 s.*

There is clear evidence that the PL peak wavelength blue-shifts with heating temperature. Figure 3-6 shows a typical quantitative relationship between PL peak and heating temperature. The heating time was 16 s. The PL wavelength decreases sharply above 300 °C.

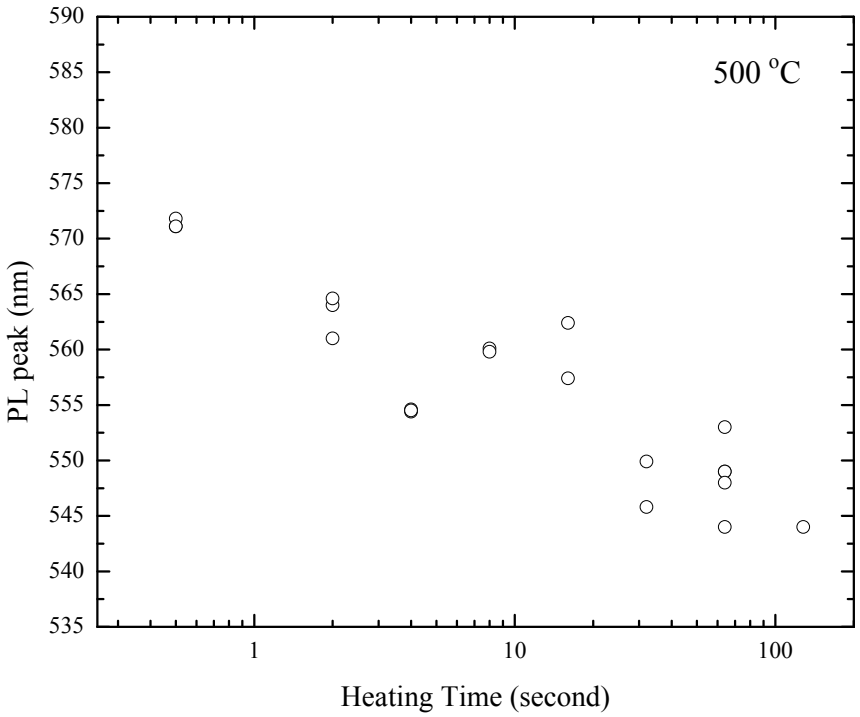

Figure 3-7. *PL blue-shift as a function of heating time for the 2nd CdSe/ZnS quantum dots. Heating temperature T = 500 °C.*

The heating time also affects the PL wavelength besides heating temperature. Figure 3-7 plots a typical relationship of PL peak wavelength and heating time when the heating temperature is 500 °C. The PL peak wavelength decreases with the heating time.

The PL peak wavelength shift could be ascribed to the confined quantum effects induced by a mass diffusion. The quantum confinement energy of a QD depends strongly on its size and the surrounding energy barrier. The thermal mass diffusion at the interface of the constituent materials induces the size and shape changes of the energy well and the barrier.

The temperature induced mass diffusion across the core and shell interface causes the core to shrink in size. Since the band-gap energy is a strong inverse function of the size, this results in an increase in the band-gap energy. The temperature (T) and time (t), dependent band-gap energy shift measured from PL spectra, $\Delta E(T,t)$, is calculated using the following relation:

$$|\Delta E(T,t)| = \left[2\pi^2 \left(\frac{a_B^2}{a^3} \right) - 1.786 \left(\frac{a_B}{a^2} \right) \right] R_y^* \sqrt{D_0} \exp\left(-\frac{E_0}{2k_B T} \right) t^n \qquad (3-2)$$

where a, a_B, n, E_0, D_0 and R_y are the radius of core, Bohr radius of CdSe, time exponent, mass diffusion energy barrier, diffusivity prefactor and Rydbergy constant for the quantum dot, respectively.

By performing the annealing time dependence at a set of temperatures, the history fingerprints

can be mapped out in a targeted sensing range of both temperature and time so that the time-temperature response of the QDs during heating processes can be fully characterized.

To determine E_0, D_0 and n of the 2nd QDs from the experimental data, we take the log on both sides of the equation (3-2). Now, assuming a constant temperature T_0, we obtain

$$\ln|\Delta E(T_0,t)|=n\ln t+A \qquad (3-3)$$

where A is a constant. This equation suggests that log of the energy shift, ln(ΔE), is a linear function of log of the time, ln$t$, with n as the slope of the plot.

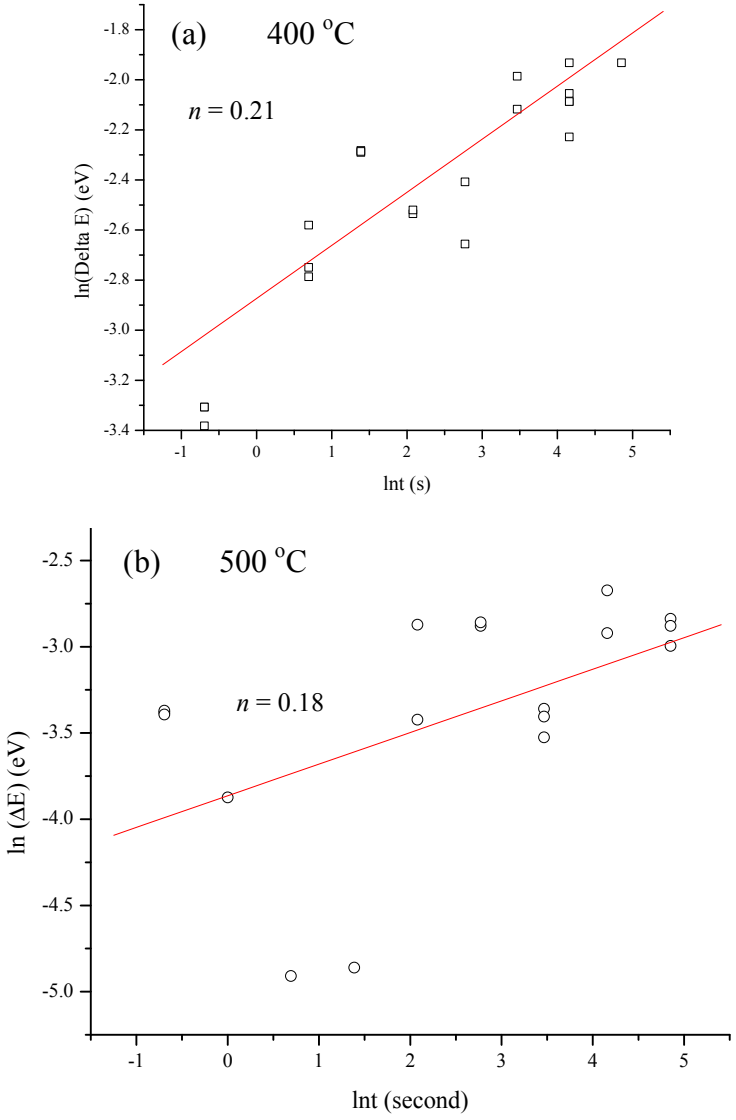

Figure 3-8. *Band-gap shift ln(ΔE) with time lnt for the 2nd kind of CdSe/ZnS quantum dots. The QDs were heated at (a) 400 °C and (b) 500 °C in air.*

Figure 3-8 plots $\ln|\Delta E(T_0,t)| - \ln t$ curve for the 2nd CdSe/ZnS quantum dots heated at 400 °C and 500 °C. From the fitting, the average time exponent n = 0.19.

Now, assuming a constant annealing time t_0:

$$\ln|\Delta E(T,t_0)| = -\frac{E_0}{2k_BT} + B \qquad (3-4)$$

where B is another constant. From this equation we find that log of the energy shift scales inversely to temperature T, with ($-E_0/2k_BT$) as the slope of the relationship.

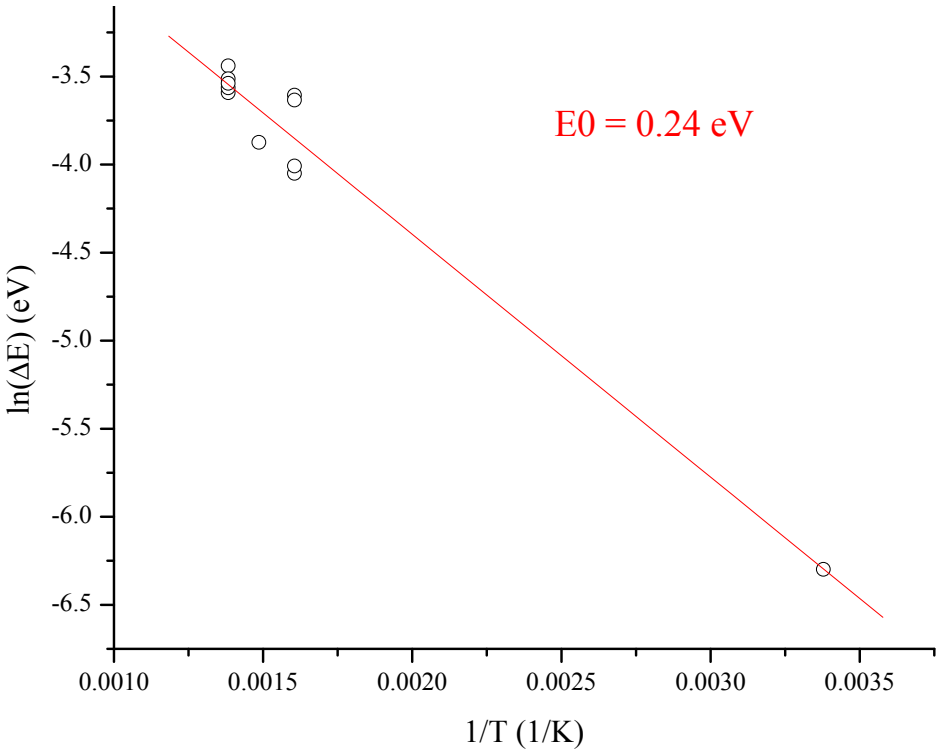

Figure 3-9. *Band-gap shift ln(ΔE) with inverse temperature 1/T for the 2nd kind of CdSe/ZnS QDs. t_0 = 1 s.*

Figure 3-9 plots $\ln\Delta E - 1/T$ curve for the 2nd kind of CdSe/ZnS quantum dots when the heating time t_0 is 1 s. From the fitting, E_0 = 0.24 eV.

Table 3-2. *E_0 of CdSe/ZnS QDs determined from fitting.*

Time t_0 (s)	*1*	*2*	*4*	*8*	*16*	*32*	*64*	*128*
E_0 (eV)	*0.24*	*0.26*	*0.28*	*0.24*	*0.24*	*0.31*	*0.45*	*0.33*

We conducted a similar study on Cd_xSe_{1-x}/ZnS quantum dots at other heating time t_0 from 0.5 s to 128 s. Table 3-2 lists E_0 fitted from the $\ln(\Delta E) - 1/T$ curves at other heating time. The diffusion energy E_0 is about 0.2 - 0.3 eV. The difference in the values of the parameter may be attributed to experimental error during the heating processing method. The average diffusion energy E_0 is 0.27 eV.

The diffusion prefactor D_0 is then calculated from the values of A and B. The best fits to the data give: $D_0 \sim 2.57 \times 10^{-18}$ m^2 s^{-1} for the 2nd kind of CdSe/ZnS QDs.

It is interesting to note that for a typical mass diffusion process, $n = 0.5$. However, for CdSe/ZnS core-shell quantum dots we find that n is much smaller, suggesting that the mass diffusion process is strongly dependent on the temperature and weakly dependent on the annealing time.

3.3. PL spectra of QDs with PL peak wavelength of 561 nm

Besides the first kind of QDs with original PL peak at 620 nm, second kind of QDs with original PL peak at 576 nm, we also investigated third kind of QDs with original PL peak at 561 nm. The third kind of QDs are also CdSe/ZnS core-shelled QDs. The size of the CdSe core is slightly smaller, resulting in a wider band-gap because of quantum refinement.

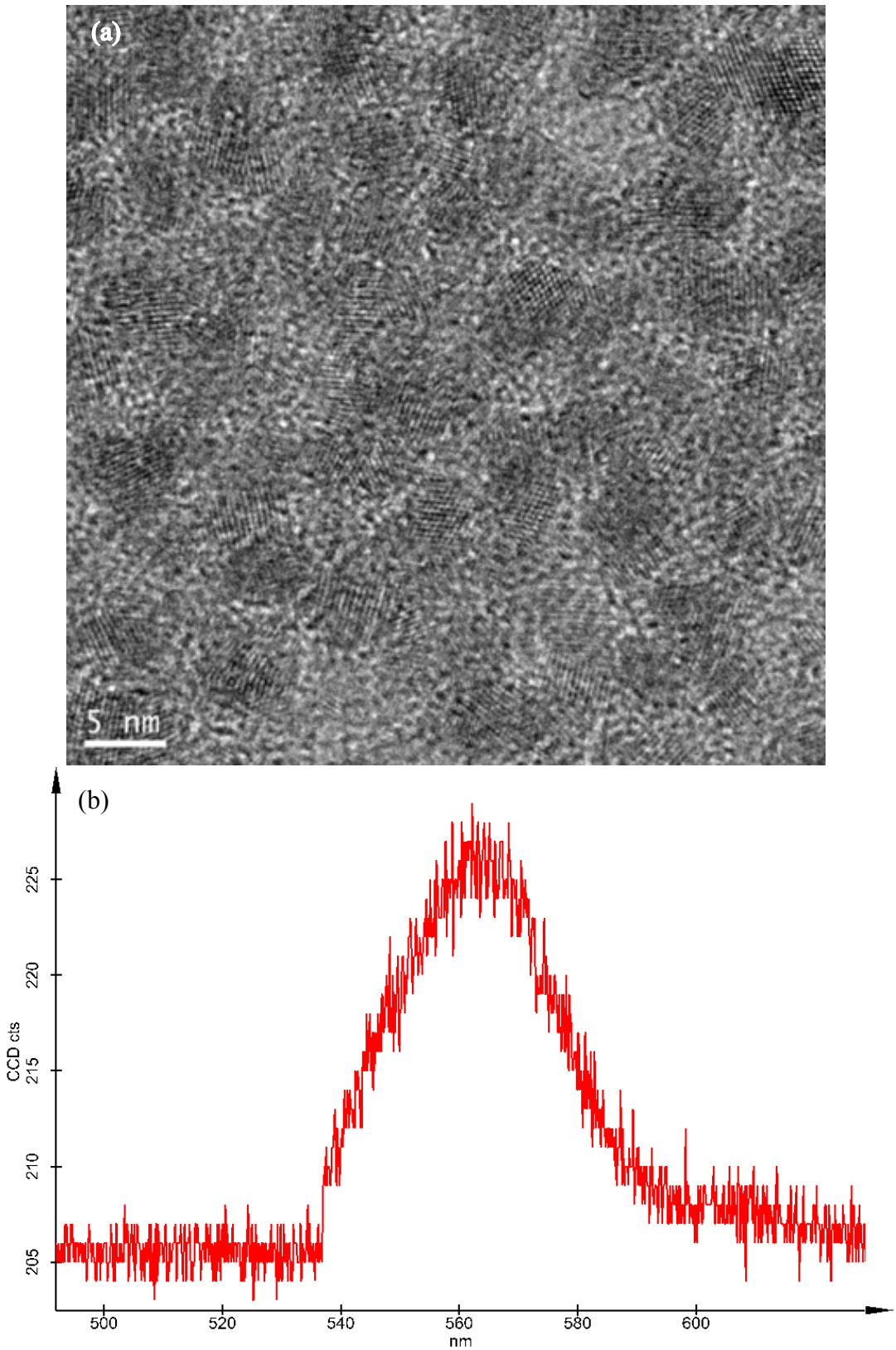

Figure 3-10. *Third kind of QDs. (a) HRTEM and (b) PL spectrum of unheated 3rd kind of QDs.*

Figure 3-10a shows an HRTEM image of the 3rd kind of QDs (3rd QDs). The unheated QDs are nanocrystals with diameter of ~4 nm. The PL peak of the unheated 3rd QDs is 561 nm, as shown in Figure 3-10b.

The 3rd kind of QDs were also deposited on hotwires, fast heated up to a certain heating temperature in air, kept at the temperature for a certain heating time. The hotwires were then cooled down to room temperature in less than 70 ms.

Table 3-3. *Heated CdSe/ZnS QDs in air. The PL peak of the unheated 3rd QDs is 561 nm.*

Time (s)	0.5	1	2	4	8	16	32	64	128
500 °C	×	×	×	×	×	×	×	×	×
400 °C	×	×	×	×	×	×	×	×	×
300 °C	×	×	×	×	×	×	×	×	×
200 °C	×	×	×	×	×	×	×	×	×

Table 3-3 lists all the heated 3rd kind of QDs that PL spectra were measured on. The PL spectra were measured at room temperature after the QDs were cooled down, as discussed in Section 2.

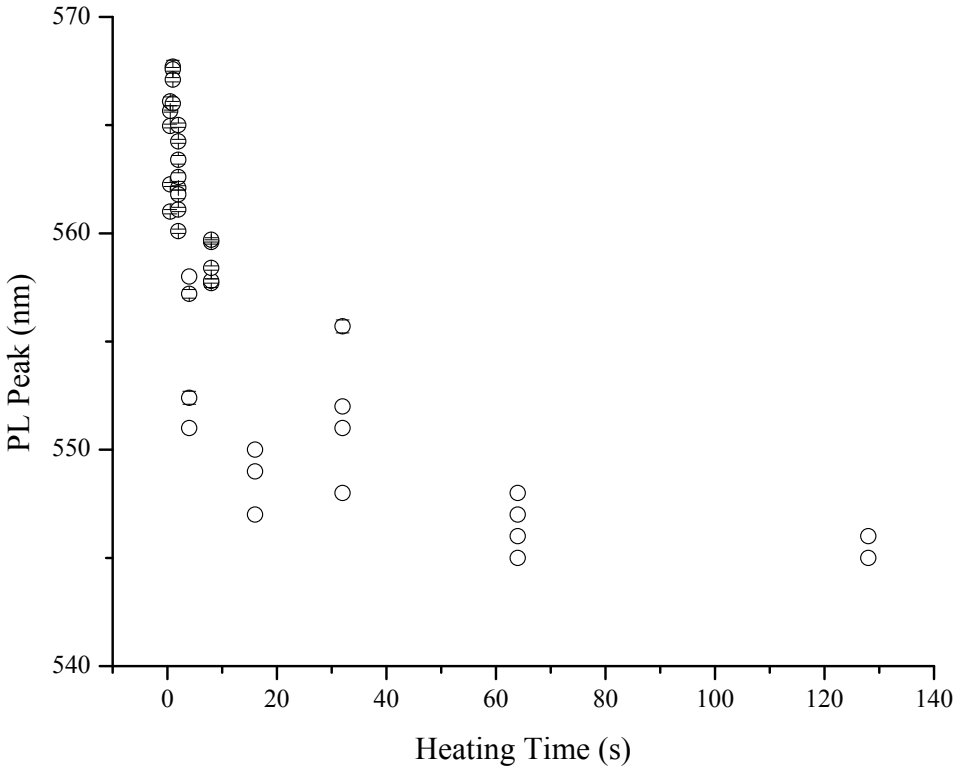

Figure 3-11. *PL blue-shift as a function of heating time t for the 3rd CdSe/ZnS quantum dots. Heating temperature T_0 = 400 °C.*

The PL peak also blue shift with heating temperature T and heating time t. Figure 3-11 shows the PL blue-shift with heating time t at a heating temperature T_0 of 400 ^{o}C. The PL peak wavelength decreases with the heating time. The similar behavior was observed at all other heating temperatures, such as 200 ^{o}C and 500 ^{o}C. All the spectra were measured at room temperature after the samples were cooled to room temperature.

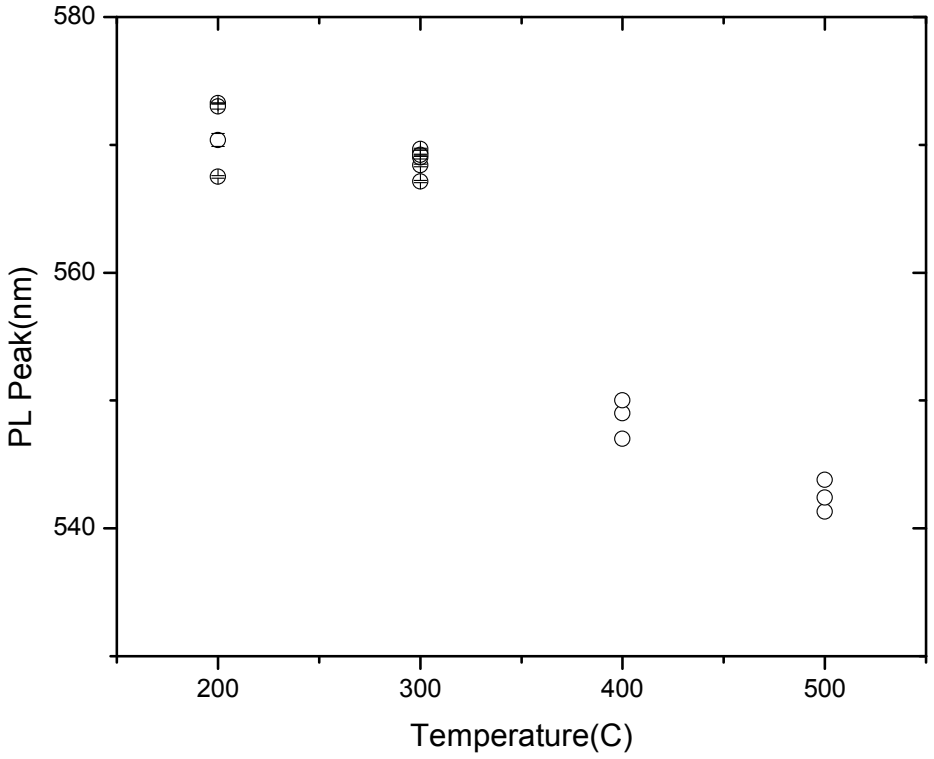

Figure 3-12. *PL blue-shift as a function of heating temperature T for the 3rd kind of CdSe/ZnS quantum dots. Heating time t_0 = 16 s.*

Figure 3-12 shows the PL peak blue shift with heating temperature T when heated for 16 s in air. The PL peak wavelength of the 3rd kind of QDs also decreases with heating temperature above 300 ^{o}C.

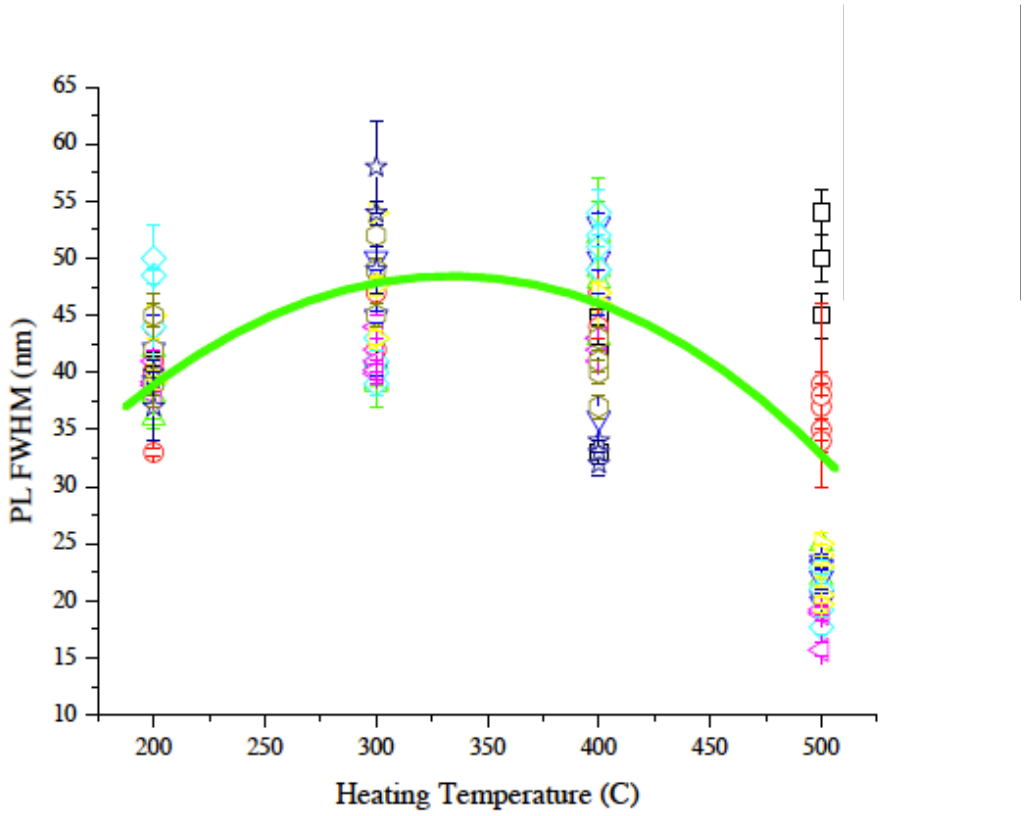

Figure 3-13. *FWHM of PL peak as a function of heating temperature for the 3rd kind of CdSe/ZnS quantum dots at various heating time.*

We also measured the FWHM of the heated 3rd kind of QDs. The data are plotted in Figure 3-13. The heating does not affect FWHM significantly. FWHM is related to the microstructure of the QDs, such as the defects in the core. Figure 3-13 implies that the microstructure of the QDs does not changed obviously, in agreement with the HRTEM study. The mass diffusion should be weak while be enough to affect PL peaks.

3.4. PL spectra of 4th kind of QDs with peak wavelength of 670 nm

We continuously examined 4th kind of QDs. The wavelength of the 4th kind of QDs is 670 nm before being heated.

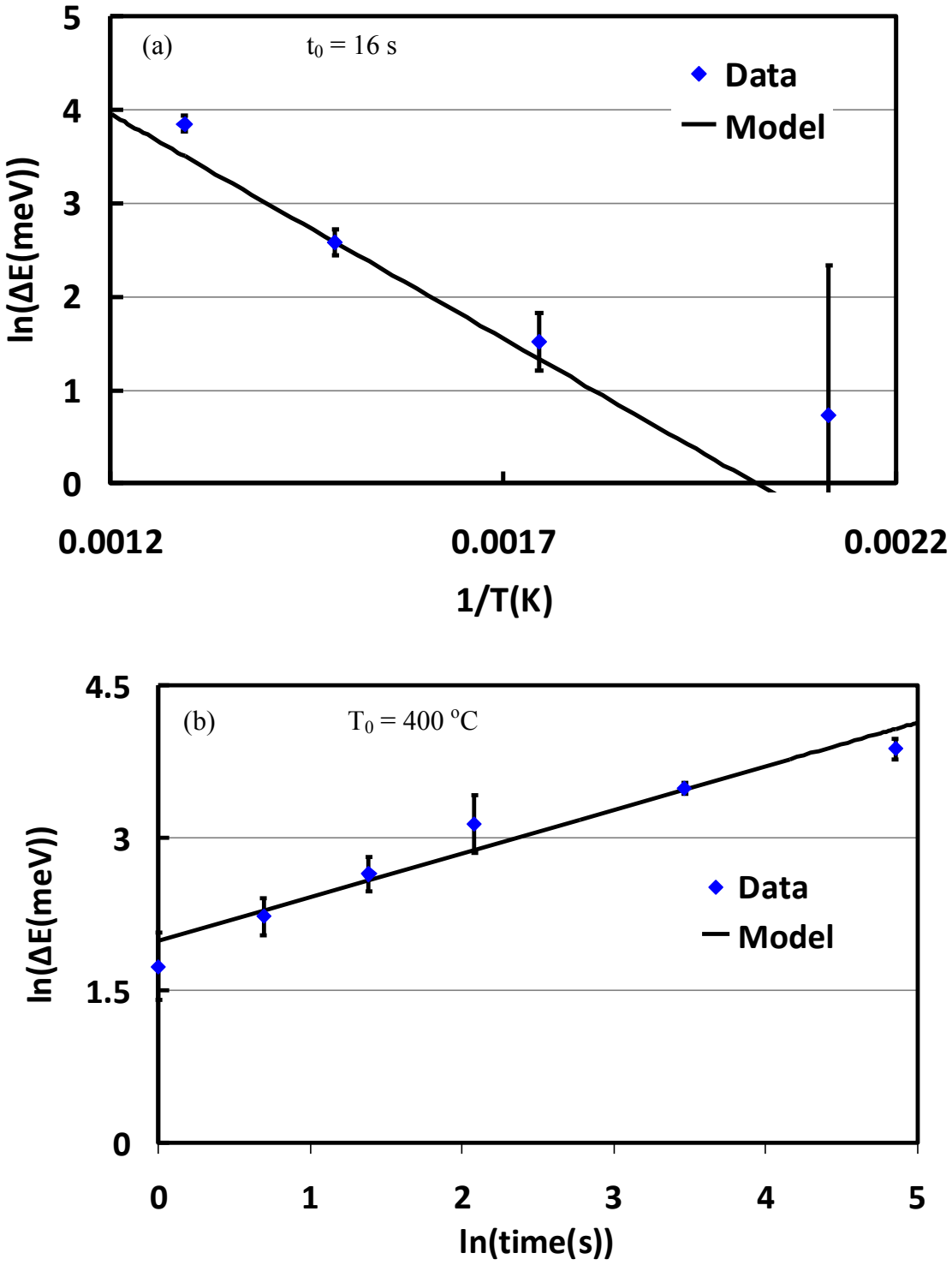

Figure 3-14. *Optical properties of 4th kind of CdSe/CdS QDs with original PL peak of 670 nm. (a) Band-gap shift ln(ΔE) – 1/T. (b) PL shift energy ln(ΔE$_{gap}$) vs heating time t at 400 °C.*

The blue-shift in PL peak was observed for increasing temperature and heating time for these

QDs, very similar to these shown in Figure 3-1, 3-2, and 3-5.

Figure 3-14 shows the bandgap dependence on temperature and heating time. The band-gap energy also shifts with heating temperature and heating time. Using the best fit analysis, we obtain: E_0 = 0.83 eV, D_0 = 9.88 X 10^{-16} m^2 s^{-1}, and n = 0.43 for the 4^{th} kind of quantum dots. The difference in the values of parameters for the 4^{th} kind of quantum dots may be attributed to different surface activation of CdSe cores.

3.5. Driving mechanism responsible for quantum dot size reduction

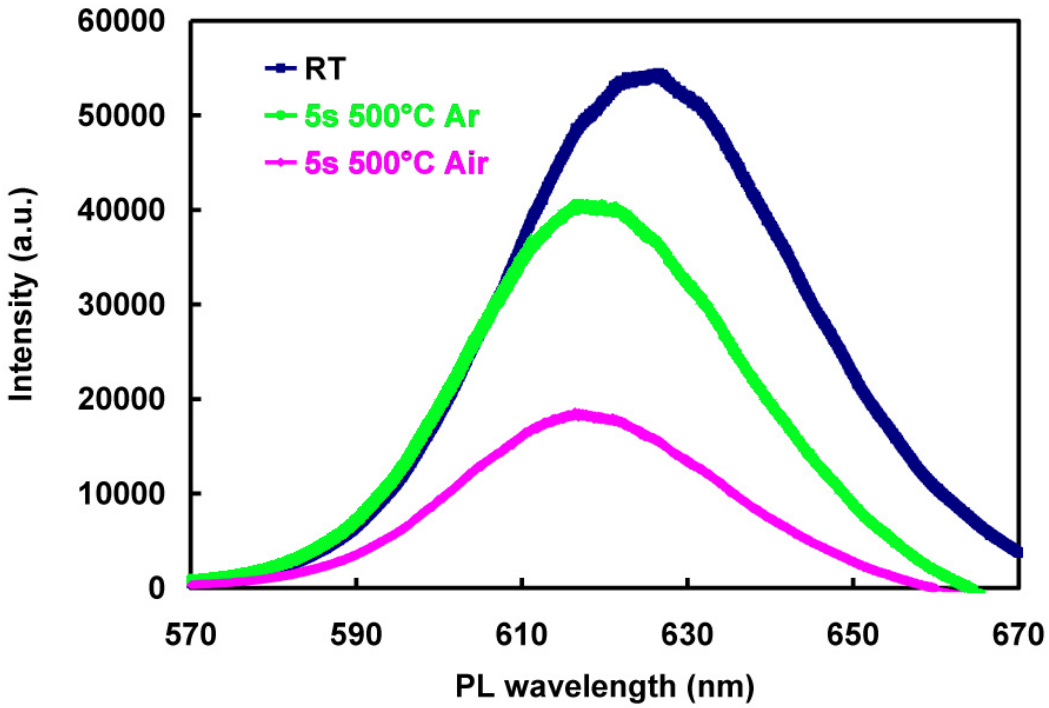

Figure 3-15. *PL spectra from CdSe/ZnS core/shell quantum dots that were unheated and heated to 500 °C for 5 s in air and in argon atmospheres.*

The PL shift that we observe when quantum dots are heated is due to the size reduction of the core structure. The shrinkage of size could be due to following two mechanisms: (i) temperature induced mass diffusion across core/shell interface, (ii) chemical reaction occurring between the core of a quantum dot and surrounding gases. To determine the relative importance of these two mechanisms, we prepared three samples. One was unheated. One was heated in air at to 500 °C for 5 seconds. The last one was heated in pure argon atmosphere at 500 °C for 5 seconds. Figure 3-15 shows PL spectra of these three samples. The PL peak of QDs shifted to higher energy after heated at 500 °C for 5 seconds, whatever in air or Ar. We observe almost same PL shift for both heated samples, which suggests that ambient air does not chemically react with these quantum dots. This experiment indicates that temperature induced mass diffusion occurring across core/shell interface is the driving mechanism behind size change. We do not discuss the intensity of PL spectra here because PL intensity is strongly dependent on QD quantity that can not be controlled well in our experiments.

4. Heating history extraction from QDs

After determining the mass diffusion energy barrier, diffusion prefactor and time exponential for each of the four kinds of quantum dots, the temperature field of a heating event can be extracted from PL spectrum. Here we demonstrate how to use one kind of QDs, two kinds of QDs to extract thermal histories.

4.1. Temperature extraction from one kind of QDs

As discussed in Section 3, PL peak changes with heating temperature. Such properties can be applied to record temperatures. Here we demonstrate how to employ one kind of QDs to study temperature distributions along a Pt hotwire. CdSe/ZnS QDs with PL peak of 576 nm are employed.

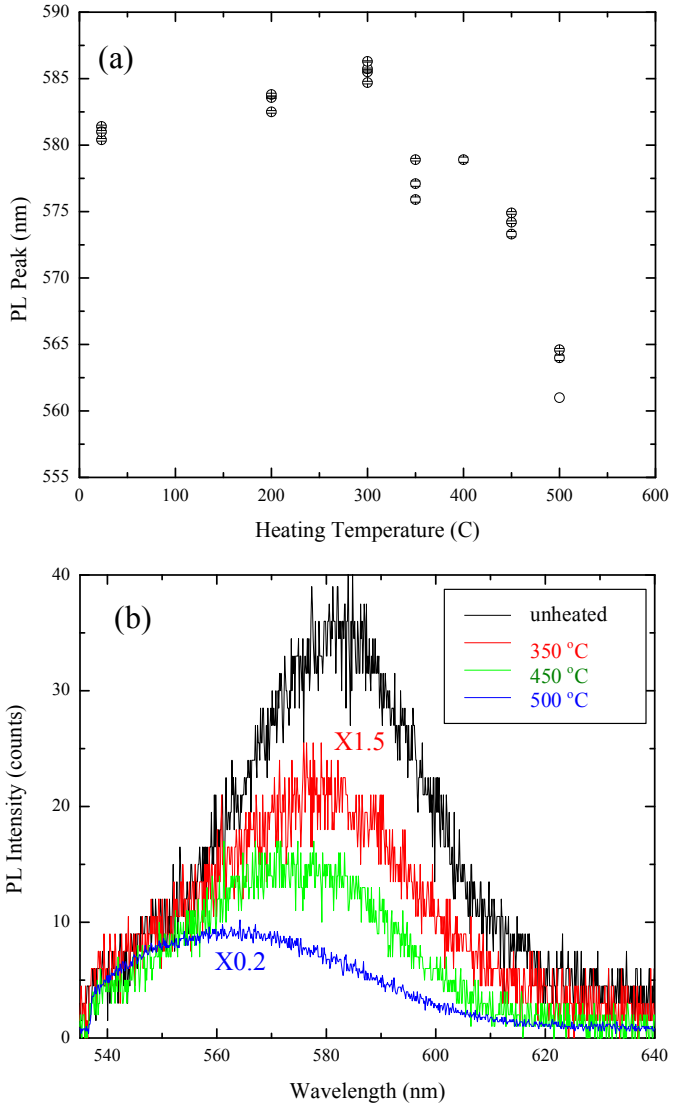

Figure 4-1. *Temperature dependent PL spectrum of QDs. (a) PL peak – T relationship and (b) PL spectrum at different temperatures.*

Figure 4-1 shows the temperature dependent PL of this kind of QDs. The temperature will be recorded by the kind of QDs and the recorded temperatures will be read out based on the relationship shown in Figure 4-1. The temperature distribution of a hotwire will be recorded by the QDs and readout from their PL peaks.

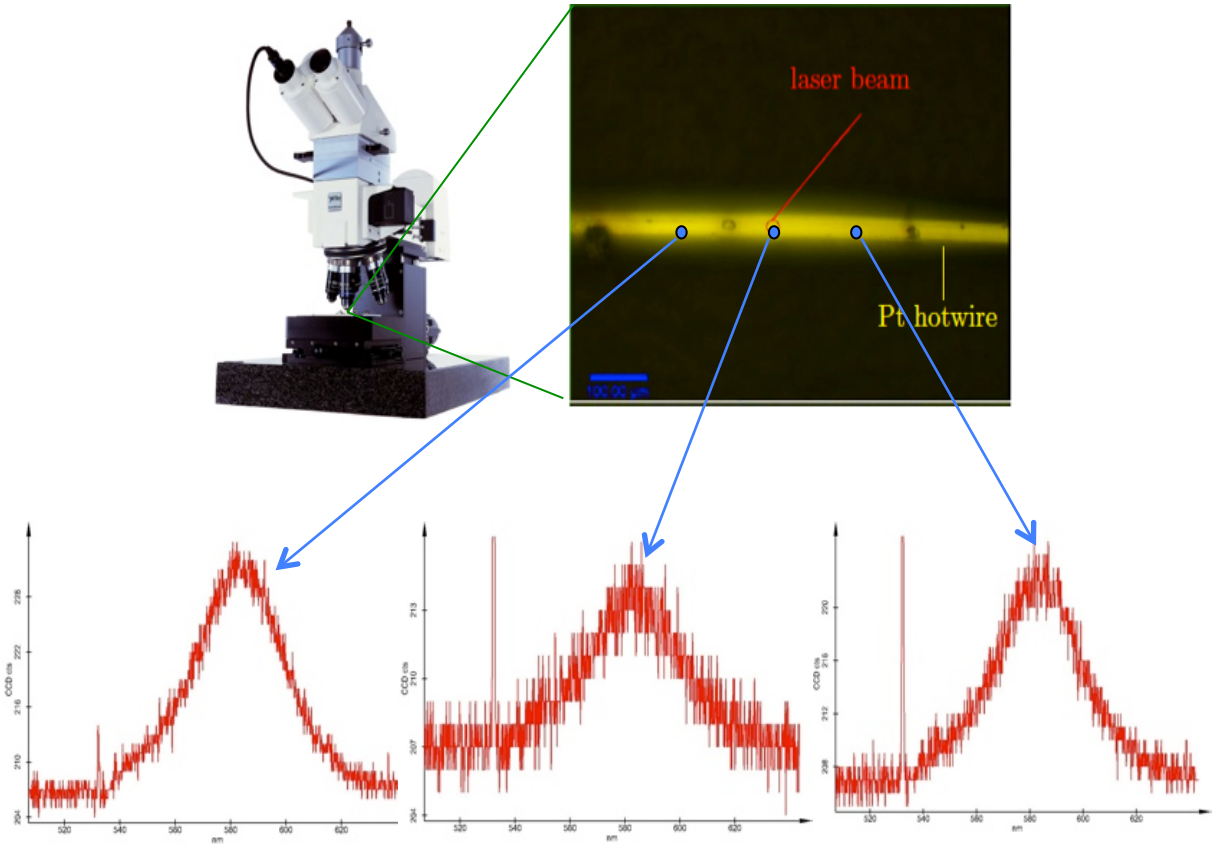

Figure 4-2. *Experimental setup to measure temperature distribution along a hotwire.*

Figure 4-2 shows the experimental setup to measure a temperature distribution along a hotwire. The QDs were deposited on a Pt hotwire and fast heated in air. Then the heated hotwire was put under a PL/Raman microscope for PL measurements. PL spectra at different locations were individually measured, shown as bottom panels in Figure 4-2. The diameter of the laser beam is about 1 micron. A series of PL spectra were measured along the hotwire.

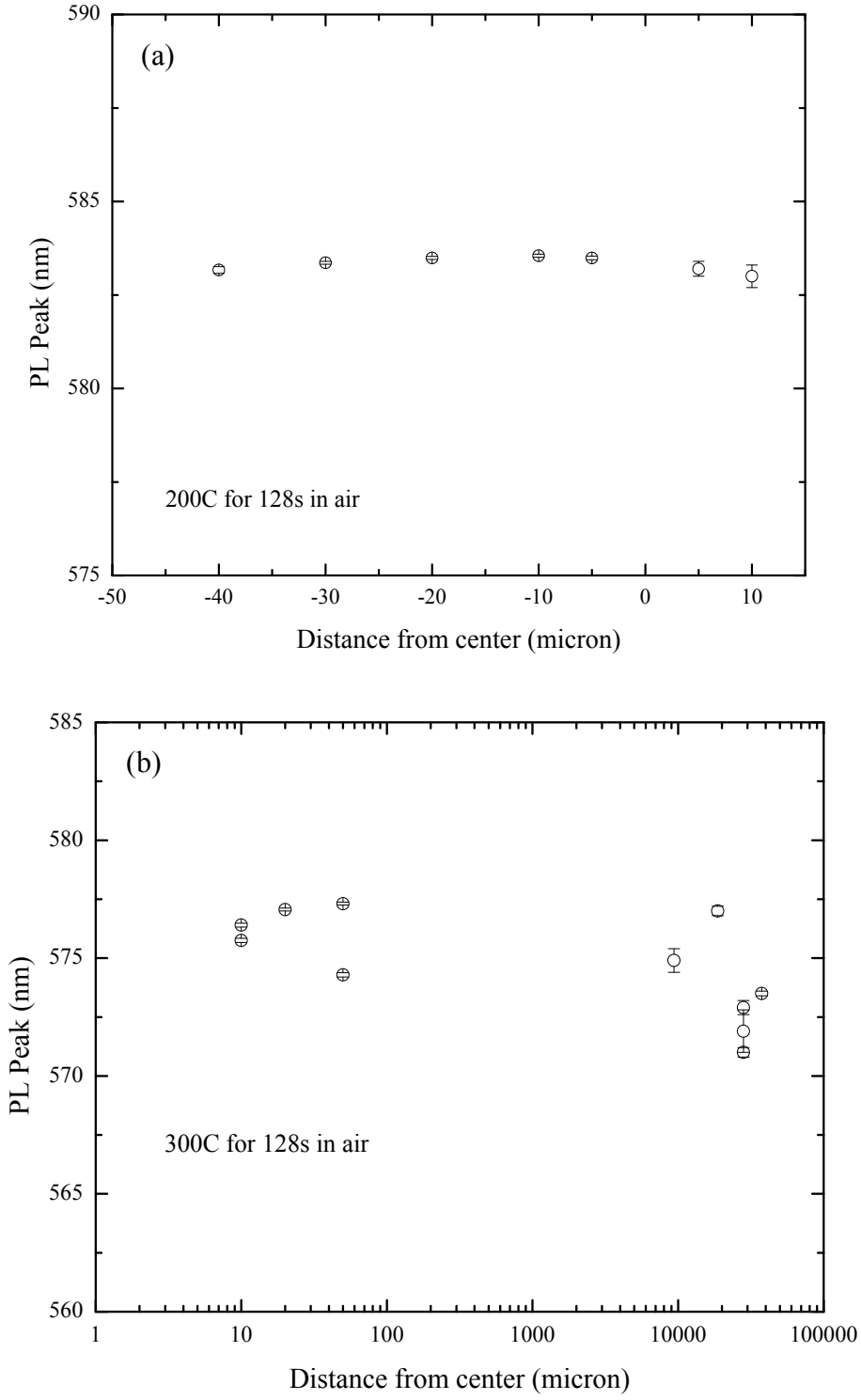

Figure 4-3. *PL peak along hotwires. (a) heating at 200 ^{o}C for 128 s in air. (b) heating at 300 ^{o}C for 128 s in air.*

Two samples were prepared and examined in air. One was fast heated at 200 ^{o}C for 128 s in air. Another was heated at 300 ^{o}C for 128 s. The measured PL peaks are almost same along Pt

hotwires (Figure 4-3), indicating the temperature of the hotwire is spatially uniform.

4.2. Heating history extraction from two kinds of QDs

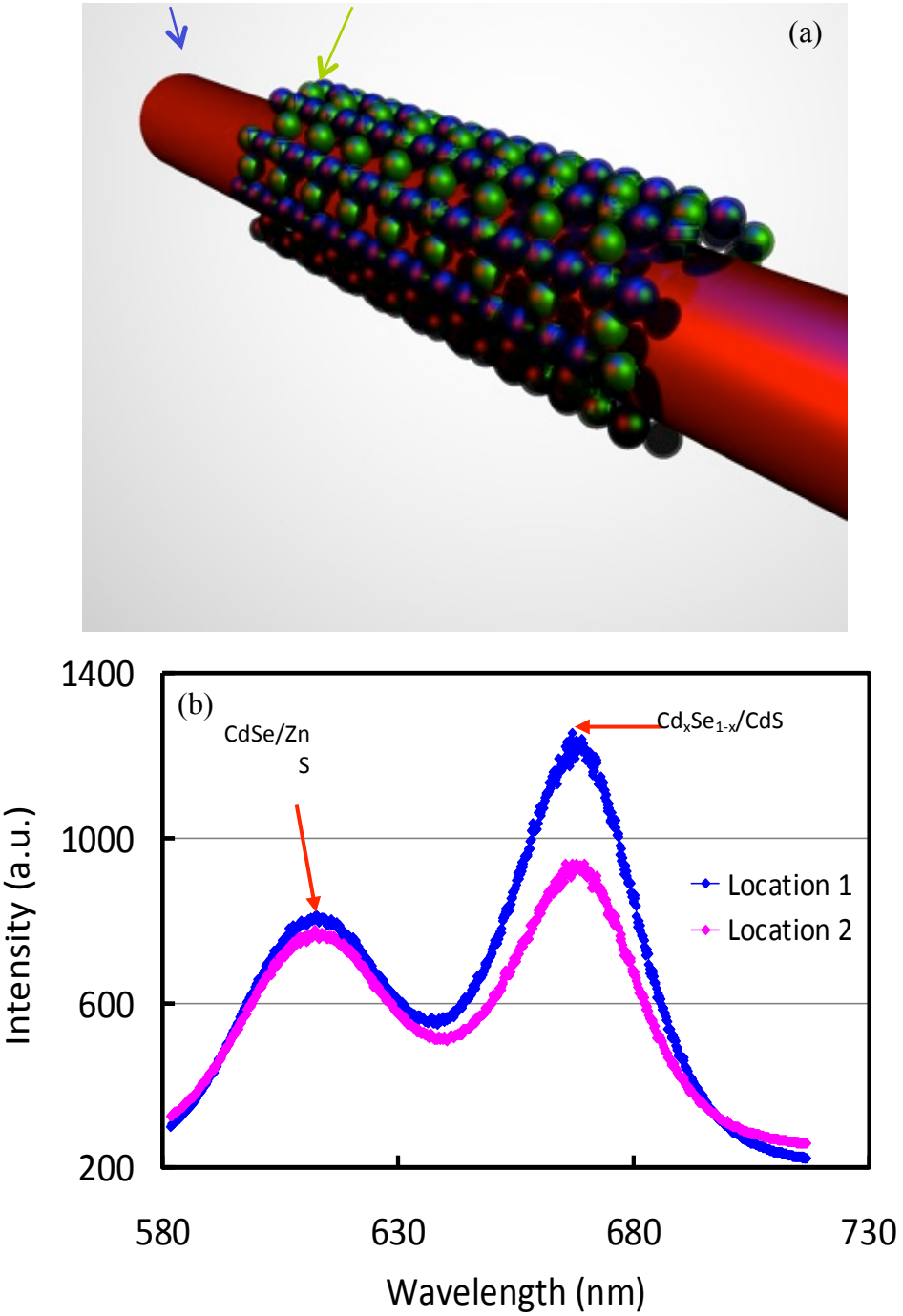

Figure 4-4. *Temperature sensors. (a) Model. (b) PL spectrum of two kinds of QDs mixed on Pt hotwire. . Two peaks are observed: one each from 1st kind of CdSe/ZnS QDs and another from 2nd kind of CdSe QDs. The intensity differs on different locations due to the non-uniform QD ratio.*

In order to extract a heating history (temperature and during), two kinds of QDs are needed. Here we mix two kind of QDs on hotwires and heat them in air (Figure 4-4a). Figure 4-4b shows the PL spectra of the mixture. We measured the PL response on at least fifteen different locations of the wire. We obtained strong PL spectrums corresponding to both quantum dots as shown in Figure 4-4b. The peak PL wavelength also matches very well with the previous data taken on individual quantum dot samples. This study shows that these two kinds of quantum dots do not interfere with each other's PL spectrum.

Figure 4-5 shows a typical case to record and extract a thermal history. Two kinds of QDs with PL peaks at 620 nm and 576 nm were mixed. Then the mixed QDs were fast heated at 400 °C for 2 seconds in air. Figure 4-5a shows the heating history. The temperature was recorded by LabVIEW VI from the electrical resistance of the Pt hotwire. The mixed QDs were heated up to 400 ^{o}C in less than 100 ms from room temperature. After heating, the QDs were cooled down to room temperature in several milliseconds. The whole heating process is a typical fast heating without any temperature delay.

Then PL spectrum of the mixed QDs was measured after heating. We measured the PL response on at least fifteen different locations of the wire. We obtained strong PL spectrums corresponding to both quantum dots as shown in Figure 4-5b. Two peaks are observed: one from the 1st kind of CdSe/ZnS QDs and another from the 2nd kind of QDs. Compared with PL of unheated QDs, both PL peaks blue-shift without interfering with each other.

The PL shift can be expressed as**:**

$$\begin{cases} |\Delta E_{g,1}(T,t)| = \left[2\pi^2\left(\frac{a_B^2}{a_1^3}\right) - 1.786\left(\frac{a_B}{a_1^2}\right)\right] R_y^* \sqrt{D_{0,1}} \exp\left(-\frac{E_{0,1}}{2k_B T}\right) t^{n1} \\ |\Delta E_{g,2}(T,t)| = \left[2\pi^2\left(\frac{a_B^2}{a_2^3}\right) - 1.786\left(\frac{a_B}{a_2^2}\right)\right] R_y^* \sqrt{D_{0,2}} \exp\left(-\frac{E_{0,2}}{2k_B T}\right) t^{n2} \end{cases} \quad (4\text{-}1)$$

In Equation 4-1, the parameters $E_{0,1}$, $D_{0,1}$, $n1$, $E_{0,2}$, $D_{0,2}$, $n2$ were fitted from Section 3. $\Delta E_{g,1}$ and $\Delta E_{g,2}$ were measured from Figure 4-5b. Then the thermal history (heating temperature T and heating time t) can be extracted from Equation 4-1.

Using Equation 4-1, the heating temperature is solved as $T \sim 400$ ^{o}C and heating time of $t = 2$ s.

The reconstructed heating temperature T and heating time t were in agreement with the thermal event recorded from the electrical resistance of the Pt hotwire, as shown in Fig. 4-5a.

This experiment demonstrates that two kinds of quantum dots could be mixed together to record thermal histories. The recorded thermal histories (heating temperature and heating duration) can be extracted from PL spectra.

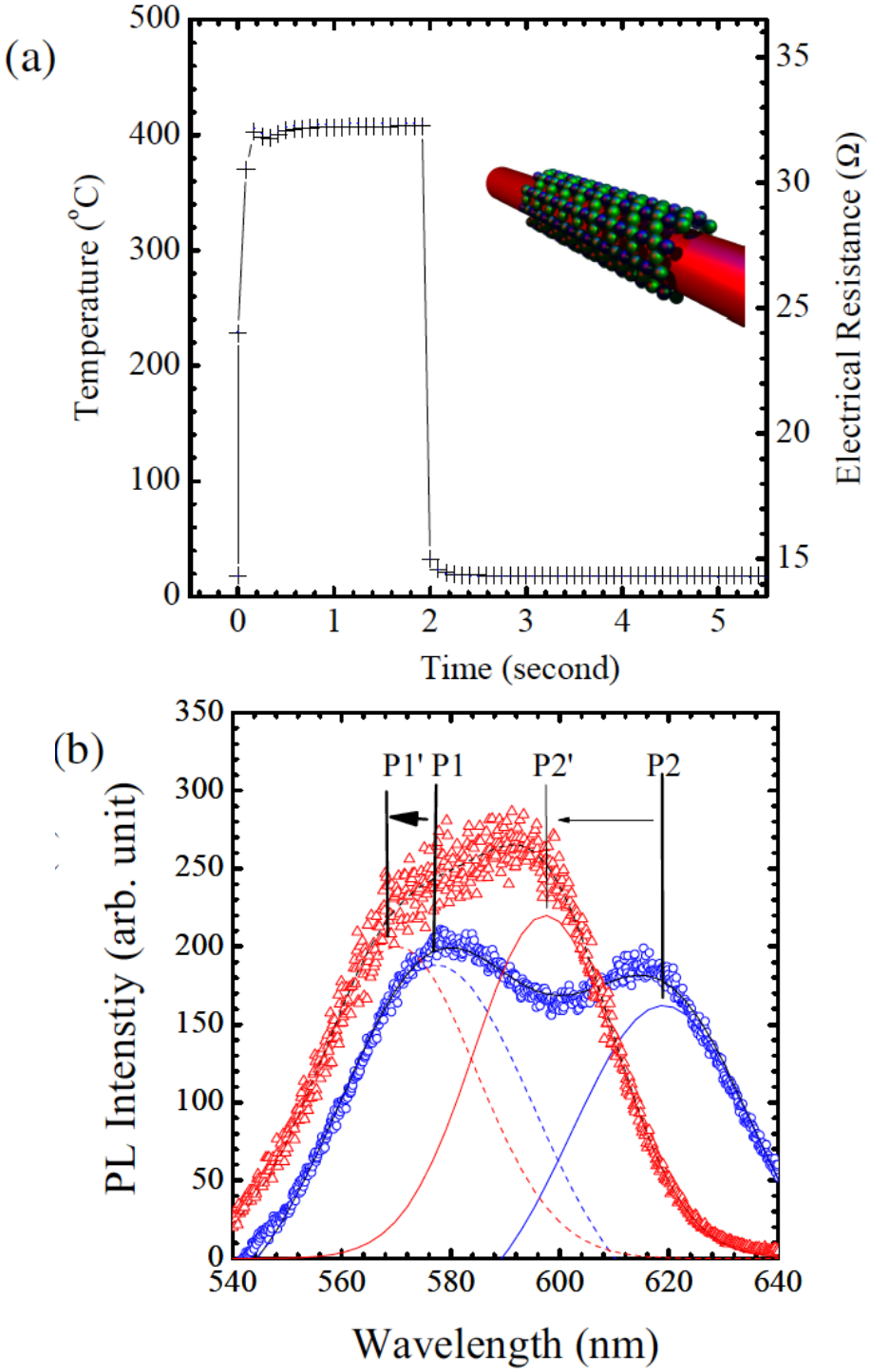

Figure 4-5. *Thermal history of a heating event without time delay. (a) A heating event without time delay. Inset: 3D model of two kinds of QDs deposited a Pt hotwire. The temperature of the heating event was calculated from electric resistance of the Pt hotwire that was recorded by a LabVIEW VI. (b) PL spectra of mixed QDs. Blue circles: measured PL data of unheated QDs. Blue curves: fitted PL peaks of unheated QDs. Red triangles: measured PL date of heated QDs. Red curves: fitted PL peaks of heated QDs. Solid curves: fitted PL peak of 1st kind of QDs. Dashed curves: fitted PL peak of 2rd kind of QDs.*

4.3. Heating history extraction from three kinds of QDs

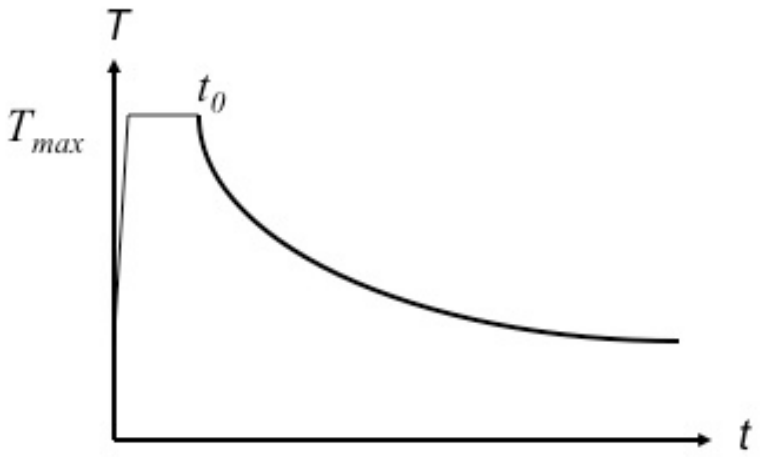

Figure 4-5. Heating history with time delay.

In real explosions, the temperature decreases very slow, as shown in Figure 4-5. Such heating process is more complex than that of fast heating. The complex heating can be seperated as two heating processes: a fast heating and a heating delay expressed as:

$$\begin{cases} T(t) = T_{\max}(t) \quad (t \le t_0) \\ T(t) = T_{\max} \exp(-\beta t) \quad (t > t_0) \end{cases} \tag{4-2}$$

In Equation 4-2, three unknown parameters, T_{max}, t_0, and β can be extracted. T_{max} and T_0 can be extracted from Equation 4-1. In order to solve the third unknown parameter β, we need a third equation. In Section 3, at least three kinds of QDs were calibrated and three equations were set-up. So a thermal history of a real explosion can be extracted using three kinds of QDs. The work to extract a heating history with time delay is being carried out.

5. TEM STUDIES

5.1. *Ex-situ* HRTEM observation of quantum dots with peak wavelength of 620 nm

The CdSe/ZnS QDs with PL peak of 620 nm are *ex-situ* examined on TEM. The QDs are heated on a TEM heating holder in vacuum or on a Pt hot-wire in air.

5.1.1. *Ex-situ* HRTEM observation of CdSe/ZnS heated on TEM heating holder

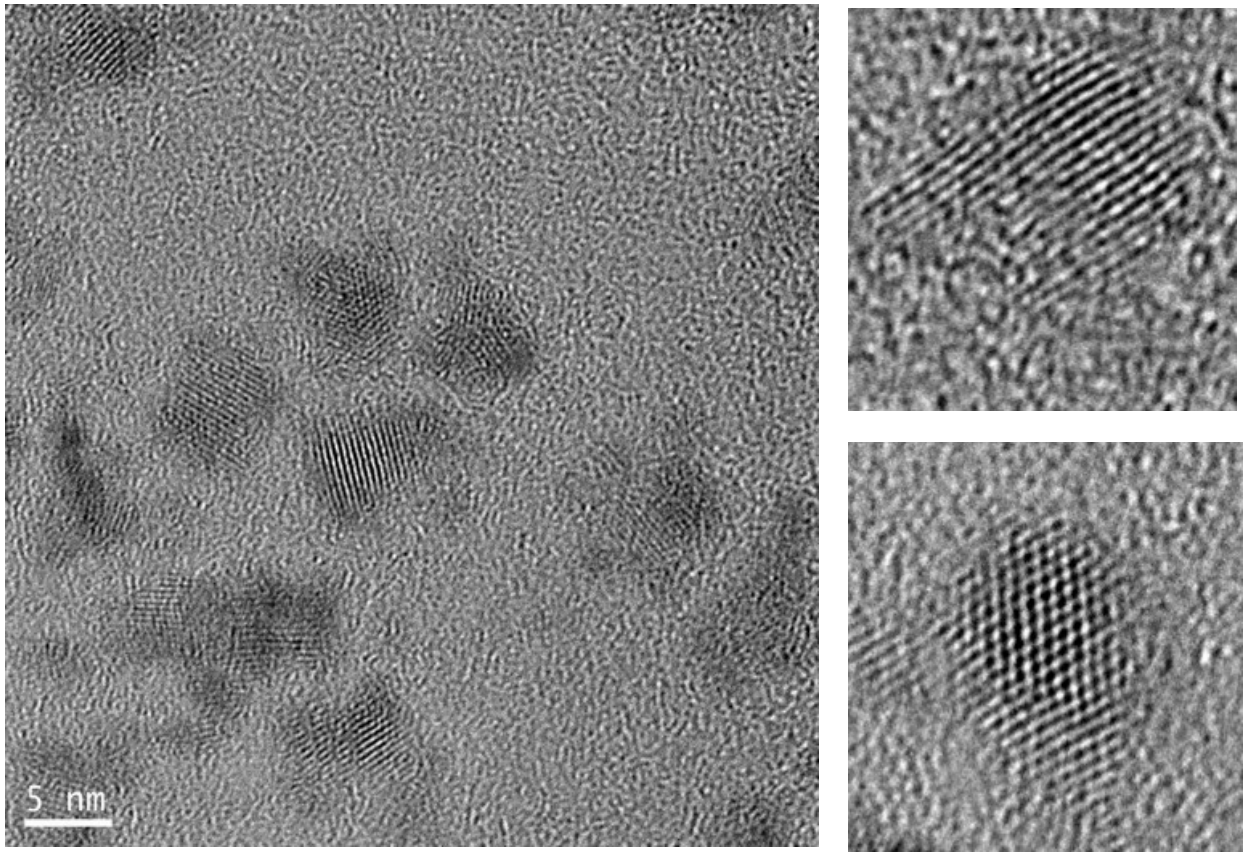

Figure 5-1. *HRTEM images of CdSe/ZnS QDs with PL peak of 620 nm. Left: Several QDs deposited on TEM grid. Right: Individual QDs at higher magnification.*

The as-received CdSe/ZnS QDs are crystalline. Figure 5.1 shows HRTEM images of the QDs. The HRTEM images show clear lattice fringes, indicating the crystalline core of the QDs. A thin ZnS layer is coated on the crystalline CdSe core. HRTEM images indicated that the lattice around the QD core is tortured, different from that of the crystalline core, indicating the ZnS shell.

In order to analyze the diameter distribution of the CdSe/ZnS QDs at different temperatures, we *ex-situ* observe the QDs at different temperatures from room temperature to 500 °C.

Hundreds of HRTEM images of the as-received QDs were took at room temperature. Then the area of each QD was measured and its diameter was calculated.

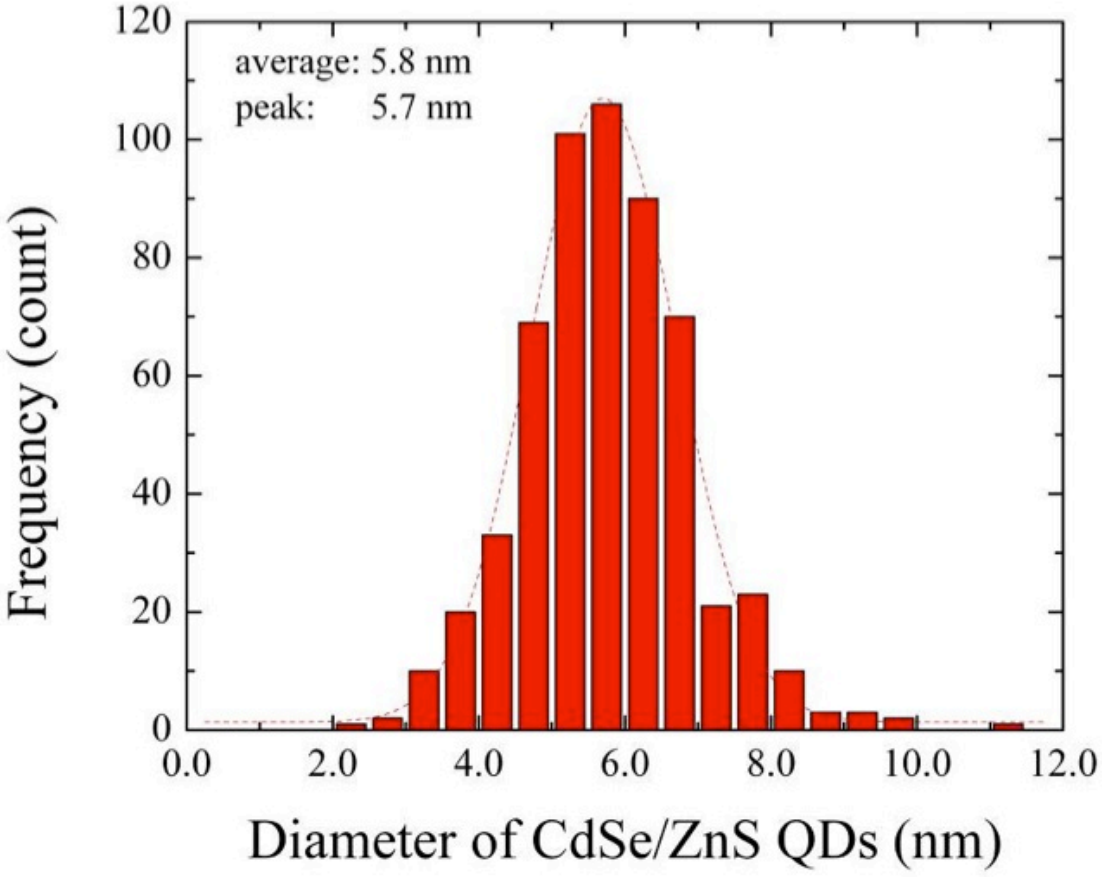

Figure 5-2. *Diameter histogram of as-received CdSe/ZnS QDs.*

Figure 5-2 shows the histogram of the as-received CdSe/ZnS QDs. Totally about 1000 QDs were analyzed and their diameters were calculated from the HRTEM images. The diameter of the CdSe/ZnS QDs distributes as a Gauss function with an average diameter of 5.8 nm and a peak of 5.7 nm.

Then the QDs were heated in TEM and *ex-situ* observed on TEM. The QDs were heated up to a certain temperature, such as 300 °C, in about one minute, kept at the heating temperature for 1 to 5 minutes, then cooled down to room temperature in less one minute. The heated QDs were *ex-situ* observed at room temperature and HRTEM images taken at room temperature. The size of the heated QDs is analyzed from these HRTEM images.

Statistical analysis indicates that the size of the heated QDs is almost same with that of as-received QDs when the heating temperature is not high than 500 °C.

5.1.2. *Ex-situ* HRTEM observation of CdSe/ZnS QDs heated on Pt hot-wires

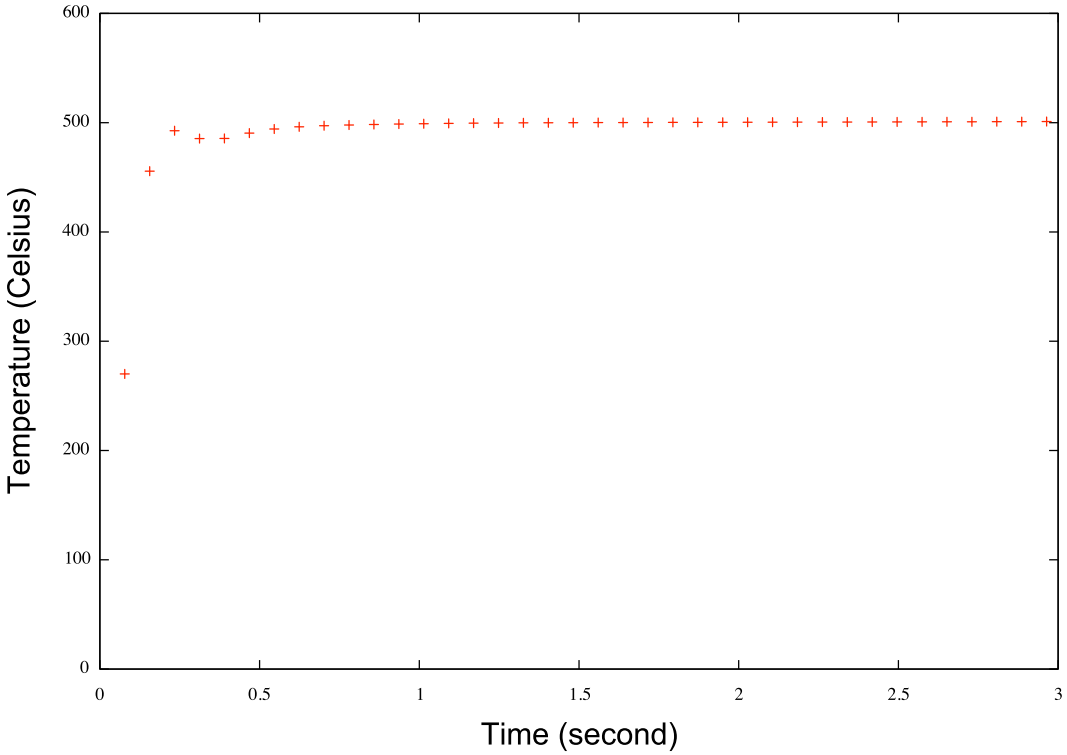

Figure 5-3. *Temperature-time curve of a Pt hot-wire when a 228 mA DC current passing through in air.*

The CdSe/ZnS QDs were also heated on Pt hot-wires in air in MIT. Figure 5.3 shows a typical heating rate of a Pt hot-wire. When a DC current of 228 mA passed through a Pt hot-wire, the Joule heating caused the temperature of the Pt hot-wire increases to 500 °C in air in less than 200 milliseconds. The CdSe/ZnS QDs deposited on the Pt hot-wire was heated up very fast in less than one second. Then the QDs were heated in air for several seconds, cooled down to room temperature.

After the PL spectra of the heated CdSe/ZnS QDs were measured, the microstructure of the heated QDs were examined on TEM.

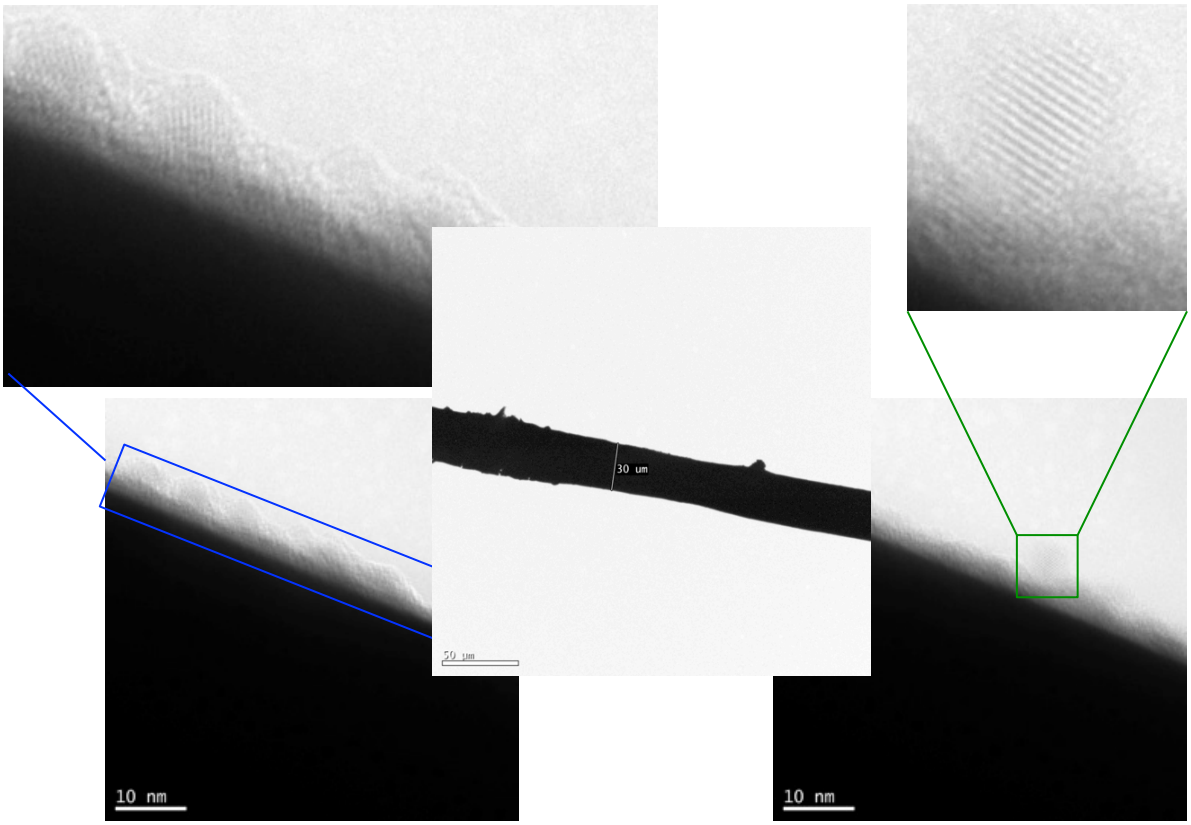

Figure 5-4. *TEM images of CdSe/ZnS QDs heated on a Pt hot-wire in air. Heated temperature: 500 ^{o}C; Heating time: 2 s. Center image: TEM image of the Pt hot-wire at low-magnification.*

Figure 5-4 shows TEM images of such heated CdSe/ZnS QDs in air. The QDs were heated at 500 ^{o}C for 2 seconds. A dense layer of CdSe/ZnS QDs were deposited on the Pt hot-wire surface. After being heated, the QDs were also crystalline.

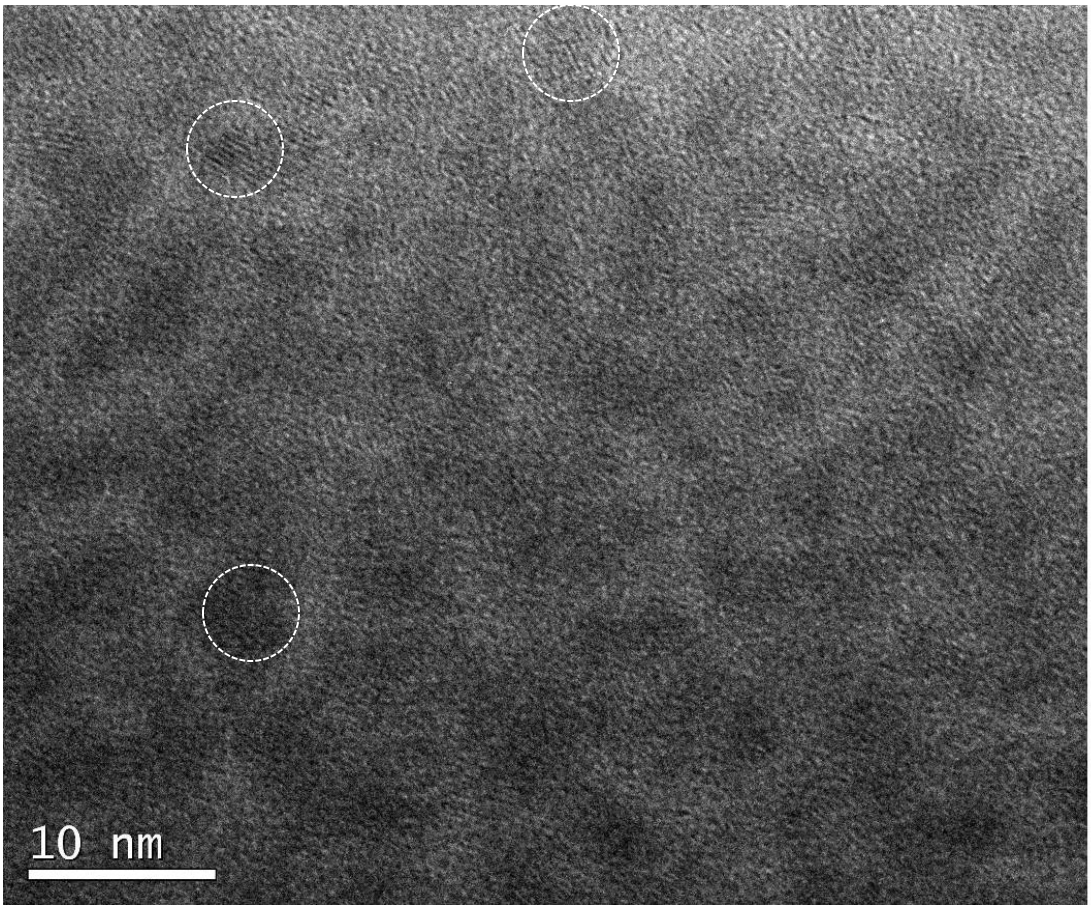

Figure 5-5. *HRTEM image of QDs after being heated on Pt hotwires. Some QDs are outlined by white circles.*

In order to obtained quantitative size change of the QDs, thousands of QDs were statistically analyzed from HRTEM images. Figure 5-5 shows HRTEM image of heated QDs on Pt hotwire. The areas of these QDs were measured and the diameters of the QDs were calculated.

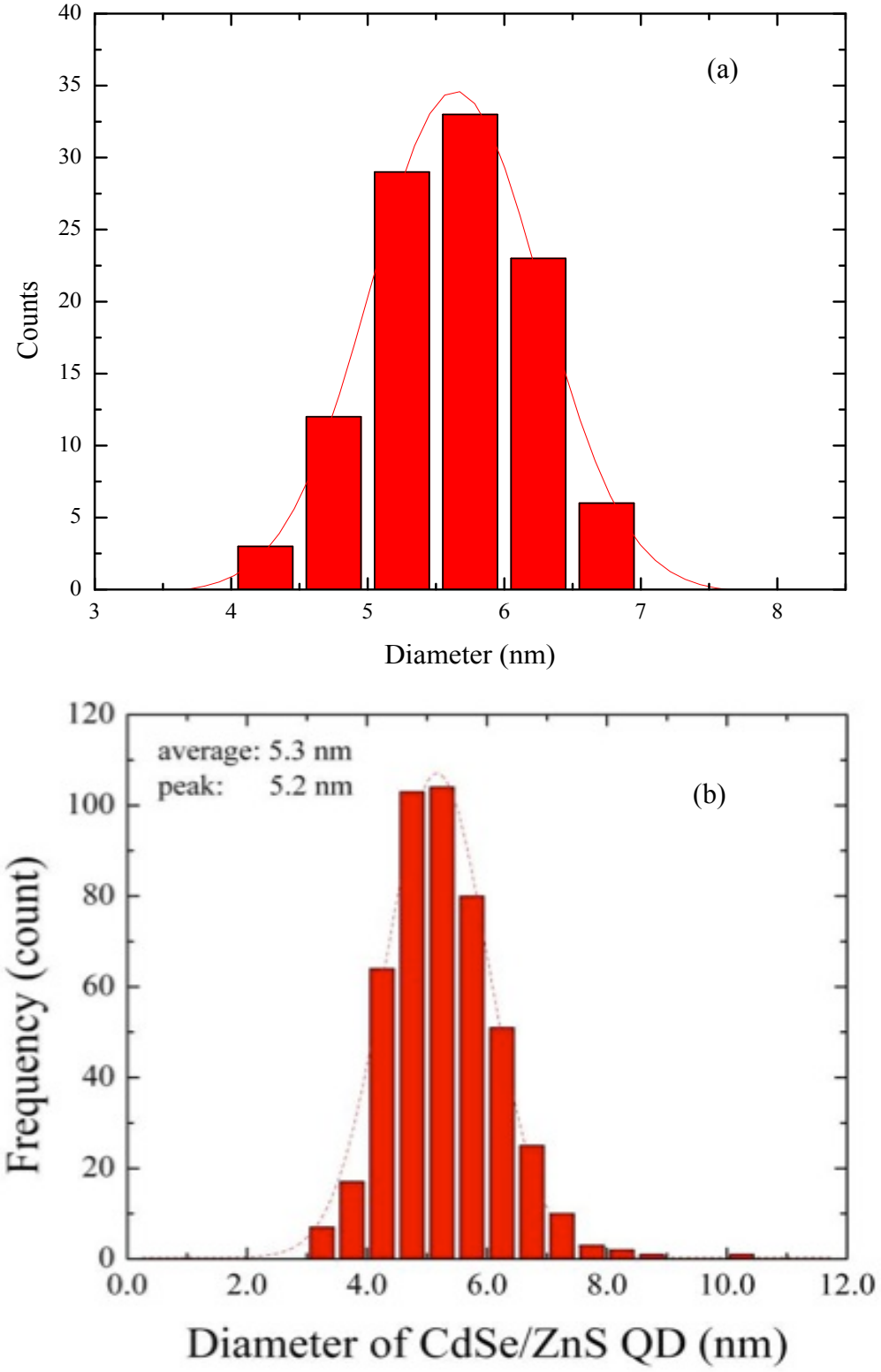

Figure 5-6. *Diameter histogram of heated CdSe/ZnS QDs on Pt hot-wires. The QDs were heated at 500 °C in air for (a) 2 s and (b) 5 s. The diameter histogram of unheated QDs was plotted in Figure 5-4.*

Figure 5-6 shows the histogram of QD diameter statistically analyzed from HRTEM shown in Figure 5-5. Over 500 QDs were statistically analyzed for each case. The QDs were heated in air at 500 °C for 2 s and 5 s. Hundreds of QDs were analyzed from HRTEM images for each histogram. Figure 5-6a shows the diameter distribution of the heated QDs after being heated at 500 °C for 2 s. Figure 5-6b shows the diameter distribution of QDs being heated at 500 °C for 5 s. The diameter of QDs still distributes as a Gauss function in both cases.

Compared with unheated QDs (shown in Figure 5-4), it seems that the QDs shrink after heating. However we can not make any conclusion at present stage because of experimental errors of the statistical analysis. More detailed work is needed to conclude if the QDs shrink or not.

The diameter change would affect the discrete energy levels of CdSe QDs, causing the PL blue shift of CdSe QDs. For example, previous researches show that the PL peak of pure CdSe QDs with diameter of 5.5 nm is 620 nm, 570 nm with diameter of 3.5 nm, and 555 nm with size of 2.5 nm. Here we have not observed any obvious size shrinkage to explain the PL shift with temperature in our research. The PL blue-shift should mainly come from other source, such as the mass diffusion of ZnS layer.

5-2. *Ex situ* HRTEM observation of QDs with peak wavelength of 576 nm

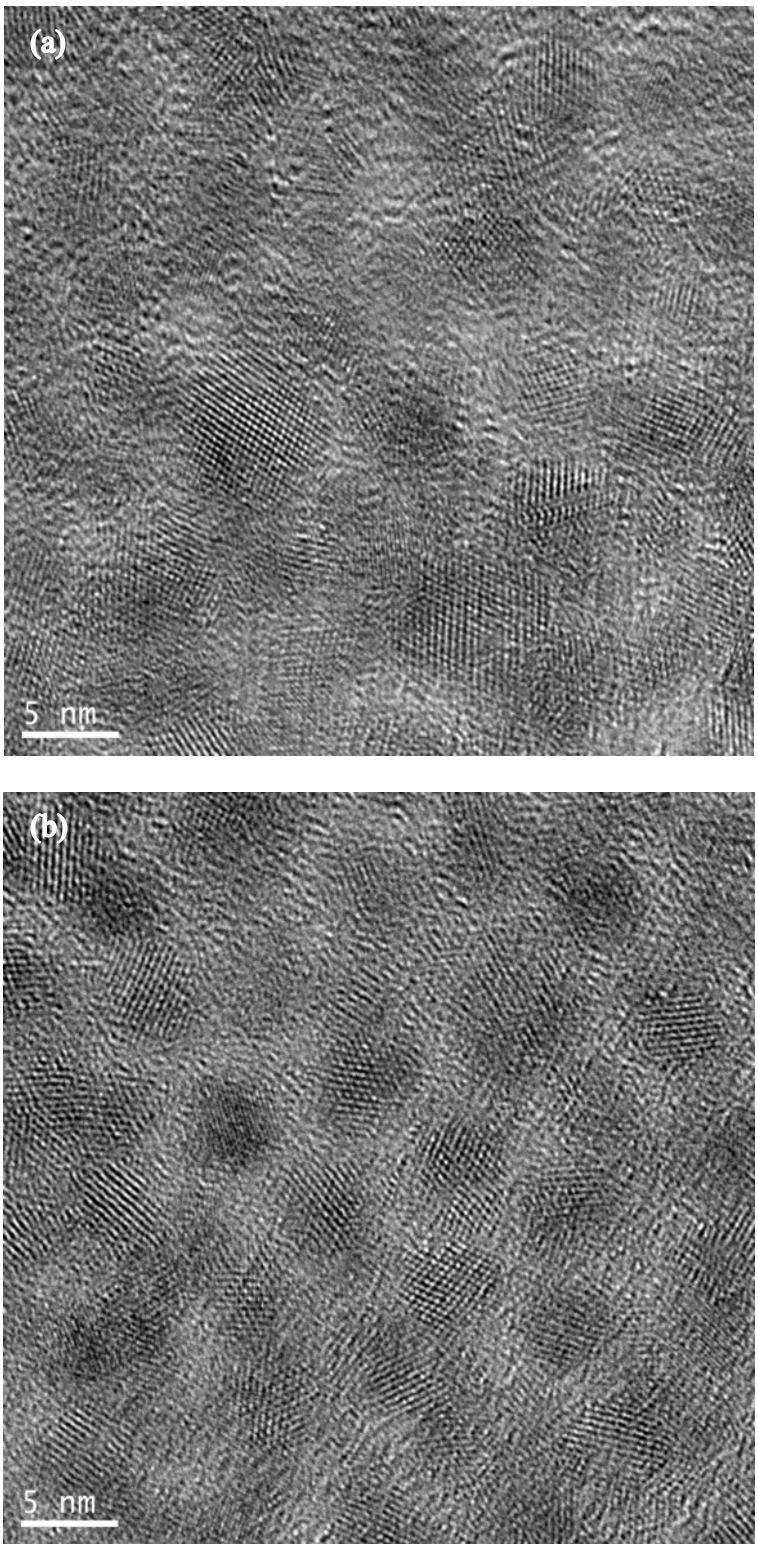

Figure 5-7. *HRTEM images of QDs with PL of 576 nm. (a) unheated and (b) heated at 400 ^{o}C for 60 s.*

Besides the 1st kind of CdSe/ZnS QDs with PL peak of 620 nm, the 2nd kind of QDs with PL peak wavelength of 576 nm were also examined on TEM at different temperatures.

Figure 5-7a shows HRTEM images of the 2nd kind of QDs with PL peak of 576 nm. The unheated QDs were nanocrystals with diameter of 5.5 nm.

The 2nd kind of QDs were heated at 100 – 500 °C on TEM and HRTEM images were *ex situ* taken at room temperature. Figure 5-7b is a typical HRTEM image of the heated QDs at 400 °C for 60 s. Detailed statistical analysis indicated that the size of the QDs does not change significantly after heating.

5.3. *In-situ* HRTEM observation of heated CdSe/ZnS QDs

Besides the *ex-situ* observation of the heated QDs, the QDs were also *in situ* examined on TEM. Such *in-situ* HRTME observation focused on an individual QD to disclose the heating effect on QD microstructure.

5.3.1. *In-situ* HRTEM observation of CdSe/ZnS QDs heated on TEM heating holder

In order to study the diameter of the QDs before and after heating, we carried out *in-situ* HRTEM observation of CdSe/ZnS QDs on TEM. The CdSe/ZnS QDs are deposited on a TEM grid, loaded into the heating chamber of the TEM heating holder. Then the CdSe/ZnS QDs were heated in TEM column and *in-situ* observed on TEM.

Figure 5.8 shows *in-situ* HRTEM images at a series of heating temperatures. The QDs were heated up to a certain heating temperature in less then one minute, kept at the heating temperature for several minutes, cooled down to room temperature in less than one minute, and observed at room temperature. Then the QD were heated up to next heating temperature and *in-situ* observed. During the whole procedure, the QDs were always traced. From the *in-situ* HRTEM images shown in Figure 5-8, no obvious change of the QD size was observed up to 270 °C in vacuum within experimental errors.

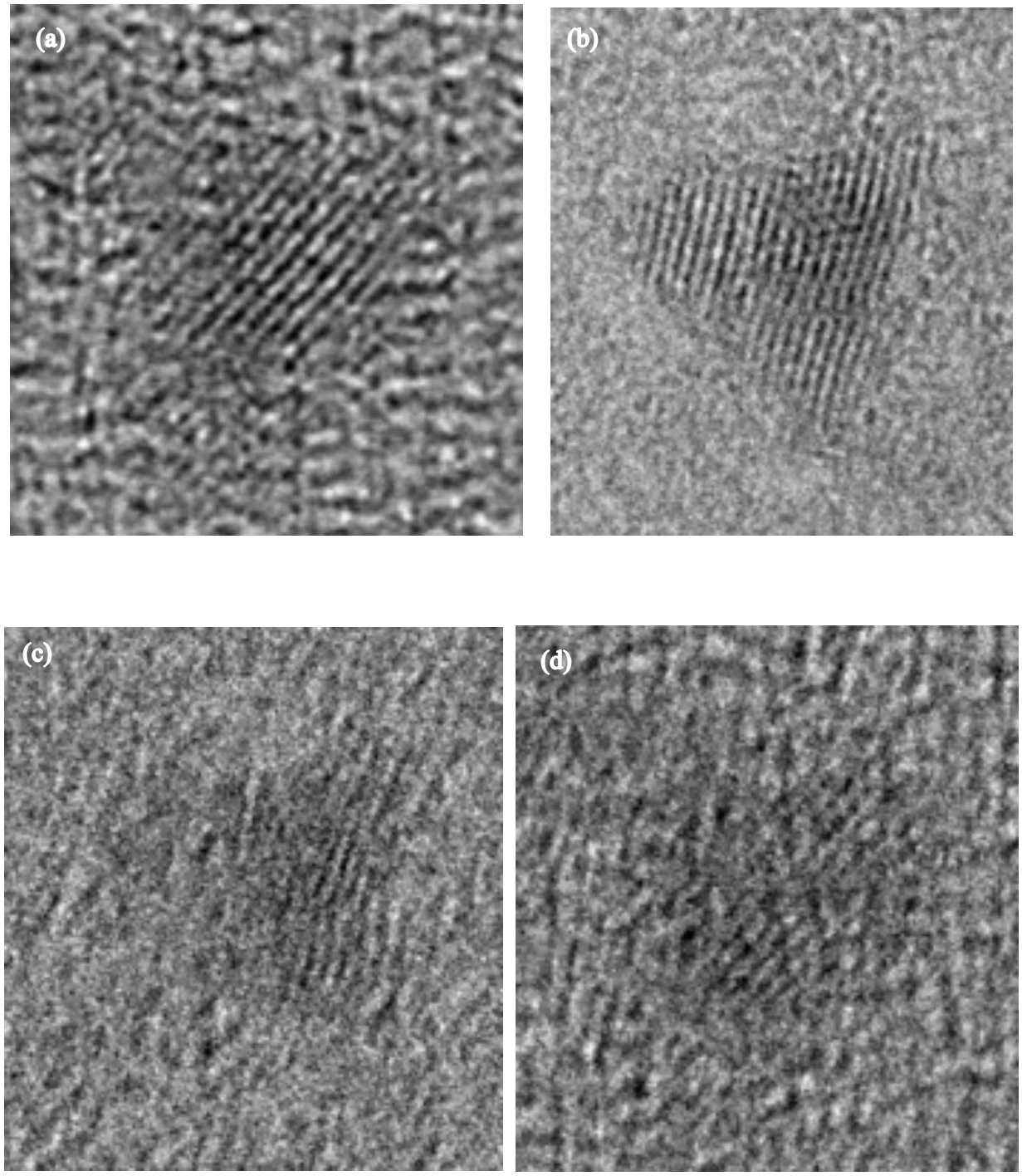

Figure 5-8. *A series of in-situ HRTEM images of CdSe/ZnS QDs heated at (a) room temperature, (b) 100 °C, (c) 250 °C, and (d) 270 °C for 5 min.*

5.3.2 *In-situ* HRTEM observation of CdSe/ZnS QDs fast-heated on Pt hot-wire

In order to speed up the heating rate and cooling rate, the CdSe/ZnS QDs were also heated on Pt hot-wires in TEM column. Use the Pt hotwire in a STM holder, QDs were fast heated in vacuum.

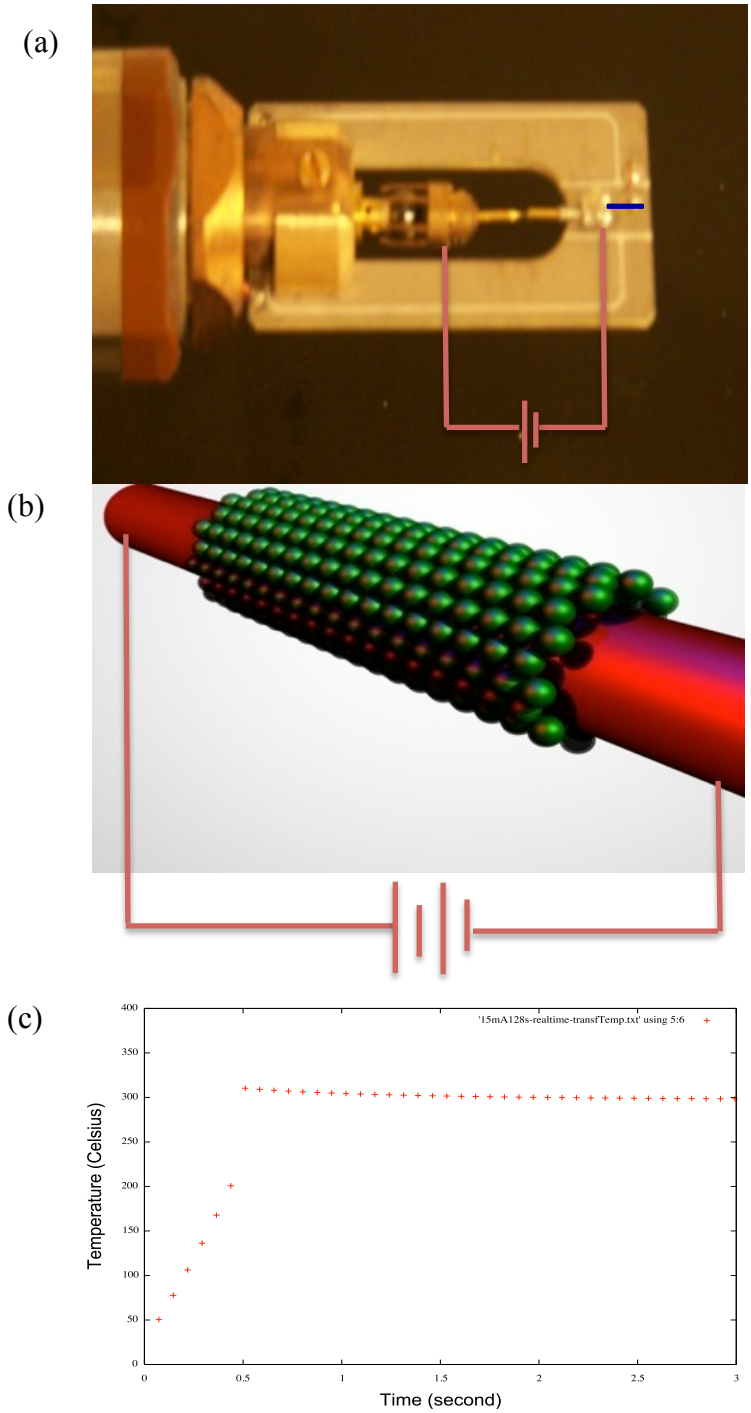

Figure 5-9. *Fast-heating of QDs on Pt hot-wire. (a) Tip of a STM holder used for fast-heating experiments. (b) Setup of fast-heating. (c) Temperature – time curve of a Pt hotwire in vacuum when a current passes through.*

During the fast-heating procedure, CdSe/ZnS QDs were deposited on a Pt hotwire with a diameter of 25 microns. Then the Pt hot-wire was connected to a power supply using a STM holder (Figure 5.9a-b). The STM holder was loaded into TEM column for *in-situ* heating and TEM observation. The Pt hot-wire was heated up to several hundred Celsius from room temperature in several hundred millisecond (Figure 5.9c), much faster than that of the TEM heating holder, making the fast-heating of QDs possible. Then the QDs were heated on the Pt hot-wire for several seconds, cooled down to room temperature, and *in-situ* observed at room temperature. The QDs were traced during the whole fast-heating procedure.

Using the same setup, the QDs were also fast-heated in air. The heating rump time and cooling rump time was less than 73 milliseconds. Then QDs were directly observed on TEM.

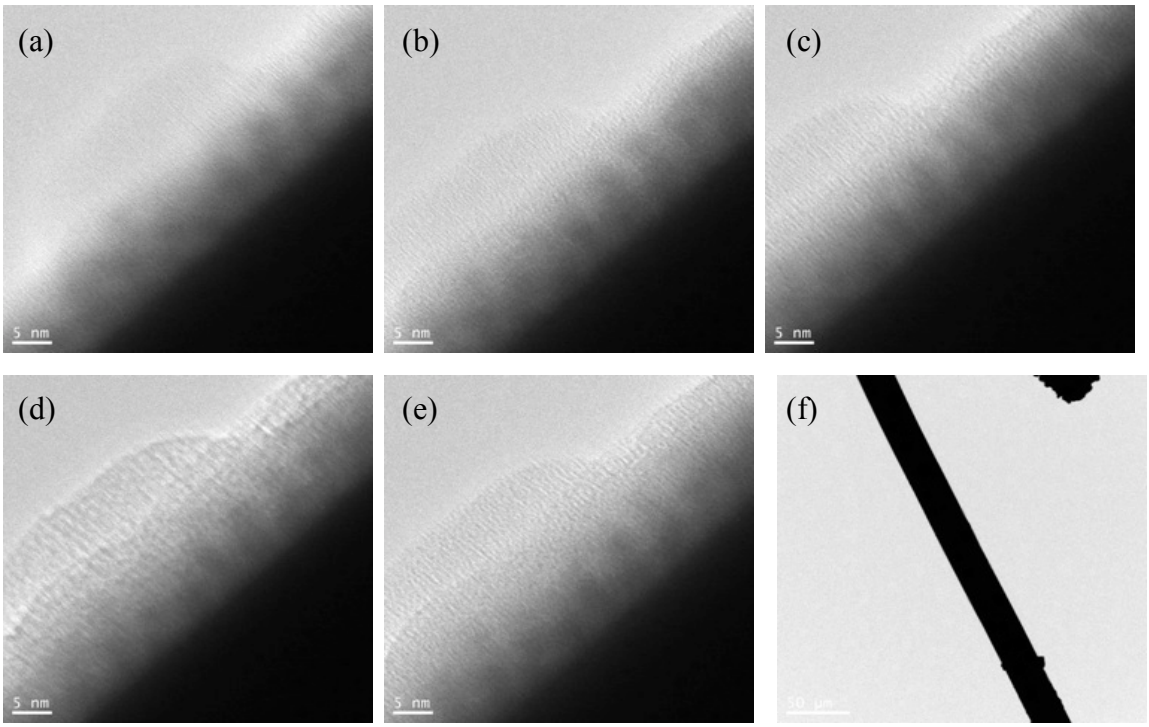

Figure 5-10. *In-situ TEM images of CdSe/ZnS QDs fast heated on TEM using STM holder. The applied voltage on the Pt hot-wire is marked for each image.*

Figure 5-10 shows a variety of *in-situ* TEM images of CdSe/ZnS QDs fast heated at different temperatures on TEM. The darker areas on the Pt hot-wire surface are CdSe/ZnS QDs. Different DC voltages were applied on the Pt hotwire to heat the QDs. From the electric resistance of the Pt hotwire, the temperature of the Pt hotwire were calculated. From TEM images shown in Figure 5-10, no obvious size change was observed.

5.3.3. *In-situ* HRTEM observation of CdSe/ZnS QDs fast heated by carbon nanotubes

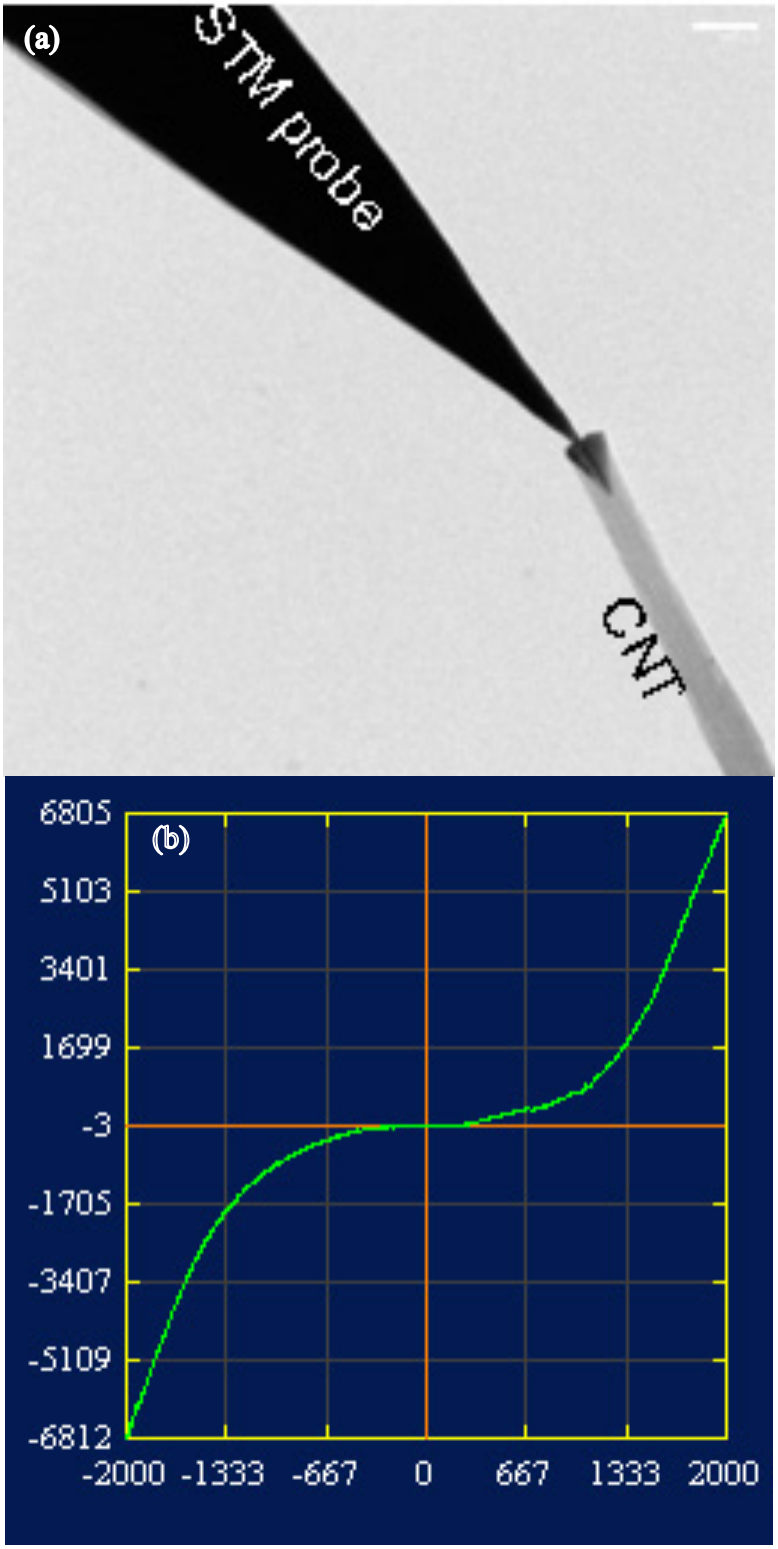

Figure 5-11. *Super-fast heating of QDs. (a) TEM image of CNT-heating set-up. (b) I-V curve of a CNT.*

In order to increase the heating rate and cooling rate further, CdSe/ZnS QDs were super-fast heated using carbon nanotubes (CNT) as hot-wires. Figure 5-11a shows the set-up. A CNT was employed as a hot-wire and a temperature sensor connected to a STM tip. CdSe/ZnS QDs were deposited on the CNT. After applied a voltage on the CNT, a current passed through the CNT (Figure 5-11b) and heated the QDs because of Joule heating.

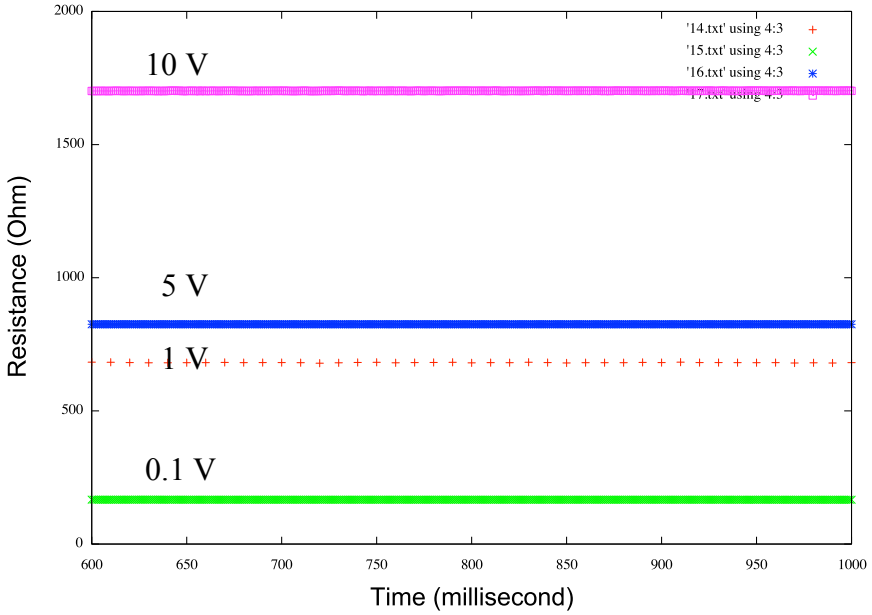

Figure 5-12. *Electrical resistance of a MWCNT heated at different voltage. From bottom to top, the applied voltage is 0.1 V, 1 V, 5 V, and 10V.*

Figure 5-12 shows the electrical resistance of a multi-walled CNT (MWCNT) under different applied voltages. The MWCNT was connected to the power supply of the STM holder. The electrical resistance increased with voltage. So CNTs can be used as hot-wires and temperature sensors, as Pt hot-wires do, to super-fast heat QDs.

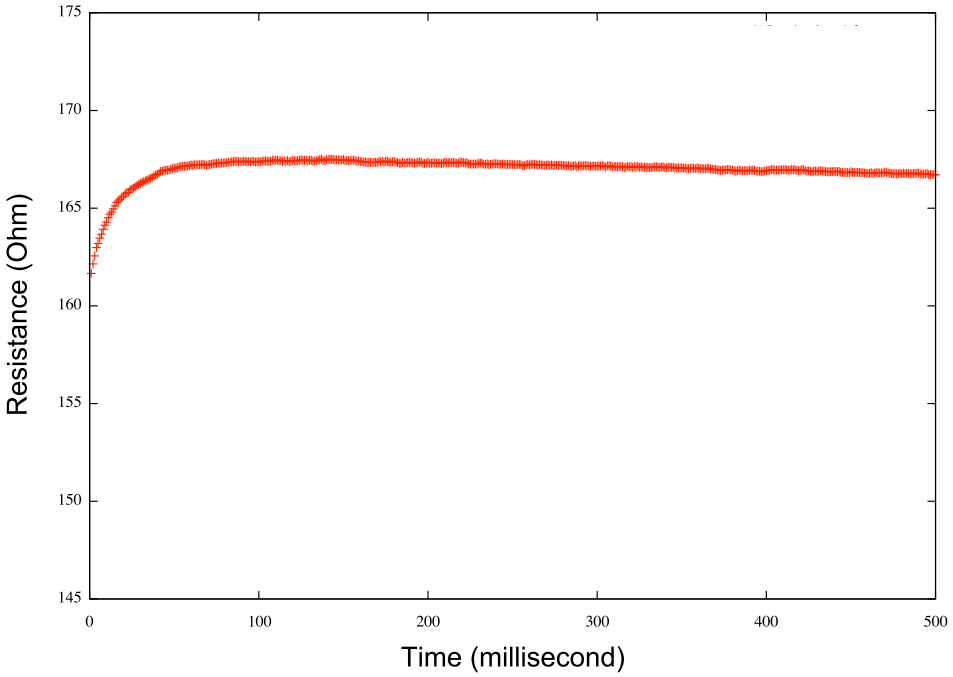

Figure 5-13. *Electrical resistance – time curve of a MWCNT when a voltage of 1 V is applied on.*

Figure 5-13 shows the electrical resistance with time after a voltage of 1 V was applied on the MWCNT. The high temperature from Joule heating increased the electrical resistance of the MWCNT to 167 Ohm from 162 Ohm. The electrical resistance and temperature of the MWCNT were thermally stable after several ten milliseconds. The heating rate was faster than that of Pt hot-wires (~140 milliseconds).

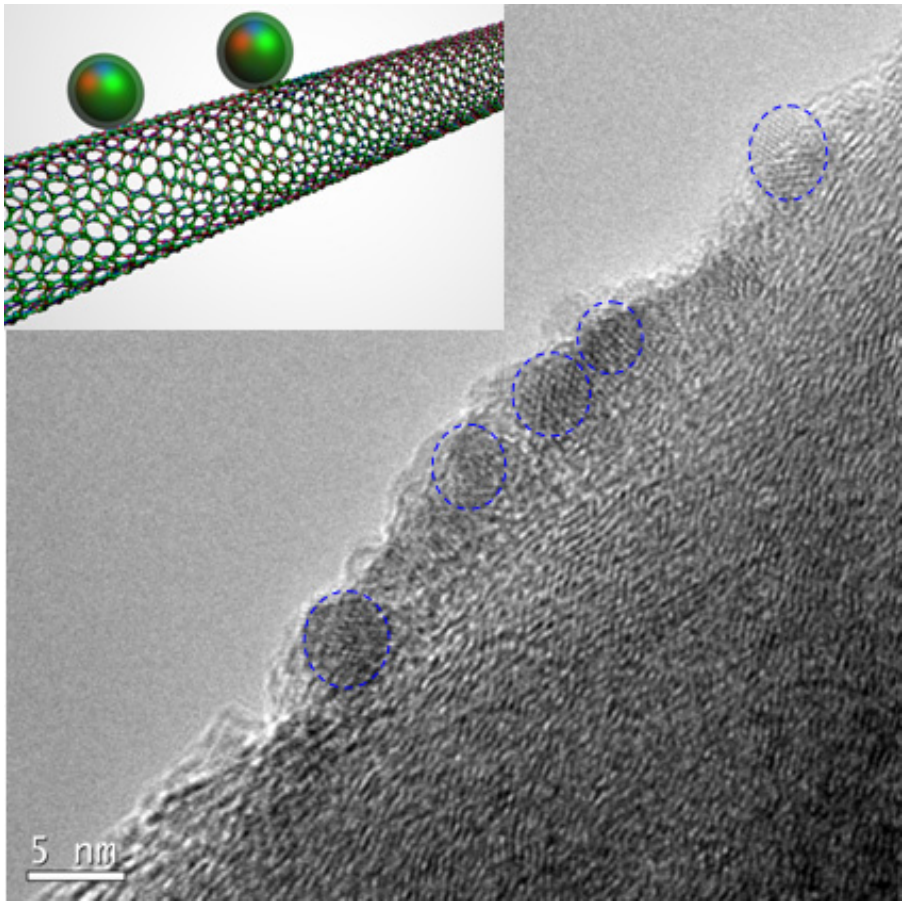

Figure 5-14. *HRTEM image of QDs on MWCNT surface. The QDs were deposited on the CNT surface. Inset: 3-D image of CdSe/ZnS QDs on a CNT*

Because the mass of CNT is very light and the thermal conductivity of CNT is very high, the CNT can be heated up to 1000 °C in one millisecond. The temperature ramp-down time is also one millisecond. So the QDs deposited on CNTs can be fast heated in one millisecond. The heating time can be controlled from second milliseconds to several minutes. Therefore such a CNT heater is an ideal fast-heating nanodevices to study dynamic properties at nanoscale.

Figure 5-14 shows an HRTEM image of QDs (circled) after being heated in vacuum. Compared with the unheated QDs, the diameter of individual QDs decreases.

The QDs deposited on CNT were also fast heated in air. Because CNTs are oxidized above 500 - 700 °C in air, the fast heating temperature was controlled below 500 °C in air.

There are lots of defects in CNTs and electrical resistances of individual CNT is different case by case. Therefore it is hard to calibrate the temperature of individual CNTs. However CNTs provide a possible method to fast heat nanoparticles.

5.4. New TEM grids

The nanoparticles are usually heated in vacuum or in air on TEM grids. The conventional TEM grids are not thermally stabile under our heating procedure and the heated nanoparticles are always dropped from the TEM grids. In order to obtain a stable film supporter, new TEM grids coated with ultra-thin amorphous Al_2O_3 films have been developed using atomic layer deposition technique.

5.4.1. Conventional TEM grids coated with carbon film

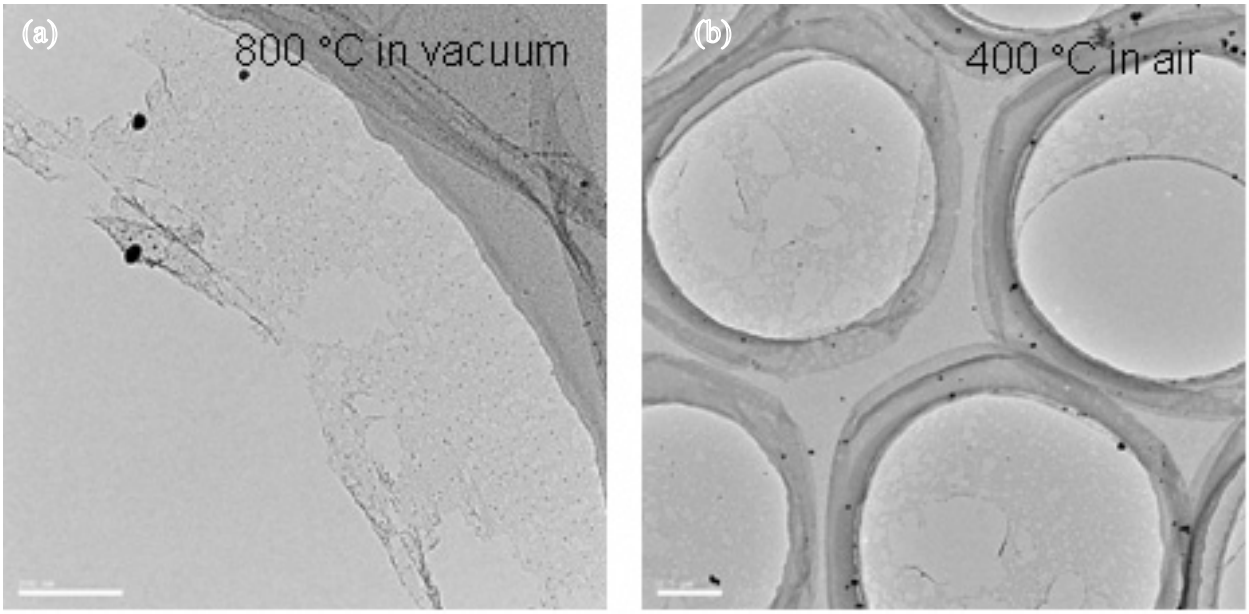

Figure 5-15. *TEM images of commercial carbon-coated TEM grids. Heated at (a) 800 °C in air or (b) 400 °C in air.*

The commercial conventional TEM grids are consisted of a ultra-thin carbon amorphous film deposited on a holey carbon film, both of which are deposited on a TEM metal grid. This kind of conventional TEM grids are widely used at low temperatures, room temperature and medial temperature less than 400 °C. In our heating experiments of nanoparticles, such carbon coated TEM grids are always broken in vacuum, especially in air because of physical properties of carbon amorphous films. Figure 5-15 shows the conventional TEM grids after heating in vacuum or in air. The carbon ultra-thin films were broken after being heated at 800 °C in vacuum or 400 °C in air. The carbon films were totally burn off when heated at 450 °C in air. The nanoparticles deposited on carbon films dropped from the supporting films after being heating.

The ultra-thin carbon films are not stable in some solutions either. For example, when CdSe/ZnS QDs suspending in toluene are deposited on the commercial TEM grids, the ultra-thin carbon films are always damaged. In order to find a thermally and chemically stable TEM grids for our fast-heating experiments, a new kind of oxide films were developed.

5.4.2. ALD coating of Al_2O_3 films on TEM grids

In a typical coating of Al_2O_3 films, commercial holey carbon TEM grids coated with a continuous ultra-thin carbon film were loaded into an atom-layer-deposition (ALD) chamber, pumped down to 1×10^{-3} Pa, and heated to 120 °C. Then an Al_2O_3 amorphous film was deposited on the carbon coated TEM grids, using water and trimethylaluminum (TMA) as the sources for oxygen and aluminum, respectively. The ALD process was performed by alternatively supplying pulses of nitrogen gas containing water and TMA with each cycle consisting of a 15 milliseconds water pulse, a 5 second nitrogen purge period, a 15 millisecond TMA pulse, and a 5 second nitrogen purge period. The deposition rate of Al_2O_3 was 0.10 nm per cycle. The thickness of the amorphous Al_2O_3 film was controlled by the cycle number. After deposition, the TEM grids were cooled down to 100 °C, taken out from the ALD chamber, plasma cleaned, and heated in air at 300 °C to burn the continuous ultra-thin carbon film over the holes of the holy carbon film that were exposed to air. Figure 5-16 shows the procedure of the ALD coating.

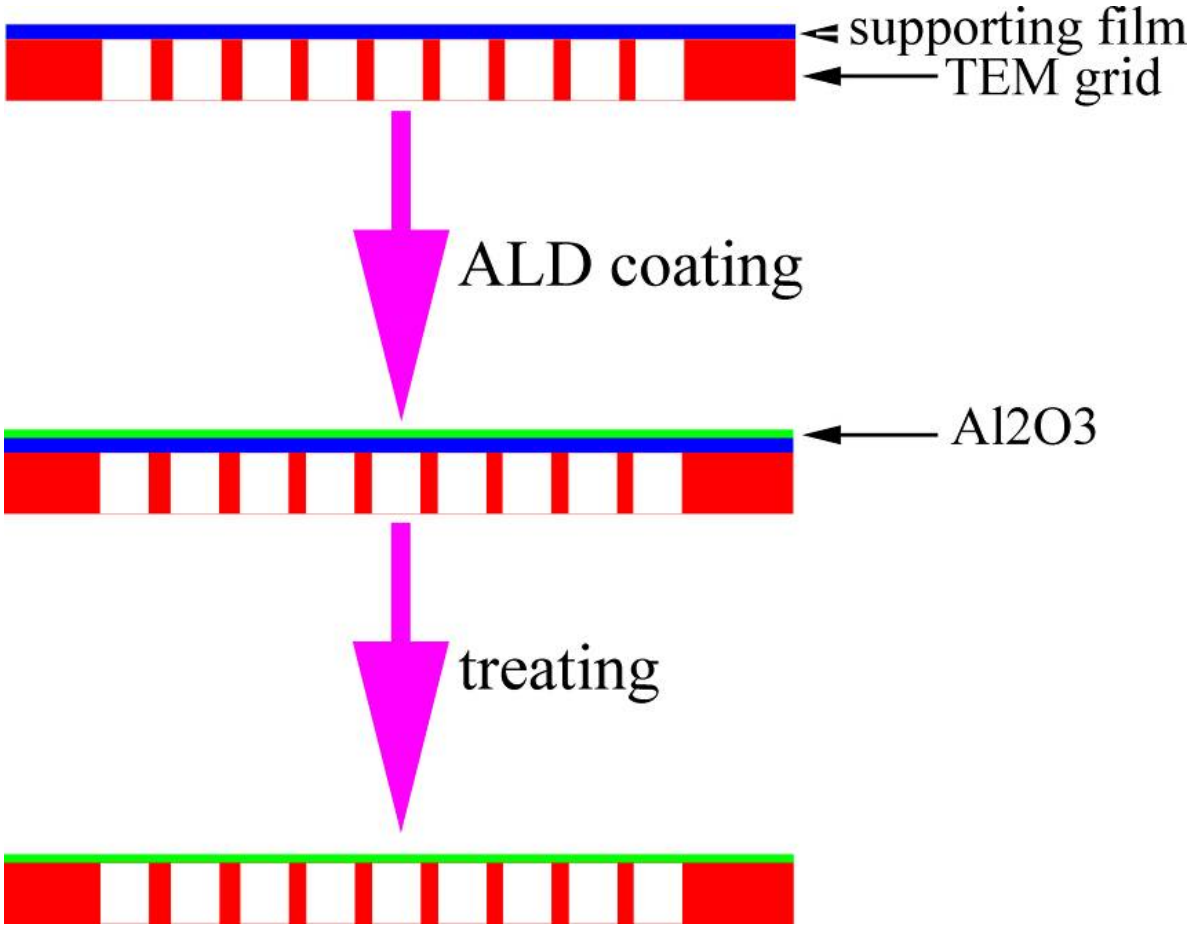

Figure 5-16. *Experimental procedure of ALD Al_2O_3 coating on TEM grids.*

5.4.3. Al_2O_3 coated TEM grids

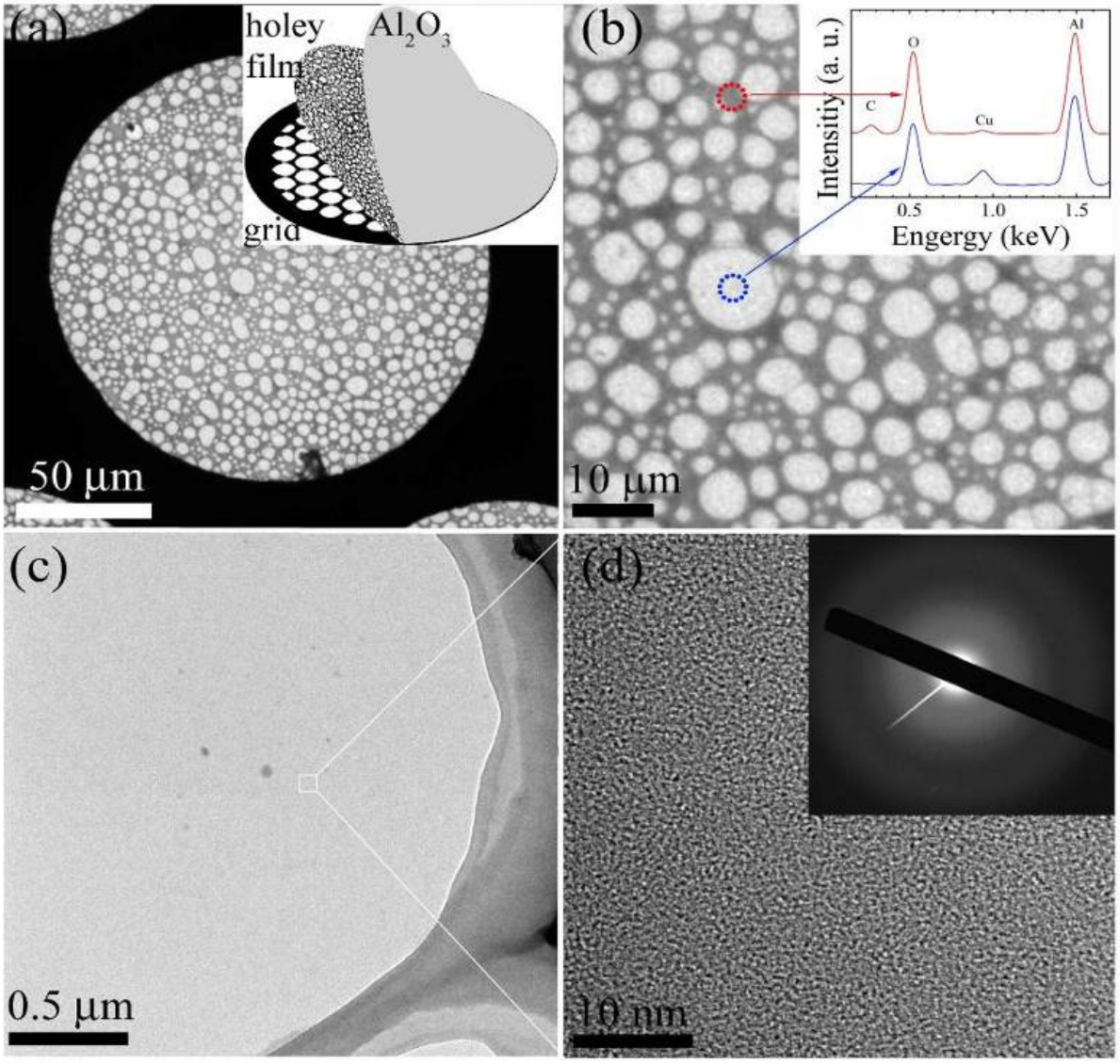

Figure 5-17. *TEM images of ALD Al_2O_3 films with thickness of 2 nm at (a) low magnification, (b) medium magnification, (c) high magnification, and (d) HRTEM. Inset in (a) illustrates the layer-structure of the coated TEM grid with part of the Al_2O_3 film and holey carbon film raised for viewing purpose. Inset in (b) is EDS of the ALD film. The top spectrum comes from the holey carbon region while the bottom one from the thin Al_2O_3 film region. Inset in (d) is SAED of the Al_2O_3 film.*

Figure 5-17 is a plan-view of an ALD coated TEM grid with an amorphous Al_2O_3 film deposited

with 20 cycles. Inset in Figure 5-17a illustrates the layer-structure of the ALD coated TEM grids: consisting of continuous Al_2O_3 film (partly raised for viewing purpose), holey carbon film (partly raised for viewing purpose), and the TEM copper grid. The thickness of the Al_2O_3 film was about 2.0 nm. The ALD Al_2O_3 film was continuous and covered the whole TEM grid of 3.05 mm in diameter (Fig. 5-17a-c). Energy-dispersive X-ray spectroscopy (EDS) of the ALD film over a hole of the holey carbon film indicated that the ALD film was consisted of oxygen and aluminum without carbon within the experimental errors (bottom curve in inset of Figure 5-17b). EDS spectrum (top curve in inset of Figure 5-17b) also indicated that the holey carbon film was still there. The holey carbon film supported the ALD Al_2O_3 film. The ratio of aluminum and oxygen was 2.0 : 3.2 calculated from EDS, close to the ideal ratio of 2.0:3.0. The slightly high oxygen content may come from the oxygen absorbed on the ALD film surfaces. The ratio of aluminum and oxygen was spatially uniform on the whole ALD film.

HRTEM and selected area electron diffraction (SAED) (Figure 5-17c-d) indicated that the ALD Al_2O_3 film was amorphous. HRTEM of the ALD film did not show any thickness contrast, indicating the thickness of the Al_2O_3 film was uniform at nanoscale.

5.4.4. Thermal stability of Al_2O_3 coated TEM grids under high temperatures

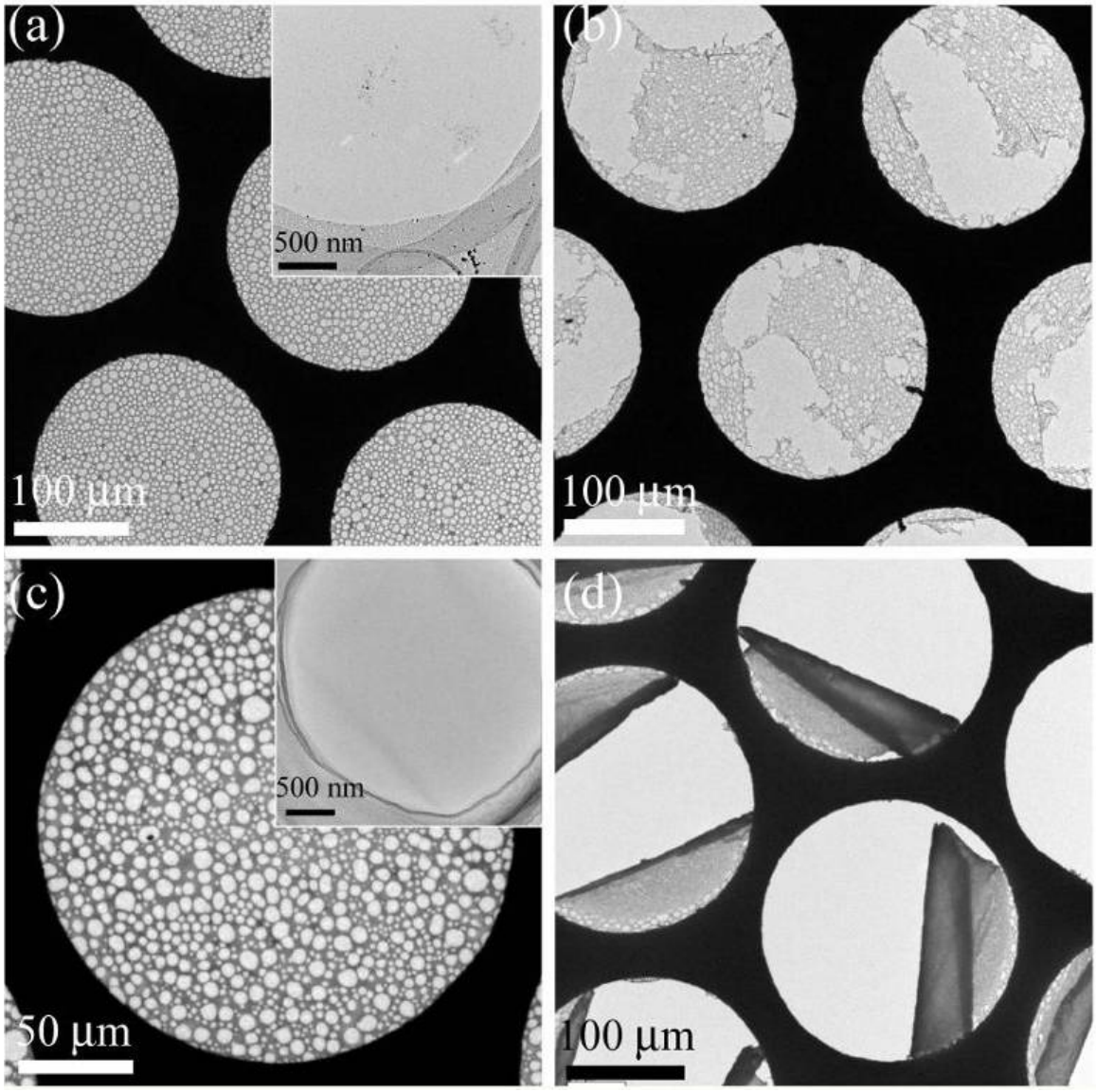

Figure 5-18. *Low magnification TEM images of ALD Al_2O_3 films with 2 nm thickness heated at (a) 600 °C in air, (b) 700 °C in air, (c) 900 °C in vacuum, and (d) 985 °C in vacuum. The insets in (a) and (c) are TEM images of the Al_2O_3 film at medium magnification.*

The ultra-thin ALD Al_2O_3 film is mechanically stable at high temperature in air and in vacuum. Figure 5-18 is a plan-view of the amorphous ALD Al_2O_3 films after being heated at various temperatures. The amorphous Al_2O_3 film was still continuous after being heated at 600 °C for 5 minutes in air (Figure 5-18a). SAED indicated that the ALD film was still amorphous after being heated. After being heated at 700 °C for 5 minutes in air, big voids were formed in the ALD film and the ALD Al_2O_3 film was broken (Figure 5-18b).

The ALD Al_2O_3 films were more mechanically stable in vacuum ($<1\times 10^{-3}$ Pa) than in air. After being heated at 900 °C for over 10 minutes in vacuum, the morphology of the ALD Al_2O_3 film

was same as before being heated (Figure 5-18c). The heated ALD Al_2O_3 film was still amorphous. After being heated at 985 °C for 10 minutes in vacuum, the ALD Al_2O_3 film broke and rolled up (Figure 5-18d).

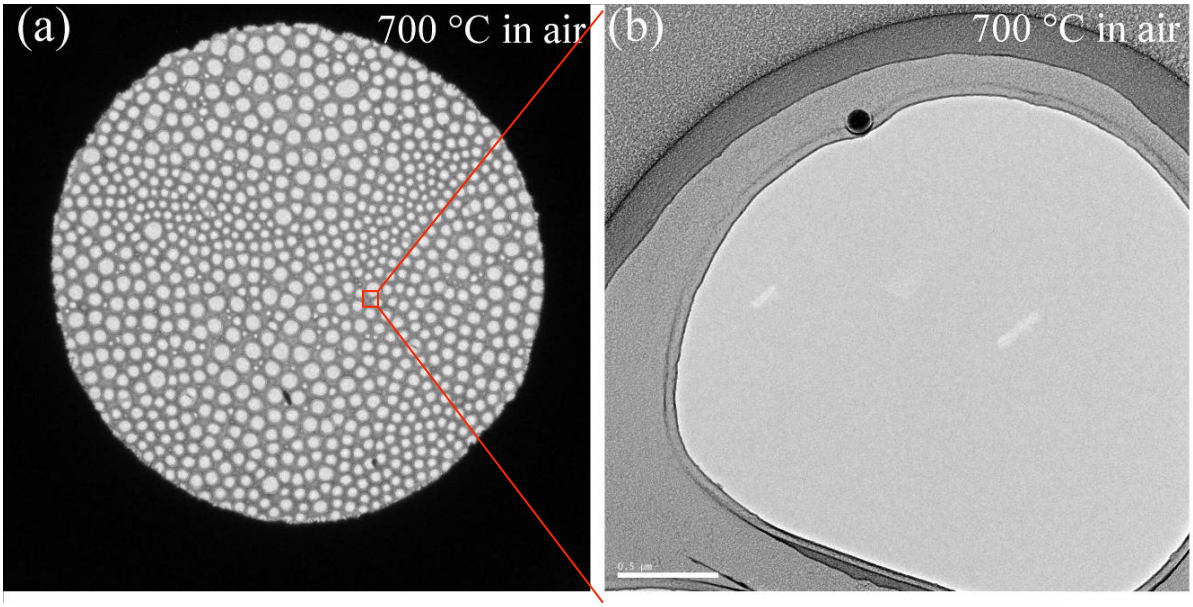

Figure 5-19. *TEM images of an ALD film after being heated at 700 °C in air.*

The mechanical stability of the Al_2O_3 films depends on the thickness of the Al_2O_3 films. Figure 5-19 shows ALD films with thickness of 10 nm after being heated at 700 °C in air. The thicker films were more thermally stable and no voids were observed on the films. Therefore the thick films were more mechanically stable. The amorphous film with 10 nm thickness was mechanically stable above 1200 °C in vacuum.

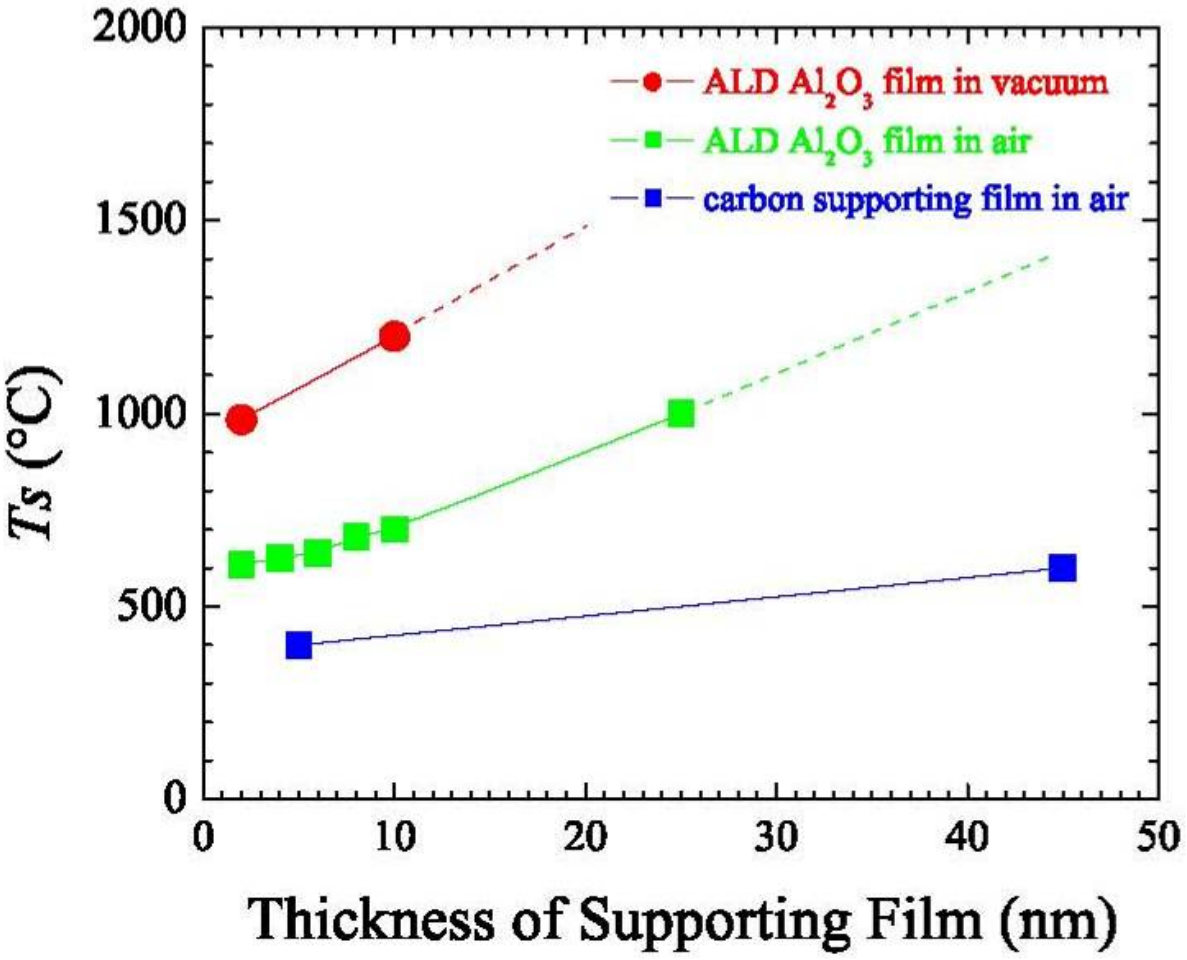

Figure 5-20. *Mechanical stability dependence of thickness of ALD Al_2O_3 films with data of carbon supporting films for comparison.*

Here we define a mechanically stable temperature T_s at which the ALD Al_2O_3 films break. Figure 5-20 shows the thickness dependence of T_s. TEM observation indicated the thicker the ALD Al_2O_3 films, the higher the *Ts*. For example, the ALD Al_2O_3 films with 10 nm thickness were mechanically stable up to 700 °C in air while the film with 25 nm thickness was mechanically stable up to 1000 °C in air. The mechanical stable temperature is higher in vacuum.

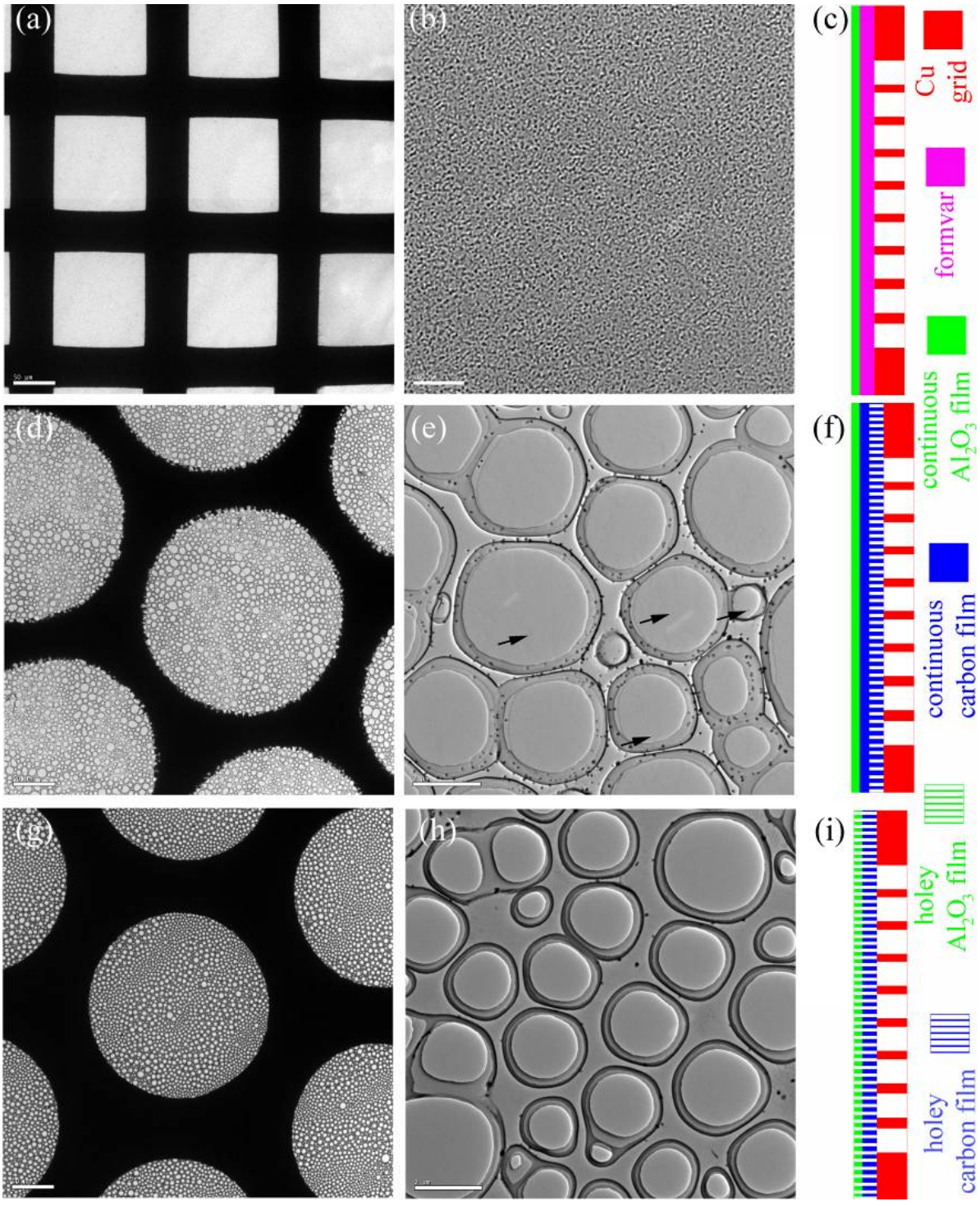

Figure 5-21. *Various ALD Al_2O_3 films with different structures. a), d), g): TEM images of TEM grid with coating Al_2O_3 films; b), e), h): TEM image of Al_2O_3 films; c), f), i): Cross-sectional structures of the TEM grids. a)-c): continuous Al_2O_3 film coated on a formvar film that deposited on TEM grids; d)-f): continuous Al_2O_3 film coated on a holey carbon film that deposited on TEM grids; g)-i): holey Al_2O_3 film coated on holey carbon film that deposited on TEM grids.*

Several kinds of Al_2O_3 supporting films were coated on TEM grids. Figure 5-21 shows several prepared TEM grids coated with 50 nm Al_2O_3 films. The Al_2O_3 films were continuous or holey, deposited directly on TEM grids or deposited on other supporting films like carbon films or formvar films. The continuous Al_2O_3 supporting films can be used for *in situ* high temperature HRTEM experiments of nanoparticles and holey Al_2O_3 supporting films for high temperature experiments of nanowires. The sandwiched carbon films or formvar films strengthened the mechanical properties of the Al_2O_3 supporting films.

5.4.5. *In situ* heating of nanoparticles on ALD Al_2O_3 TEM grids

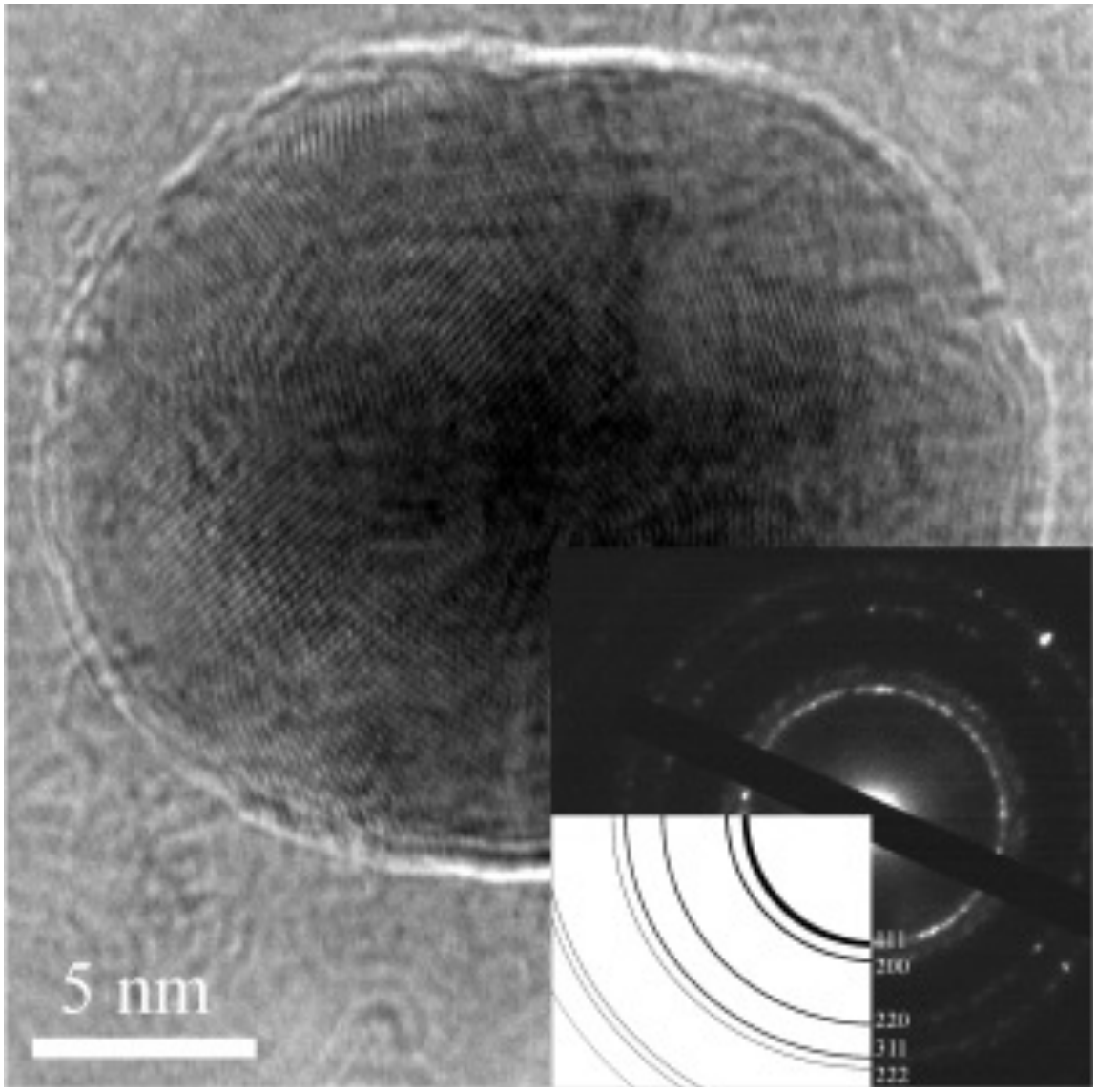

***Figure 5-22**. In-situ HRTEM image of a silver nanoparticle taken at 500 °C in vacuum. Inset: SAED pattern of the nanoparticle taken at 500 °C.*

As a test of the ALD Al_2O_3 amorphous films, silver nanoparticles with a diameter of less than 20 nm were deposited on an ALD Al_2O_3 amorphous film and heated *in-situ* up to 900 °C in vacuum. Figure 5-22 shows an *in-situ* HRTEM image and SAED of a silver nanoparticle taken at 500 °C in vacuum showing the polycrystalline nature of the silver nanoparticle. Quality of the obtained HRTEM image was almost same as those obtained using the conventional ultra-thin carbon films with thickness of several nanometers. The diffraction halos of the ALD Al_2O_3 film were very weak and hardly seen under our experimental conditions (inset of Figure 5-22).

Compared with other TEM supporting films, the ALD-Al_2O_3 films are more suitable for

HRTEM imaging of nanoparticles at high temperatures. The amorphous Al_2O_3 films can withstand temperatures over 600 °C in air and 900 °C in vacuum when the thickness of the Al_2O_3 film is 2 nm, and up to 1000 °C in air when the thickness is 25 nm, which makes possible heating TEM grids with nanoparticles up to 1000 °C in air and immediate TEM observation without interrupting the nanoparticles. The ALD films not only mechanically support the observed nanoparticles at high temperatures but also are thin enough for HRTEM imaging. Such coated TEM grids are very much desired for applications in high-temperature high-resolution transmission electron microscopy. The ALD-Al_2O_3 films can be fabricated much easier and massively produced in a short time. The Al_2O_3 supporting films are much cheaper than the present commercial coated TEM grids.

5.4.6. Heating Ag nanoparticles in air

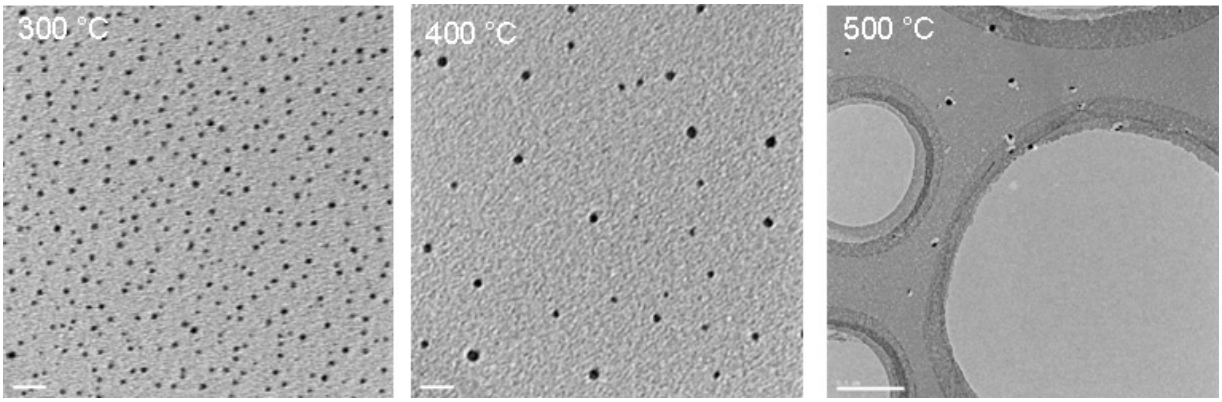

Figure 5-23. *Ex-situ TEM images of Ag nanoparticles heated at different temperatures in air.*

Using Al_2O_3 ultra-thin supporting films, Ag nanoparticles were heated for 2s in air and then examined on TEM at room temperature. Figure 5-23 shows the TEM image of the heated Ag nanoparticles. The areal density of the Ag nanoparticles decreased with increasing temperature and most of the nanoparticles disappeared at 500 °C in air.

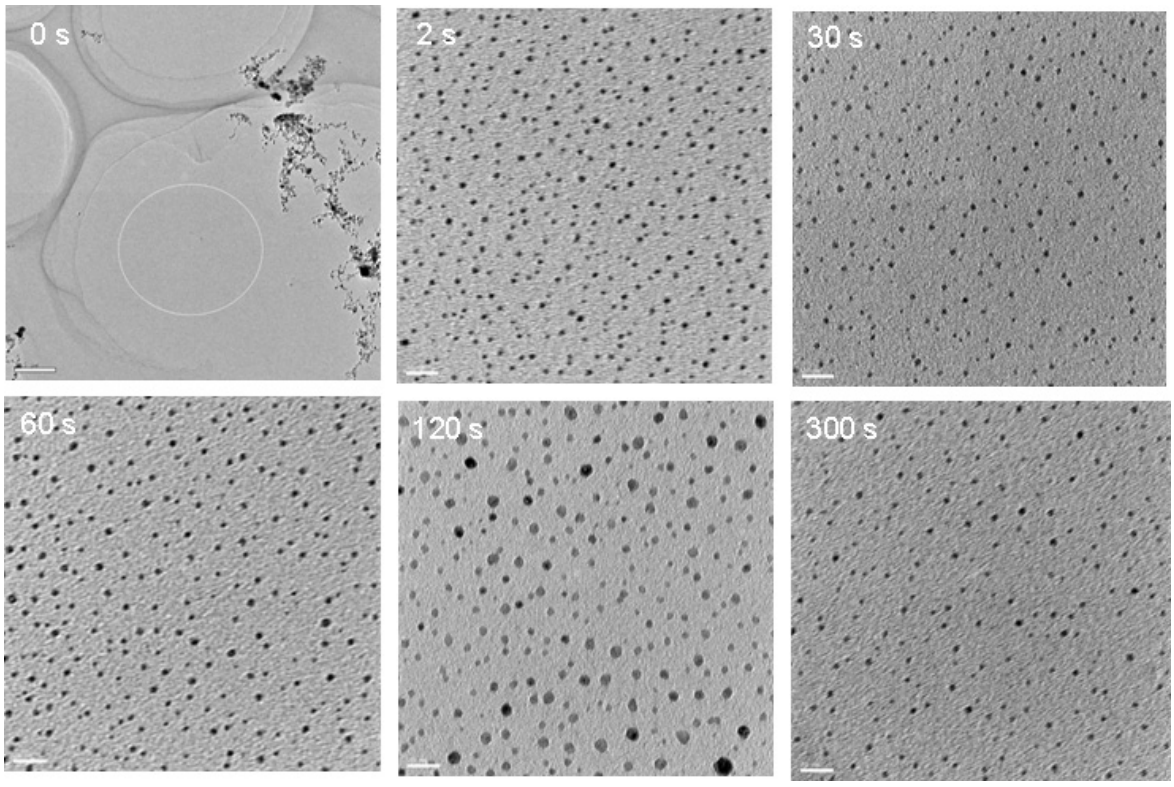

Figure 5-24. *Ex-situ TEM images of Ag nanoparticles heated at 300 °C in air for different heating time.*

Ag nanoparticles were also examined at different heating time. Figure 5-24 shows TEM images of Ag nanoparticles heating from 0s to 300s at 300 °C in air. The nanoparticles were heated in a tube furnace and observed on TEM at room temperature. Each TEM sample experienced only one certain heating temperature. Figure 5-24 indicates that the heating time also affect the morphology of the silver nanoparticles.

5.5. Internal temperature calibration in heating TEM

In the above *in-situ* and *ex-situ* HRTEM observations, the heating temperatures were calibrated externally and at macroscale. In our heating experiments, all the QDs were heated at nanoscale. So it is necessary to calibrate temperature fields at nanoscale. In order to measure the heating temperature at nanoscale, we calibrated temperature fields at nanoscale internally.

During the calibration of temperature fields, PbTe nanocubes were employed as the internal standard.

5.5.1. Morphology of PbTe nanocubes at high temperatures

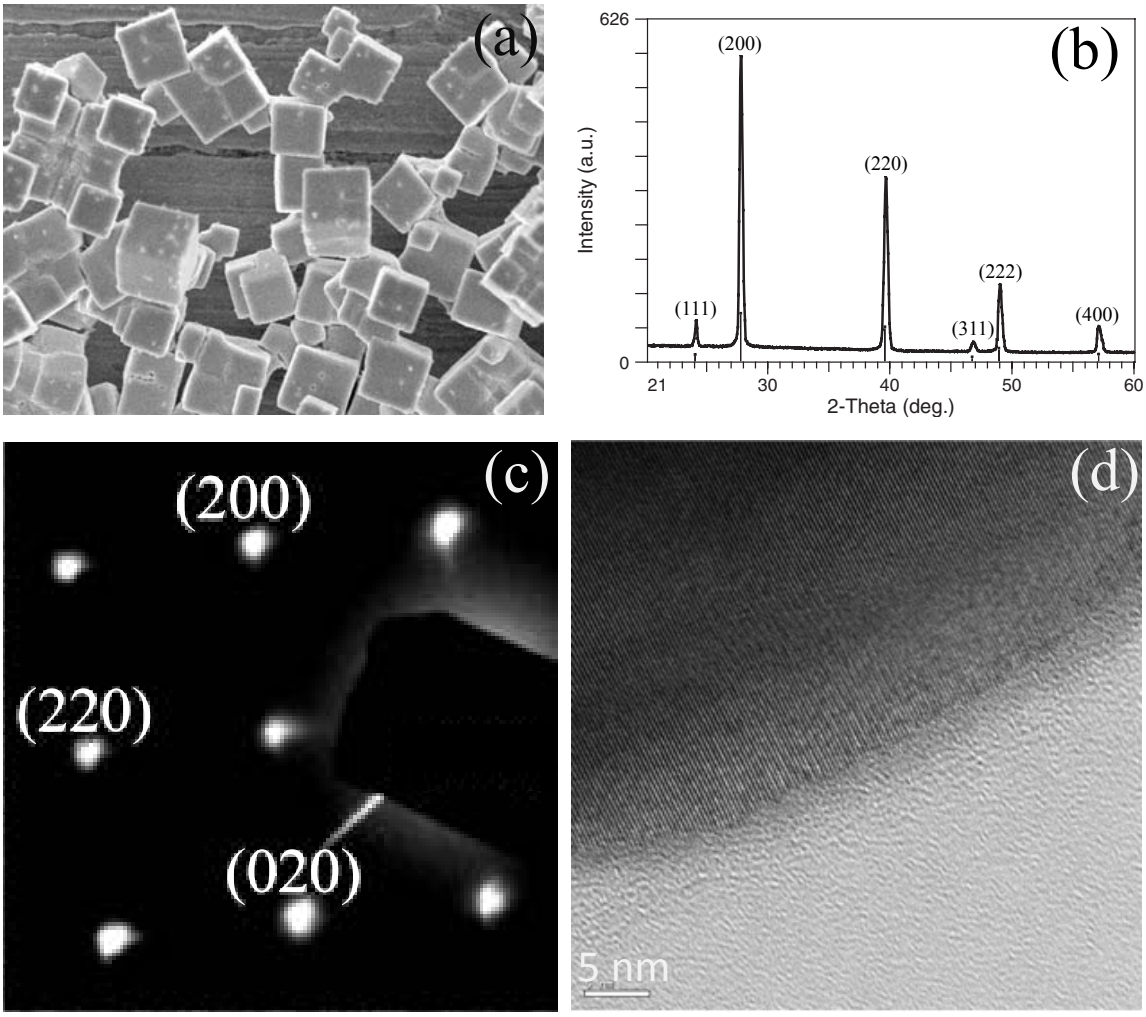

Figure 5-25. *PbTe nanocubes. (a) SEM image, (b) X-ray diffraction pattern, (c) SAED pattern of one nanocube, and (d) HRTEM image of a PbTe cube edge.*

Figure 5-25 shows the synthesized nanocubes. The scanning electron microscopic (SEM) image shows that the PbTe nanomaterials are nanocubes with perfect corners, edges, and facets. The X-ray diffraction pattern indicates that the nanomaterials are PbTe with $Fm\bar{3}m$ space group. Selected area electron diffraction (SAED) shows the nanocubes are crystalline. HRTEM studies further confirmed that the PbTe nanocubes crystallized very well. The perfect PbTe nanocubes were employed as internal TEM temperature calibration standards here.

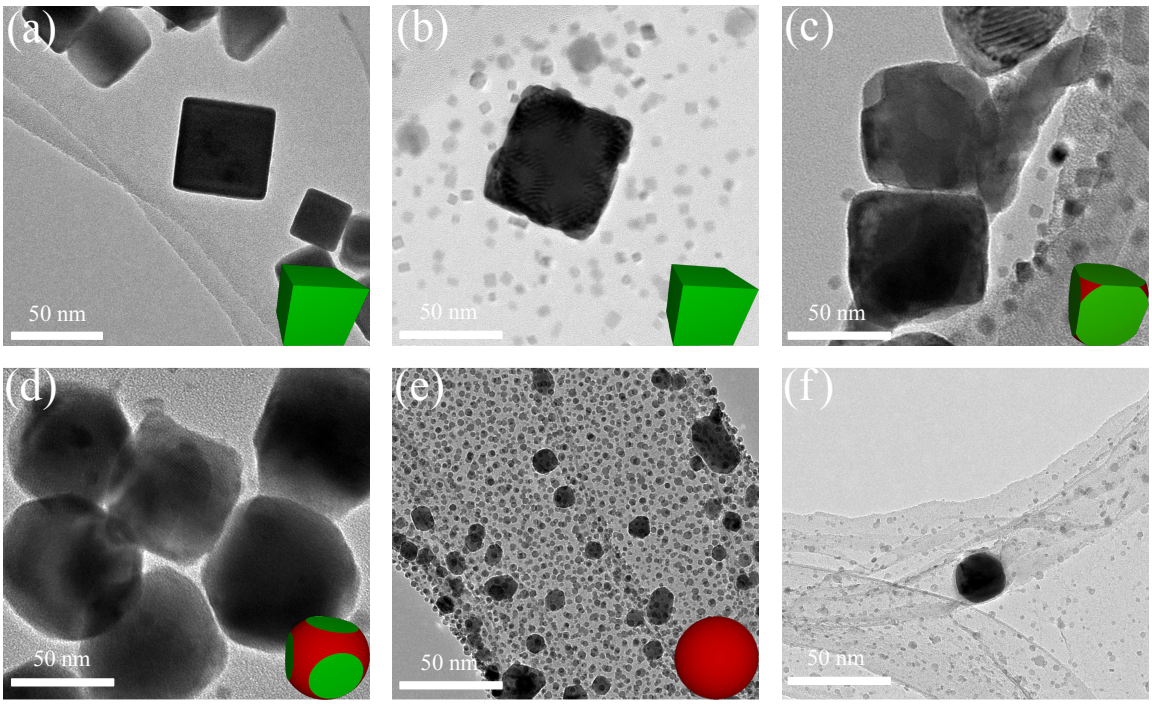

Figure 5-26. *TEM images of heated PbTe nanocubes heated in quartz tubes at different temperatures T* for 5 min at (a) room temperature, (b) 300 °C, (c) 340 °C, (d) 375 °C, (e) 400 °C, and (f) 450 °C. The temperatures T* were measured by a thermocouple located inside the tube furnace. TEM images were ex situ taken at room temperature. Some small particles re-deposited around PbTe cubes during cooling in (b)-(e). Insets: 3D morphology of nanocubes at different temperatures.*

Figure 5-26 shows TEM images of PbTe nanocubes heated in evacuated quartz tubes. Morphology of the PbTe nanocubes changed with the heating temperature T^* measured by furnace controller. Figure 5-26a shows a perfect PbTe nanocube before being heated. The sealing procedure of quartz tubes did not affect the prefect morphology of the PbTe nanocubes. Figures 5-26b-f show PbTe nanocubes heated for 5 min in evacuated quartz tubes. The morphology of the nanocubes was stable up to 300 °C (Figure 5-26b). The corners of the nanocubes were rounded at 340 °C because of the melting of corners (Figure 5-26c), T^*_{corner} = 340 °C. When the heating temperature T^* was 375 °C, the edges of the nanocubes began to melt (Figure 5-26d, T^*_{edge} = 375 °C) while the corners melt further. The facets of the nanocubes began to melt at 400 °C (Figure 5-26e), T^*_{facet} = 400 °C. Once taken out of the furnace and cooled to room temperate, the vapor of PbTe deposited on the TEM grids, forming many smaller particles (size: < 20 nm), as shown in Figure 5-26e. At higher temperatures, the PbTe nanotubes totally decomposed and the vapor would deposit onto quartz tubes and the PbTe nanotubes disappeared completely on TEM grids (Figure 5-26f). The observed temperature-depend morphology is in agreement with the predication of the depressed melting temperature model of semiconductors. The theoretical model predicates that the melting of crystallographic surfaces strongly depends on the radius of surface curvature. The corners, edges, and facets of PbTe nanocubes have a small, medium, and large radius of curvatures, respectively, resulting in different melting temperatures.

5.5.2. Ex situ temperature calibration

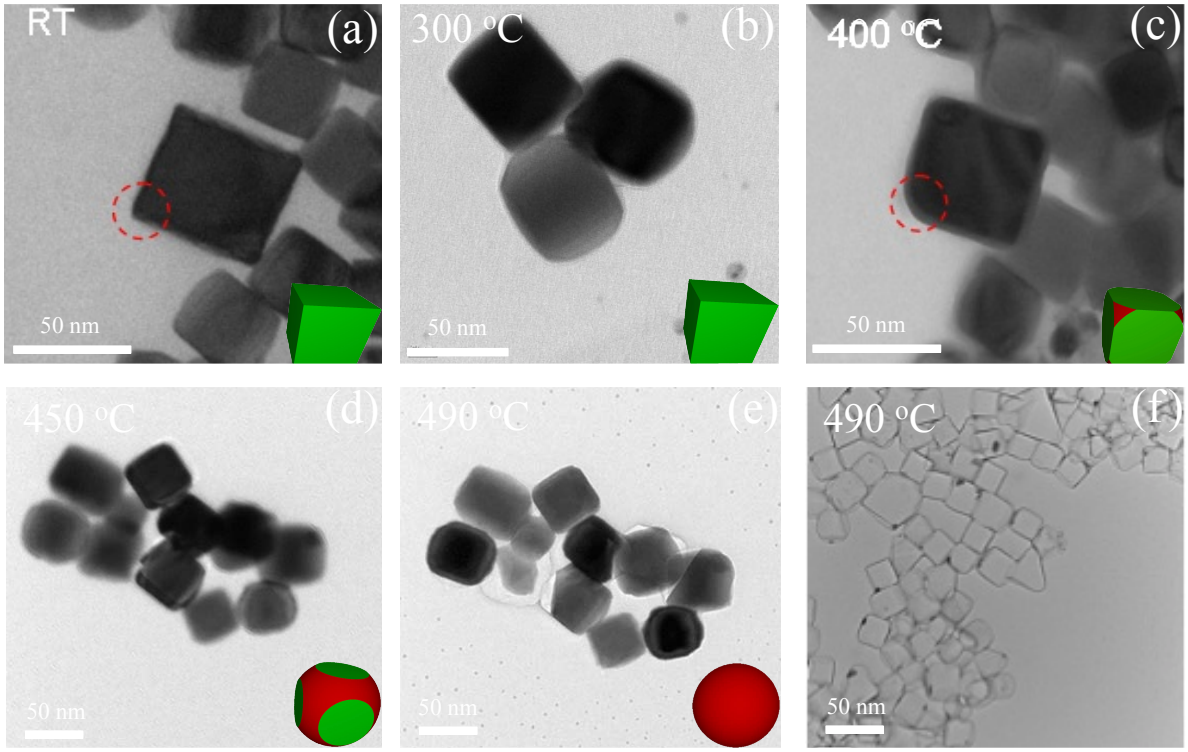

Figure 5-27. *TEM images of PbTe nanocubes in situ heated at different temperature T' for 5 min at (a) room temperature, (b) 300 °C, (c) 400 °C, (d) 450 °C, (e) 490 °C (for 2 s), and (f) 490 °C. The temperature T' was measured by a thermocouple integrated into the TEM heating holder. Insets: 3D morphology of PbTe nanocubes at different temperatures.*

Figure 5-27 shows TEM images of PbTe nanocubes being heated in TEM at different temperatures T' in vacuum. The temperature T' was measured by the hot-stage controller connected to the TEM heating holder. TEM images were *in situ* taken at high temperatures.

Figure 5-27a shows that the as-synthesized nanocubes are perfect cubes with edge length of 50 nm, in agreement with SEM observations. Morphology of the nanocube does not change below 350 °C regardless the heating time (Figure 5-27b).

Once the heating temperature *T'* increased to 400 °C, the corners of the nanocubes got rounded (Figure 5-27c). Between 350 °C and 400 °C, no morphological change was observed with heating time at the TEM magnification. This means that the corners melt at 400 °C, T'_{corner} = 400 °C. The edges of the nanocubes melt at about 450 °C (T'_{edge} = 450 °C), and facets at 500 °C (T'_{facet} = 500 °C). Between 400 – 450 °C, the radius of curvatures of the rounded corners increased with time at the first one minute and then were roughly constant with heating time. Between 450 – 500 °C, the radius of curvatures of the rounded edge were only dependent on the heating temperature while not on heating time after 5 minutes.

The PbTe nanocubes evaporated very quickly above 490 °C. Figure 5-27e shows a typical TEM image at 490 °C for the first 10 seconds. The PbTe nanocubes began to melt. The

morphology of the PbTe nanocubes changed quickly with heating time. All PbTe nanocubes evaporated at the temperature after 1 min and only some traces were observed (Figure 5-27f).

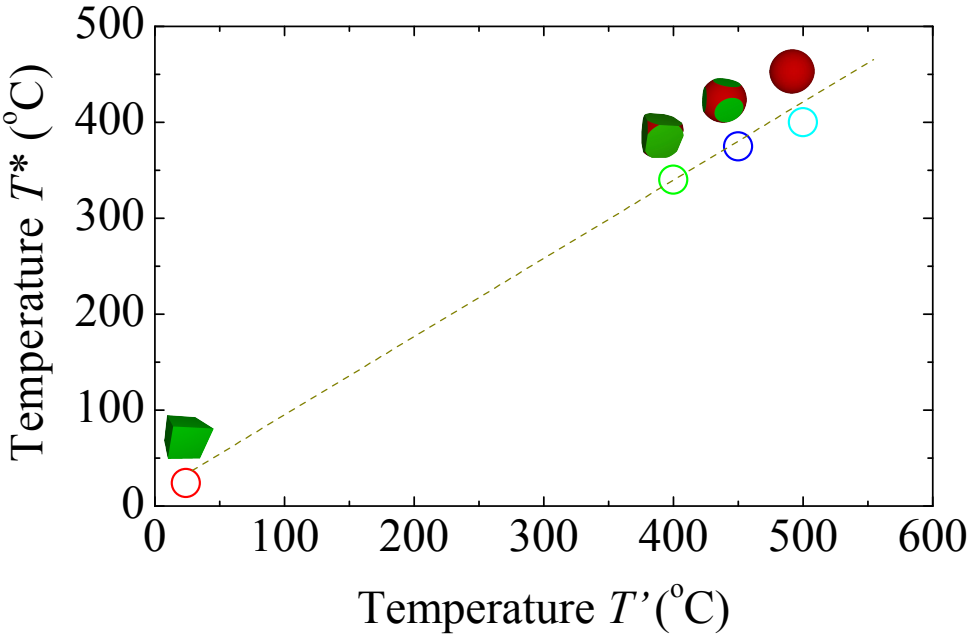

Figure 5-28. *Ex situ calibration curve of temperature. T': measured by the TEM hot-stage controller. T*: measured by the thermocouple of furnace.*

The temperature T' measured from the hot-stage controller can be *ex situ* calibrated from the relationship between T' and T^*. Theoretically the three critical temperatures should be equal respectively, $T'_{corner} = T^*_{corner}$, $T'_{edge} = T^*_{edge}$, $T'_{facet} = T^*_{facet}$. Figure 5-28 plots the relationship between T^* and T'. From Figure 5-28, we obtained

$$T^* = 0.83 \times T' + 5 \qquad (2)$$

Thus the macroscopic temperature of the TEM heating holder T' can be *ex situ* calibrated from the PbTe nanocubes. The accurate temperature T^* exposed on the PbTe nanocubes is lower than T' measured from the TEM heating holder.

5.5.3. In situ temperature calibration at nanoscale

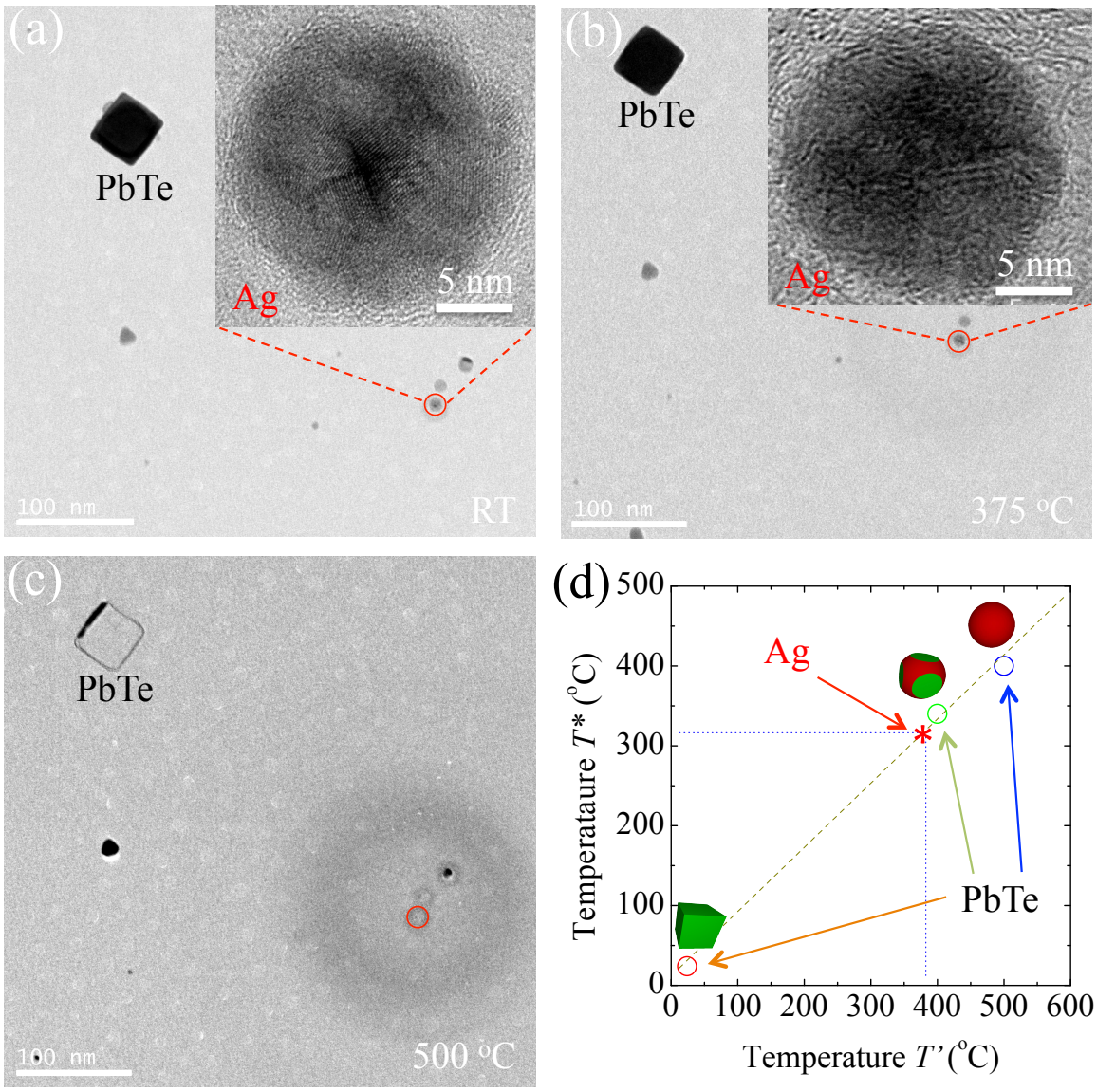

Figure 5.29. *In situ temperature calibration at nanoscale on TEM. In situ TEM images of a PbTe nanocube and a silver nanoparticle at (a) room temperature, (b) 375 °C at which temperature the Ag nanoparticle melts, and (c) 500 °C at which temperature the PbTe nanocube melts. Insets in (a-b): in situ HRTEM images of a silver nanoparticle taken at the heating temperatures. (d) In situ calibration of the melting point of the silver nanoparticle. Insets: morphology of the PbTe nanocubes at different temperatures. *: melting point of the Ag nanoparticle with a diameter of 15 nm.*

Figure 5-29 shows TEM images of entire calibration procedures in which silver nanoparticles were deposited on TEM grids with PbTe nanotubes. Figure 5-29a shows a TEM image at room temperature. A perfect PbTe nanocube was located near a silver nanoparticle as an internal

temperature calibration standard, just 500 nm away from the silver nanoparticle. The HRTEM image (inset in Figure 5-29a) indicated that the silver nanoparticle was single crystalline at room temperature. The silver nanoparticle was then *in situ* heated with the PbTe nanocube in the TEM heating holder. The heating temperature T' was measured by the hot-stage controller connected to the TEM heating holder. With the increasing temperature T', the surface of silver nanoparticle melt first and then totally melt at T' = 375 ^{o}C (Figure 5-29b). HRTEM images indicated no lattice fringe of the silver nanoparticle at the high temperature (inset in Figure 5-29b). SAED of the silver nanoparticle was consisted of diffraction rings (not shown here), and no any diffraction spots were observed, indicating the silver nanoparticle was liquid.

The morphology of the PbTe nanocube was unchanged at T' = 375 ^{o}C (Figure 5-29b) at which temperature the silver nanoparticle melt. Then the heating temperature T' was increased further until the morphology of the PbTe nanocube was changed at higher temperatures. The corners of PbTe nanocube melt first at T'_{corner} = 400 ^{o}C while the size of the silver nanoparticle became smaller because of evaporation. The PbTe nanocube totally melt at T'_{facet} = 500 ^{o}C and disappeared in several minutes at the temperature T'_{facet} (Figure 5-29c). The silver nanoparticle totally evaporated at the temperature T' = 500 ^{o}C.

Figure 5-29d plots the $T' - T^*$ relationship of the *in situ* heated PbTe nanocube. The measured melting point of the silver nanoparticle (T'_{Ag} = 375 ^{o}C) is also plotted on the curve. The melting point of the silver nanoparticle can be calibrated from the $T' - T^*$ curve. After calibration, the true depressed melting point of the silver nanoparticle T^*_{Ag} should be 324 ^{o}C, 50 ^{o}C lower than recorded by the TEM heating holder.

6. QD carriers with protection

We coated QDs with SiO_2 and integrated them into submicron spheres as QD carriers. These carriers would benefit from having a silica shell to impart wettability and biocompatibility. Silica can also be easily surface modified to link bioconjugators. Additional such individual QD carriers can be used as thermal history sensors.

6.1. Protective coating of CdSe QDs

We developed protective coatings for CdSe/ZnS QDs. This is necessary to minimize the environmental effect on the signals.

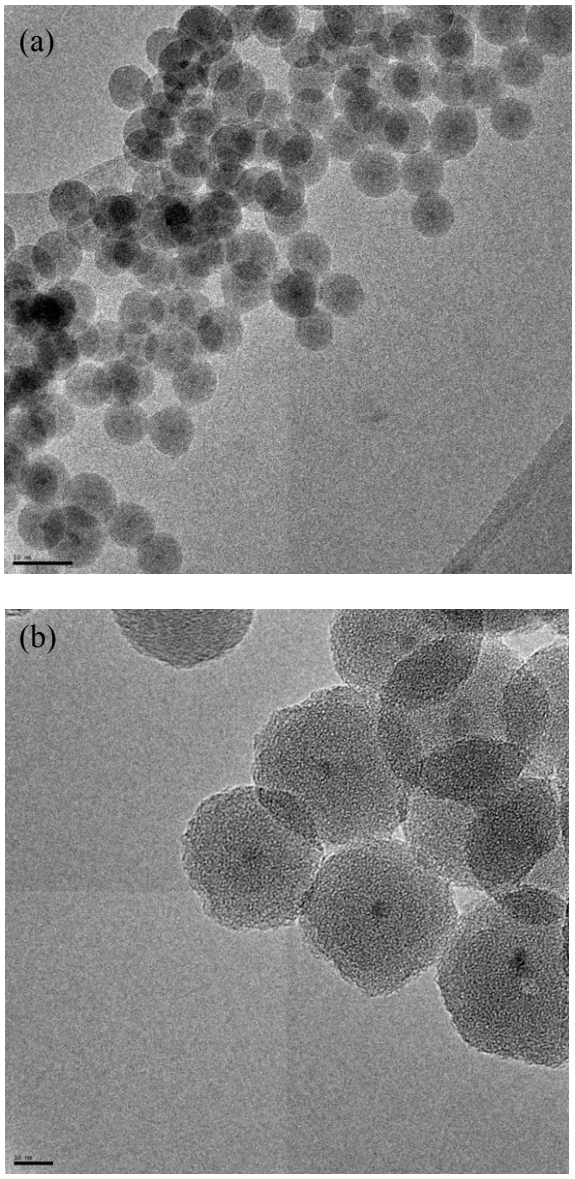

Figure 6-1. *TEM images of SiO_2 coated QDs at (a) low and (b) high magnification. The black dots are QDs.*

Figure 6-1 shows TEM images of the coated QDs. The quantum dots were encapsulated in thick silica shells by a reverse microemulsion approach. Silica-capped QDs were prepared from alkoxysilane. The silica shell thickness ranged from 2 - 5 nm to 40 - 80 nm, well controllable by reaction conditions.

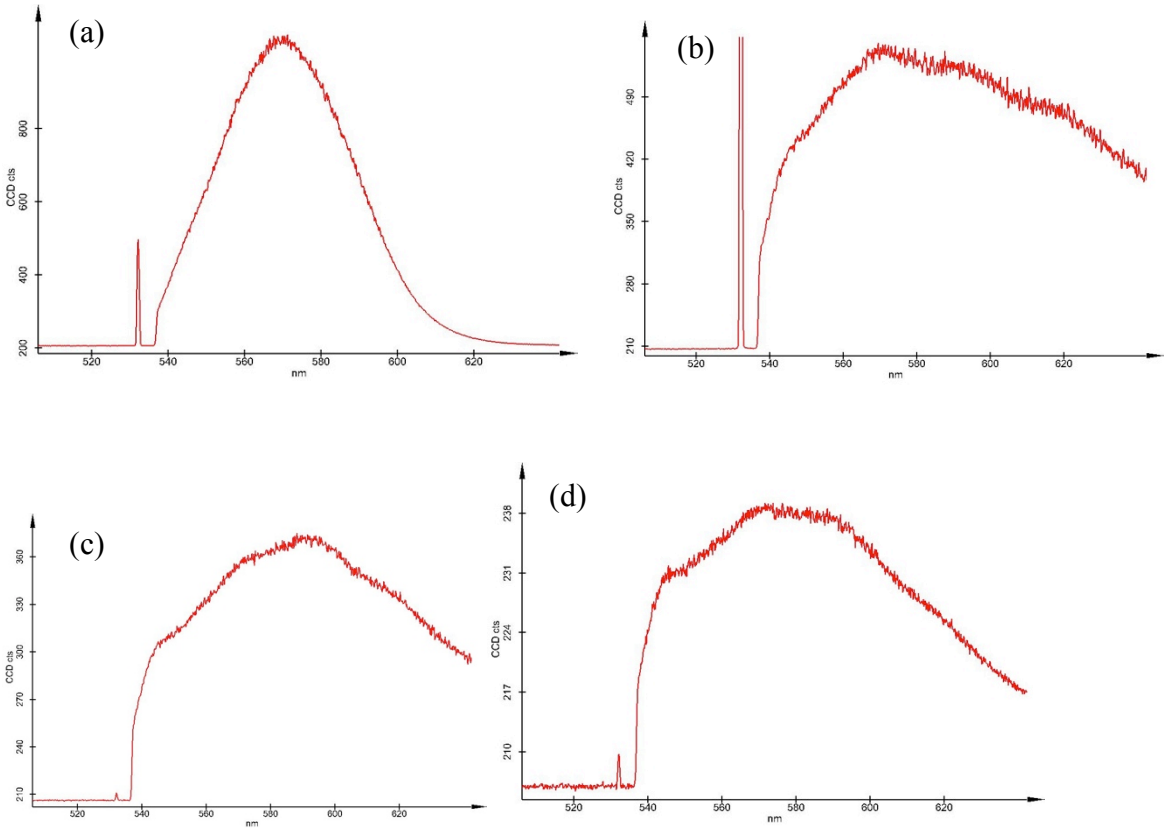

Figure 6-2*. PL spectra of QD carriers (a) before heating and heated at (b) 300 ^{o}C for 64 s, (c) 500 ^{o}C for 4 s and (d) 500 ^{o}C for 64 s.*

The PL peak wavelength of the carrier is 575 nm before being heated. Figure 6-2 shows PL spectra of heated QDs in air. The coated QDs were heated in air from 300 ^{o}C to 500 ^{o}C. After fast heated in air, the width of the PL peak obviously broadened. The broadening should come from 1) oxidization of CdSe QD embedding in SiO_2 coating and 2) temperature dependent peak shift.

6.2. Multiple QD carriers

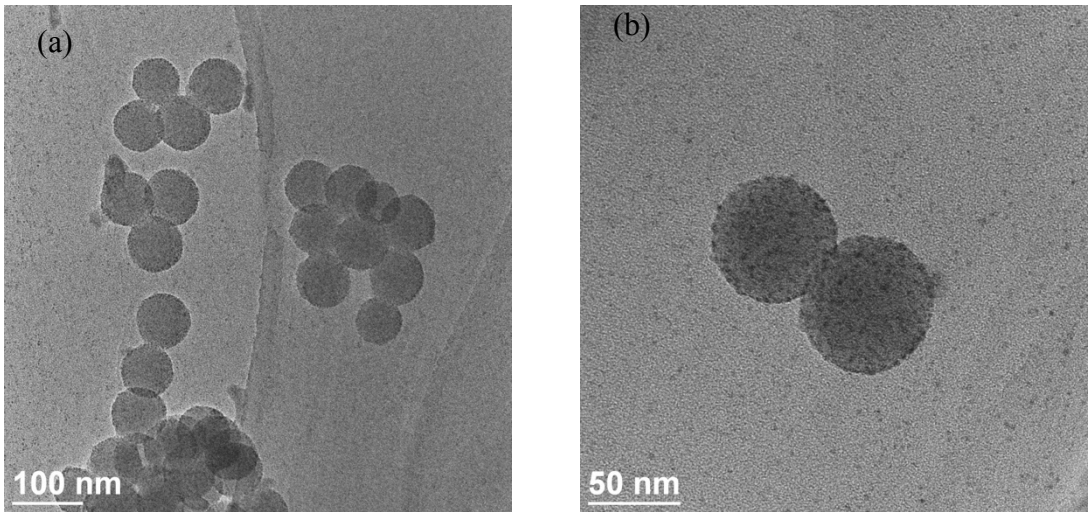

Figure 6-3. *TEM images of multiple QD carriers at (a) low and (b) high magnification.*

We further developed a technique to encapsulate two kinds of QDs in carriers. Figure 6-3 shows TEM images of the carriers containing two kinds of QDs. Such kind of multiple QD carriers can be used as thermal history sensors to extract the heating temperature and heating time of thermal events.

7: New potential materials as thermal sensors

CdSe/ZnS QDs are good thermal sensor materials covering 200 – 500 ^{o}C in air. However CdSe/ZnS QDs are not very thermally stable. For example, the CdSe/ZnS QDs are usually stored in refrigerators and the shelf-life is usually several months. Such instability would cause high measurement errors in field tests and transport problems. So we have searched other nanomaterials with high thermal stability as new thermal sensors. Gallium oxide, gallium nitride, carbon nanotubes are more stable in air. Here we synthesized these nanomaterials as potential thermal sensors.

7.1. Core-shell microspheres

Core-shell QDs are too small to investigate the mass diffusion between core and shell. In order to study the mass diffusion easier, we synthesized a kind of microscale counterpart of the core-shell QDs: core-shell microspheres.

Core-shell microspheres consist of a glass core and a metal shell. Soda lime glass microspheres were coated with metals (cobalt or nickel) by electroless plating method. The glass microspheres were cleaned in acetone and etched in diluted HF solution to produce fresh surfaces. The etched microspheres were then sensitized in a $SnCl_2$ solution and Sn^{2+} ions were absorbed on the microsphere surfaces. The sensitized microspheres were activated with a $PdCl_2$ solution. Palladium ions were reduced to catalytic nanoparticles on the microsphere surfaces during the activation procedure. The activated microspheres were then electrolessly plated in a nickel or cobalt ion containing bath at 70 – 90 ^{o}C.

Figure 7-1 shows the images of glass microspheres before and after electroless cobalt plating. The as-received soda lime glass microspheres were transparent under optical microscope (Figure 7-1a). The average diameter of the as-received microspheres was 49.1 ± 2.9 μm. After electroless plating, the microspheres were black under naked eyes. Figure 7-1b shows an SEM image of the coated microspheres. The coating was continuous on the microspheres and covered the whole surface of the microspheres. Under an optical microscope, the electroless plated microspheres were opaque and the coating was colorful, shown as the inset in Figure 7-1b. Figure 7-1c shows a FIB image of a typical cross-sectioned microsphere with cobalt coating. Cobalt continuously deposited on the surface of the glass microsphere. In addition, the coating layer was ~2 μm thick and the thickness was very uniform. In our plating experiments, the thickness of the cobalt coating was adjustable from 0.1 to 4 μm depending on the plating temperature and plating time.

EDS spectrum of the coated microspheres indicated that the coatings were consisted of phosphorus and cobalt or nickel.

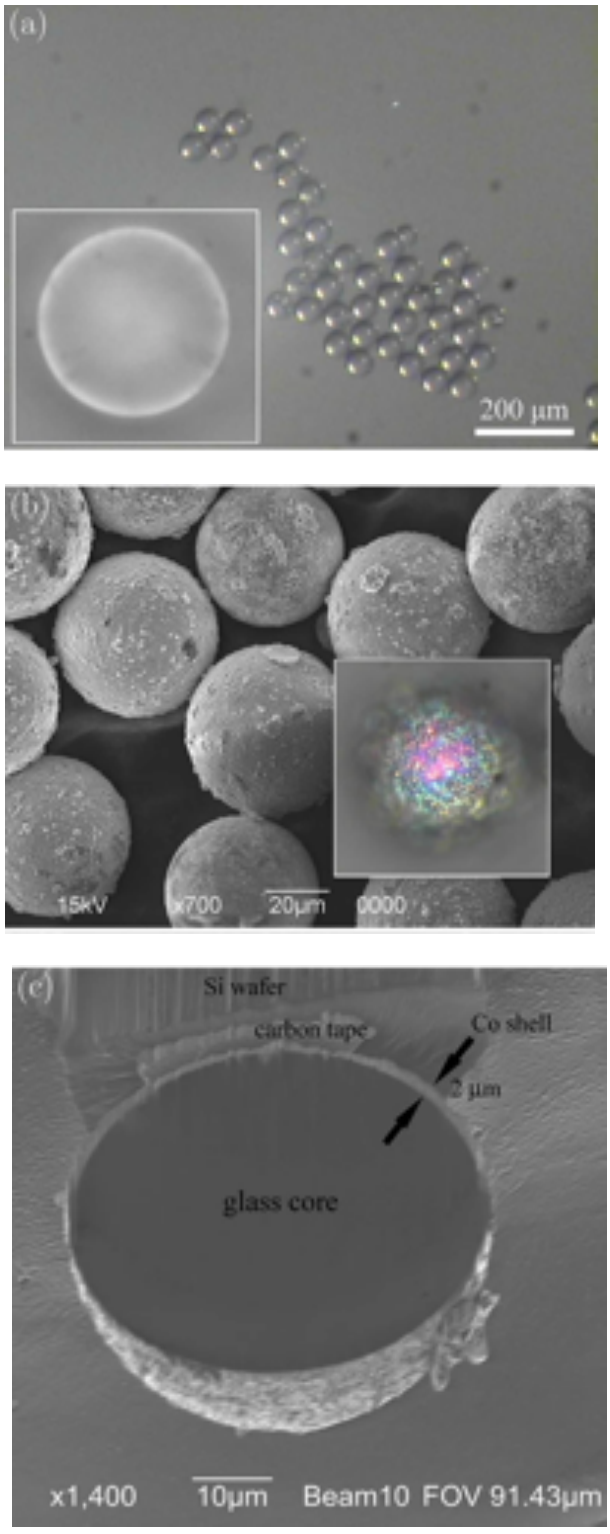

Figure 7-1. *Microspheres before and after electroless cobalt plating. (a) Optical image of as-received glass microspheres. Inset is a zoomed image of a glass microsphere. (b) SEM image of coated microspheres. Inset: optical image of a coated microsphere. (c) FIB image of a cross sectioned microsphere with coating.*

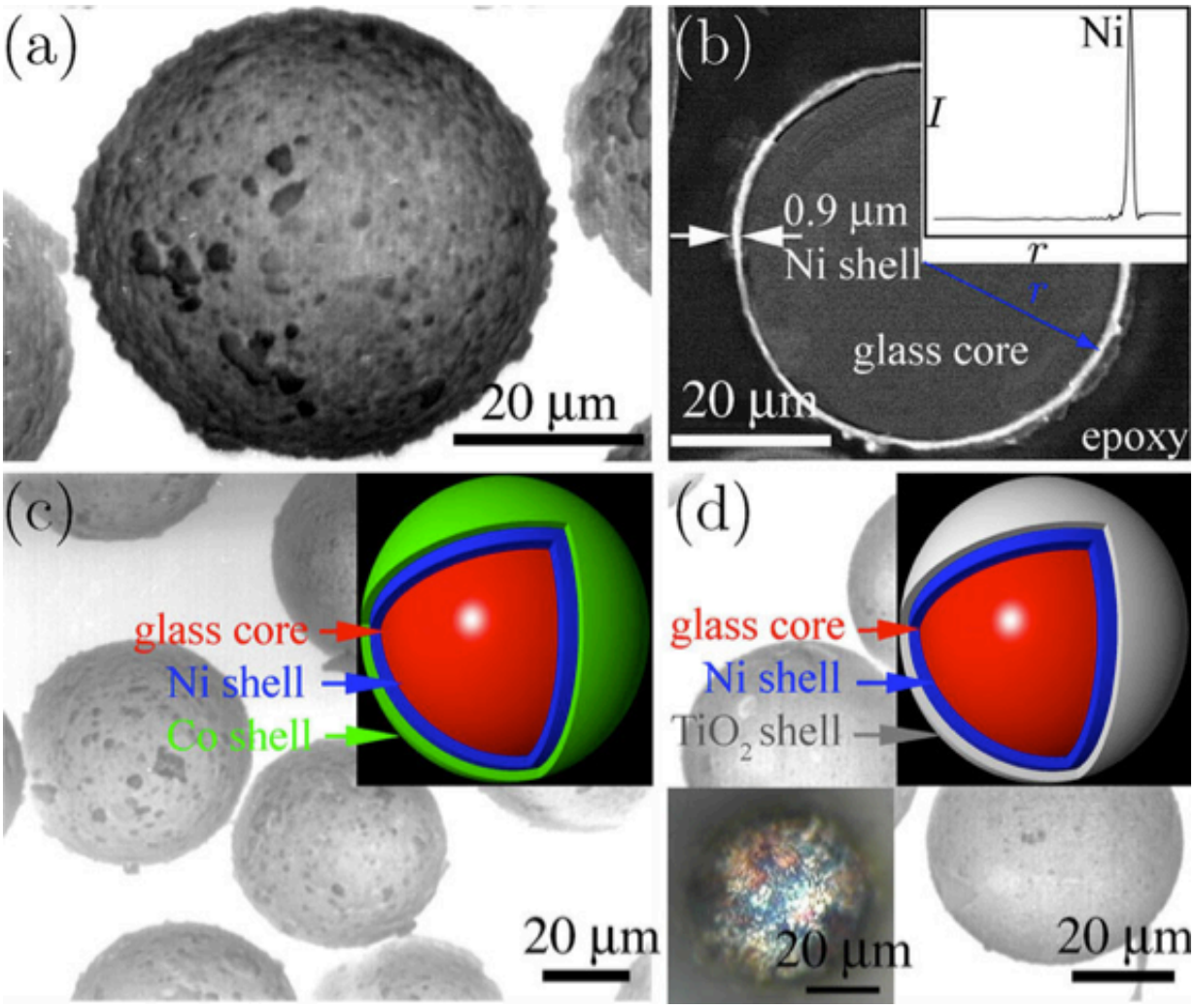

Figure 7-2. *SEM images of various coated microspheres. (a) Nickel coated microspheres. (b) Cross-sectioned microsphere with nickel coating. Inset EDS nickel linescan along the radial direction. I: EDS intensity. r: the distance from the core center. (c) Ni/Co double-coated microspheres. Inset is the core-shell-ed structure with double coatings. (d) Ni/TiO_2 double-coated microspheres. Top-right inset is the core-shell-ed structure with double-coatings. Bottom-left inset is an optical image of a Ni/TiO_2 double-coated microsphere. (e) Core-shell-ed microsphere with a thick nickel coating. (f) Optical images of Ni/TiO_2 double-coated microspheres at low magnification (top) and at high magnification (bottom) after fast annealing.*

Figure 7-2a shows an SEM image of a typical nickel coated microsphere. The surface morphology is similar to that of the cobalt-coated microspheres shown in Figure 7-1b. In order to examine the core–shell structure of the nickel coated microspheres, the nickel-coated microspheres were embedded in an epoxy and mechanically polished. Figure 7-2b shows an SEM image of a cross-sectioned microsphere coated with nickel coating. The outer diameter of the coated microsphere was 52.3 ± 0.1 µm and the thickness of the coating layer was 0.9 ± 0.1 µm. EDS line-scan of nickel (inset in Figure 7-2b) indicated the coating layer was nickel locating at the surface of the microsphere. This core–shell structure was very similar to that of

cobalt-coated microspheres shown in Figure 7-1c.

Complex double-layered core–shell structures, such as Ni/Co double coatings, were also produced by the electroless plating method. The as-received microspheres were first coated in a nickel bath. Then the nickel-coated microspheres were extracted from the nickel bath by a magnet at the plating temperature, dispersed into a cobalt solution with a same plating temperature, and electroless cobalt plated. Figure 7-2c shows an SEM image of the Ni/Co double-coated microspheres. The inset in Figure 7-2c shows the core–shell structure of the double-coated microspheres. When the process was reversed, the microspheres were coated by cobalt first, then nickel plated to produce Co/Ni double-coated microspheres. The surface morphology of the Co/Ni double-coated microspheres was similar to these of nickel-coated, cobalt-coated, and Ni/Co double-coated microspheres.

Moreover, complex metal/oxide double-coated core–shell structures, such as Ni/TiO_2 coated microspheres, were also produced by combining the electroless method with a sol-gel technique. After electroless coating and vacuum drying, the electroless-coated microspheres were coated by TiO_2 by a sol–gel technique at room temperature, forming metal/oxide double-coated microspheres. Figure 7-2d shows the Ni/TiO_2 core-shell microspheres. Compared with the metal coated microspheres, the surface of the oxide coating was smoother.

The thickness of the metal coatings can be easily controlled in the range of 0.1 - 4 μm by varying the plating time and plating temperature. If the coatings were too thick (>2 μm), the coatings sometimes debonded from the surface of the glass microspheres.

The TiO_2 coatings sometimes cracked after being heated, especially when the oxide layer was thick or the annealing rate was too fast.

7.2. Ga_2O_3 nanowires

Ga_2O_3 is a thermal stable material with bulk melting point of over 1700 ^oC. Ga_2O_3 crystalline nanowires were grown on patterned silicon substrates using the chemical vapor deposition technique to check if it is possible to be used as high temperature thermosensors.

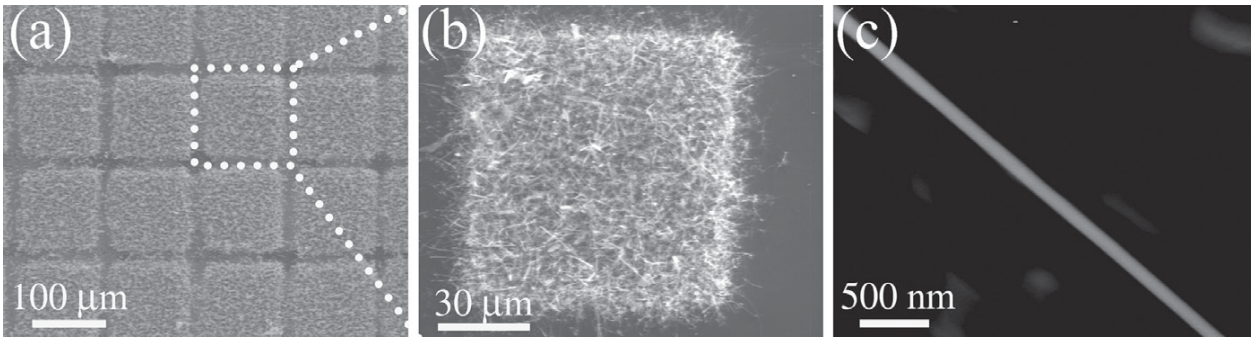

Figure 7-3. *SEM images of as-grown Ga_2O_3 nanowires on silicon substrates at (a) low (b) medium and (c) high magnification.*

Figure 7-3 shows SEM images of the as-grown Ga_2O_3 nanowires on the catalytic cobalt patterns. Low-magnification SEM (Figure 7-3a) indicated that the produced Ga_2O_3 nanowires was consisted of a series of 100 µm × 100 µm nanowire-blocks on the Si substrates. Most of these nanowires were longer than 10 µm, some even longer than 40 µm. The diameter of these nanowires was less than 100 nm. Figure 7-3c shows one typical nanowire grown on the cobalt regions. The nanowire was straight and uniform with a length of 25 µm and a diameter of about 80 nm. The surface of the nanowire was smooth.

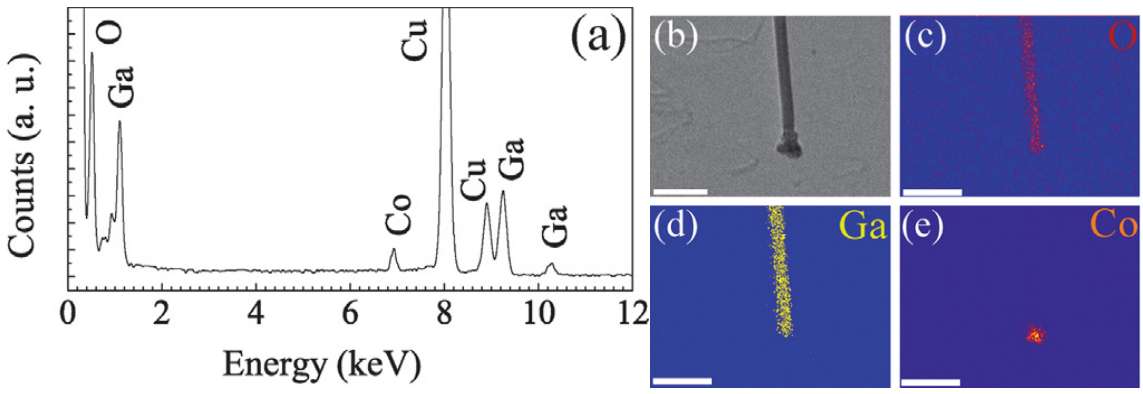

Figure 7-4. *(a) EDS spectrum of the synthesized nanowires. The copper signal comes from the TEM copper-grid. (b) Bright-field STEM image of a nanowire. EDS elemental mapping of (c) oxygen Kα, (d) gallium Kα and (e) cobalt Kα. The scale bars are 300 nm.*

The microstructure of the Ga_2O_3 nanowires was investigated on STEM. EDS spectrum of the synthesized nanowires (Figure 7-4a) indicated that the nanowires were composed of cobalt, gallium, and oxygen. In order to qualitatively study the spatial elemental distribution of these nanowires, EDS mapping was carried out on STEM. Figure 7-4b was a bright-field STEM image of a typical β-Ga_2O_3 nanowire. The nanowire was consisted of a long straight stem (up to 11 μm) with a diameter of 30 nm and an irregular tip with a 65 nm diameter. The EDS elemental mapping indicated that oxygen distributed on the entire nanowire including the nanowire tip and the nanowire stem (Figure 7-4c), gallium mainly distributed on the nanowire stem (Figure 7-4d) and cobalt mainly located at the tip of the nanowire (Figure 7-4e).

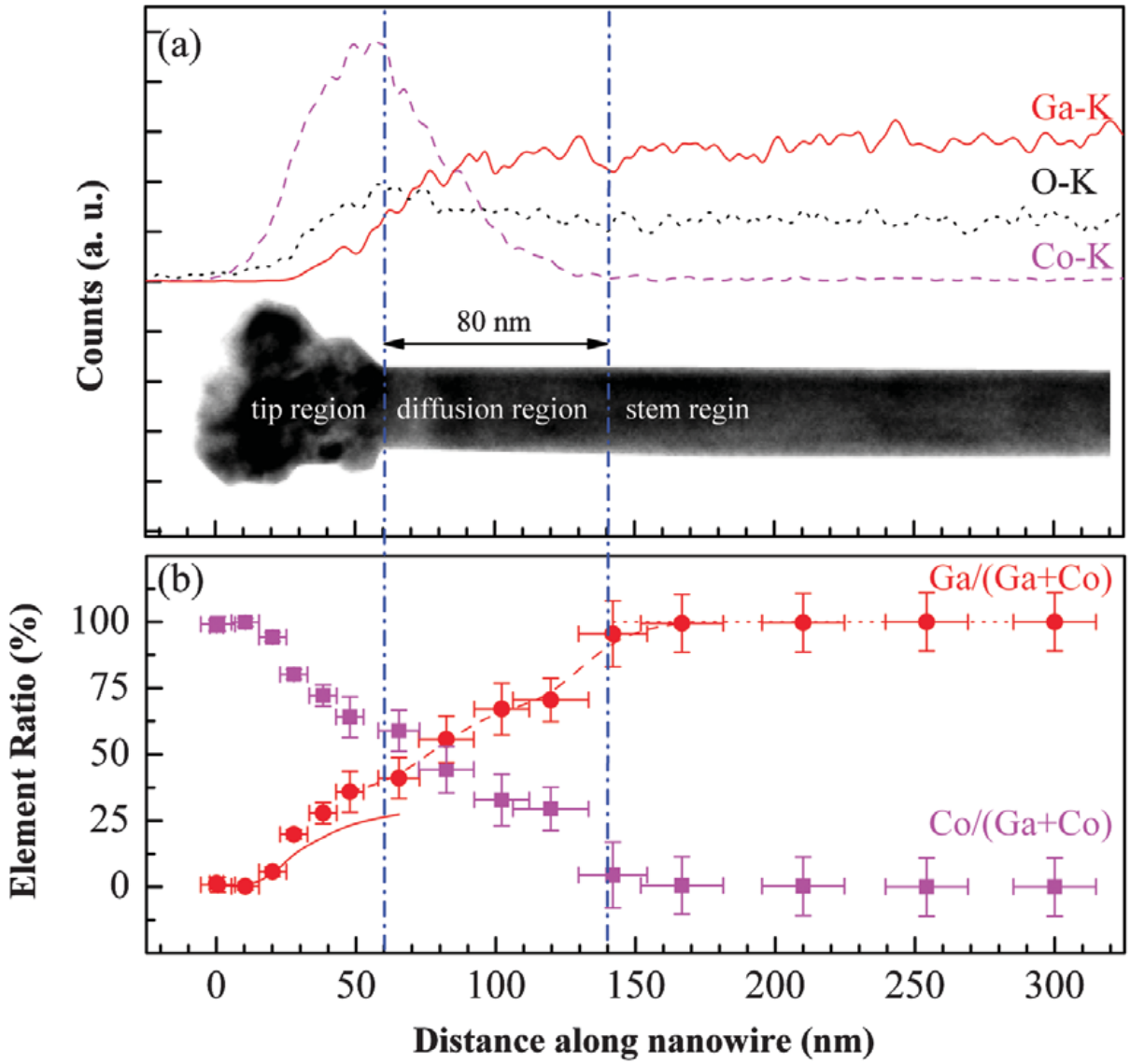

Figure 7-5. *(a) EDS linescanning along a Ga_2O_3 nanowire. EDS linescaning is measured along the white dashed line in the inset. (b) Elemental ratio of cobalt and gallium along the nanowire. A series of EDS spectra are measured along the white dashed line in (a) to calculate the Co/Ga elemental ratio. Three regions are defined based on the spatial elemental distribution: $(Co_{1-x}Ga_{2x/3})O$ tip region, $(Co_xGa_{1-x})_2O_3$ diffusion region, and Ga_2O_3 nanowire stem region.*

The entire wires were composited of three regions. Figure 7-5 shows the element distribution in the three regions. At high temperatures, the cobalt at tip regions can diffuse into stem regions to form diffusion regions. The length of the diffusion regions and the element concentration along the diffusion regions depend on heating histories. Therefore such a kind of nanowires is a potential thermosensors at high temperatures.

7.3. GaN porous microtubes

GaN is another kind of thermal stable material used at high temperatures. We synthesized nanostructured GaN to explore their potential application as thermosensors.

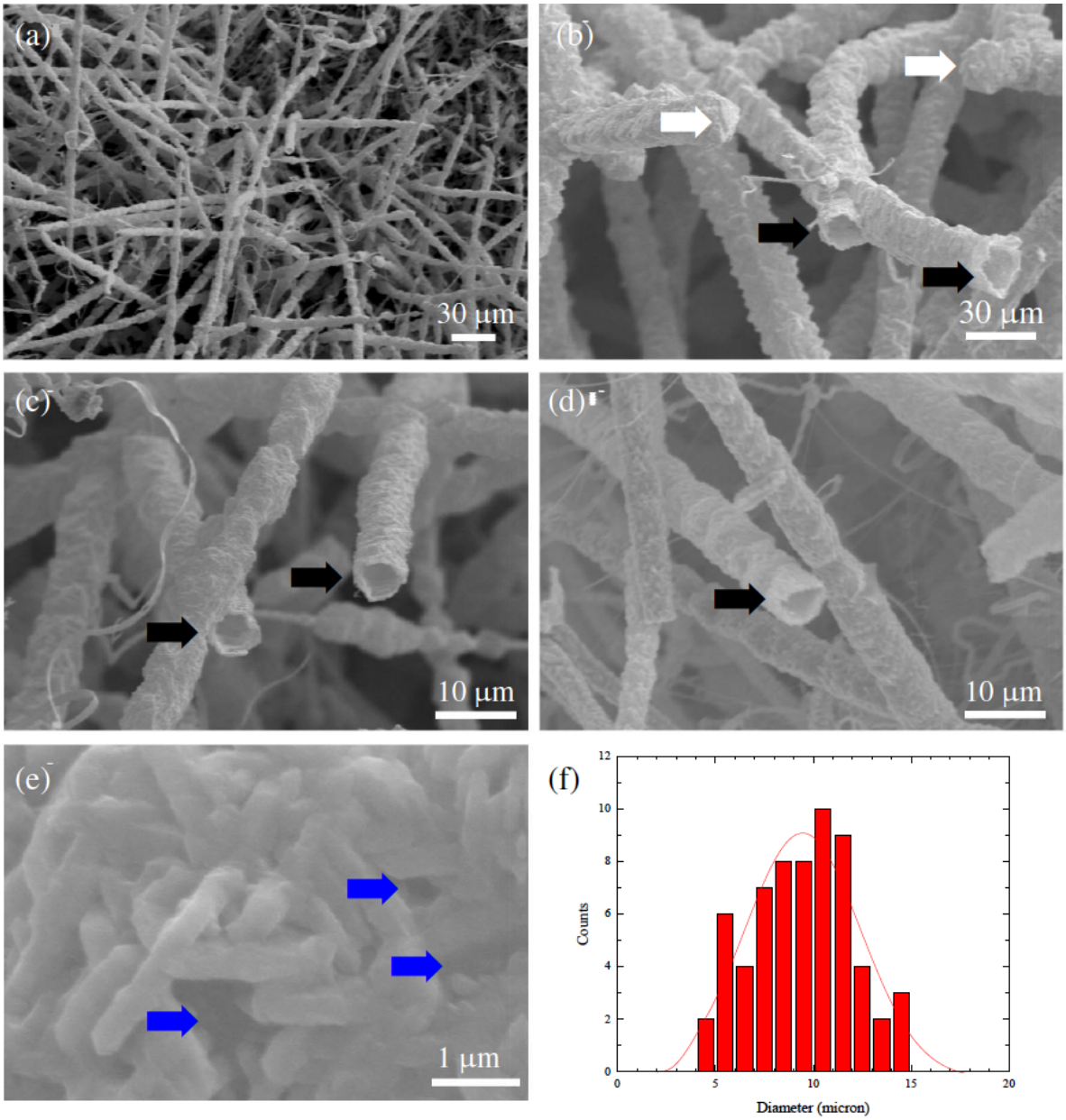

Figure 7-6*. SEM images of microtubes (a-d) grown at different regions and (e) wall surface of a microtube. White arrows mark the closed ends, black arrows the open ends, and the blue arrows the nanopores of the microtubes. (f) Histogram of microtube diameter.*

Figures 7-6a-d show SEM images of the GaN nanostructures imaged directly on the substrates. The synthesized structures were hollow. The cross-section of the microtubes was circular. The ends of most of the microtubes were open (marked with black arrows) while some were closed

(marked with white arrows). The length of the microtubes was up to 100 µm. The diameters of 85 microtubes were measured and Figure 7-6f plots the diameter distribution of these 85 microtubes. These microtubes were picked up at ten regions located within several millimeters. The diameter of the microtubes ranged from 4 µm to 15 µm with an average of 10 µm.

By observing the open ends of the microtubes, the thickness of the microtube walls was measured from fifteen microtubes, and was found to be 0.13 − 0.52 µm with an average of 0.24 µm.

High magnification SEM images (i.e., Figure 7-6e) indicated that the nanowalls of the microtubes consisted of short nanorods. Most of the nanorods were about 2 µm long and about 0.3 µm in diameter. Consequently, the nano-wall thickness was essentially 1-2 nanorods thick and were highly defective with many nano-pores.

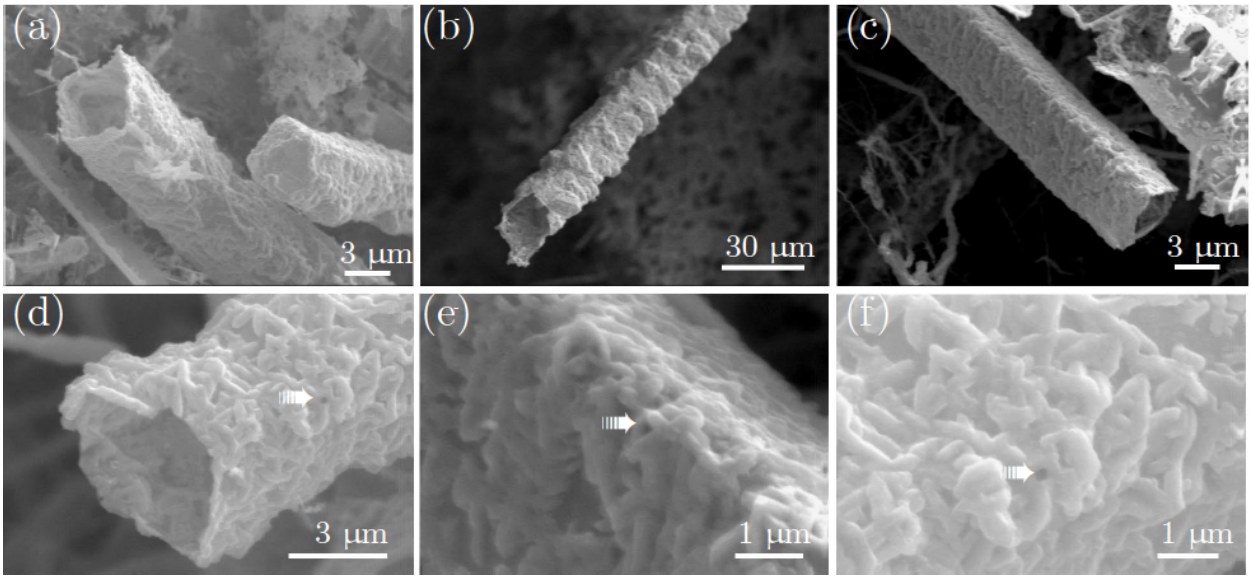

Figure 7-7*. SEM images of GaN square microtubes. (a-c) Microtubes grown at different regions. (d) End of one microtube. (e) Edge of a square microtube. (f) Enlarged surface of a microtube. White arrows mark the nanopores of the microtubes.*

Besides the circular GaN microtubes, square GaN microtubes were also synthesized by CVD method. Figures 7-7a-c show SEM images of some microtubes grown on the substrates. The synthesized structures were hollow microtubes with cross sections about 3 µm and lengths up to 100 µm. The ends of most of these microtubes were open, but some were closed (Figure 7-7a). SEM images also indicated that all tube walls were nearly equal in width (Figure 7-7a-d) and all face angles were at right angles (Figure 7-7a-e). That is, the synthesized microtubes were square in cross-section.

From the open ends of the microtubes (Figures 7-7a-d), the thicknesses of the microtube walls were found to be about 100 nm. More detailed examination indicated the walls consisted of single layer of randomly oriented nanorods (Figures 7-7d). The diameters of the nanorods were about 100 nm and their lengths were about 1 µ m (Figure 7-7d-f).

High magnification SEM images (Figure 7-7d-f) indicated that, as a result of the random packing of the nanorods, the thin walls of the microtubes were porous, resulting in these walls having very large surface areas. Some nanopores, indicated by the arrows, in these walls are noted by the arrows in Figures 7-7d-f.

7.4. Coated CNTs

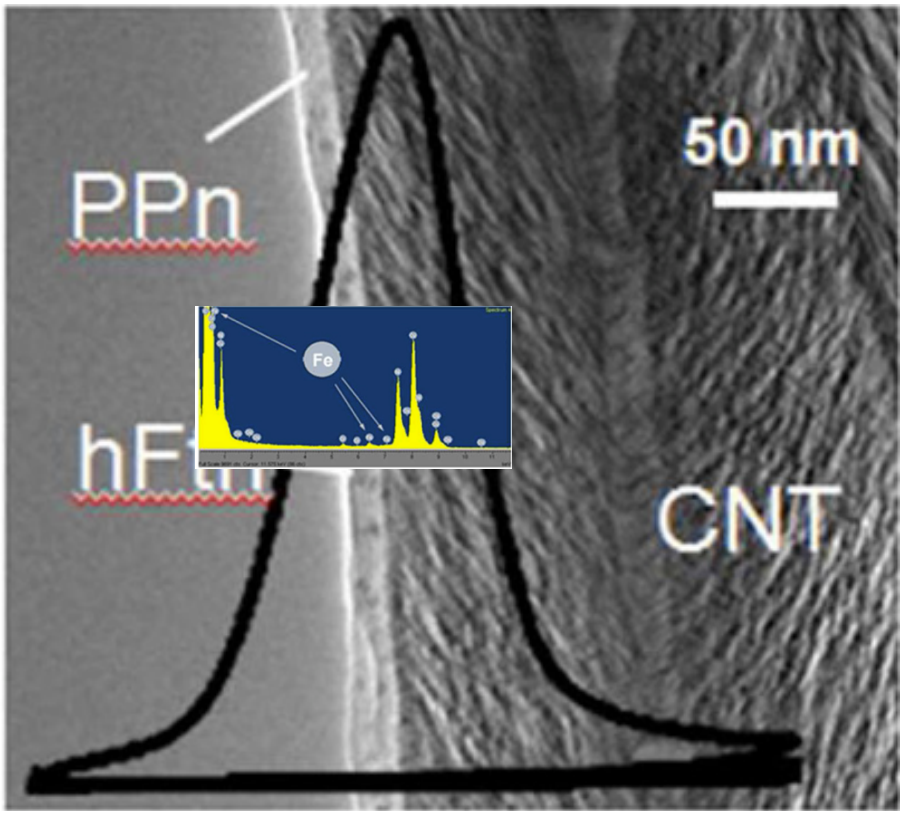

Figure 7-8*. TEM image of CNT/PPn structures. Inset: EDS spectrum.*

Besides the spherical core-shelled structures, cylindrical core-shell structures are also potential sensors based on same measurement and readout strategy. Here we chose carbon nanotube (CNT) as core and polyphenol (PPn) as shell.

CNTs were synthesized by plasma enhanced chemical vapor deposition. PPn was coated on CNT by electropolymerization method. During the coating, CNTs were used as the working electrode in a standard three-electrode recording system. A platinum wire served as a counter electrode and AgCl coated Ag foil was used as a reference electrode. The buffer contained PPn. Cyclic voltammetry was performed with a voltage scanned from 0 V to 0.9 V at 100 mV/s, and the thickness of the PPn coating was controlled by the number of running cycles.

Figure 7-8 shows a TEM image of a CNT/PPn core-shell structure. The PPn coating was compact, pin-hole free, and 10 - 20 nm thick. Its consistency and stability were indicated by the

electrode impedance and leakage currents.

Black dots in the PPn coating were iron-based compounds with diameter of 5 nm. Such nanodots would work with PPn to record temperature history.

8 SUMMARY

8.1. Project

Significant progresses have been made in using quantum dots as temperature history sensors. We obtained quantitative relationship between heating temperature/duration and PL properties of four kinds of QDs. The relationships were used to fabricate and characterize thermal history sensors. Thermal histories with or without time delay can be extracted from the PL spectra of mixed CdSe/ZnS QDs. The experimental data have shown that we have achieved our goals in laboratories.

The microstructures of the QDs were examined before and after heating. The physical mechanism was established to explain the PL properties under high temperatures.

In addition, ultra-thin, oxidization resistant, amorphous Al_2O_3 supporting films are deposited on conventional TEM grids by atomic layer deposition. The amorphous films with 2 nm thickness are mechanically stable up to 600 °C in air and over 900 °C in vacuum, suitable for high-temperature HRTEM and high-temperature SAED. The coated TEM grids can withstand higher temperature when the thickness of Al_2O_3 supporting films increases.

Several kinds of nanomaterials have been synthesized. These nanomaterials are thermally stable in air and are potential nanosensors.

8.2. Personal supported

At MIT: Prof. Gang Chen supervised the work. Dr. Taofang Zeng, research scientist, carried out thermal diffusion theory. Dr. Nitin Shukla, postdoc, carried out photoluminescence experiment and analysis of the 1st kind of QDs. Yi He, graduate student, carried out mass diffusion of core-shells.

At BC and UH: Prof. Zhifeng Ren supervised the work. Dr. Yucheng Lan, research assistant professor, carried out TEM and photoluminescence experiments. Dr. Dong Cai, research associate professor, and Mr. Zhen Yang graduate student carried out coating of QDs. Mr. Hui Wang, researcher, carried out size analysis of CdSe QDs.

8.3. Honors/Awards

G. Chen was named Carl Richard Soderberg Professor of Power Engineering at MIT in 2010, and was elected to the National Academy of Engineering. Zhifeng Ren was named M. D. Anderson Chair Professor at University of Houston in 2013. Yi He was awarded a doctorial degree from MIT in 2012.

2010-2013 Journal Publications

1. Zhen Yang, Lulu Zhang, Lu Ren, Yucheng Lan, Jeffrey H. Chuang, Z. F. Ren, Thomas Chiles, and Dong Cai, "Artificial Interface in Electropolymerized Protein Imprint", (2013) (prepared).
2. Yucheng Lan, *et. al.*, "Determination of Thermal History by Photoluminescence Change of Core-Shelled Quantum Dots Going Through Heating Events" (2013) (submitted).
3. Yucheng Lan, Feng Lin, Hui Wang, Zhifeng Ren, and Martin A. Crimp, "Spontaneously Assembled Gallium Nitride Macroscopic Tubular Structures and Quantum Confinement Effects" (2013) (submitted).
4. Yucheng Lan, Hui Wang, Bed Poudel, Qing Jie, and Zhifeng Ren, "Temperature Sensing Based on Melting Point of Nanoparticles and Applications on Heating Transmission Electron Microscopy" (2013) (submitted).
5. Yucheng Lan, Hui Wang, Feng Lin,_Zhifeng Ren, Martin A. Crimp, "Nanoporous Gallium Nitride Square Microtubes", *Journal of Material Science* (2013) (accepted).
6. Yucheng Lan, Yalin Lu, and Zhifeng Ren, "Mini Review on Photocatalysis of Titanium Dioxide, Nanoparticles and Their Solar Applications", *Nano Energy* (2013) (in press) (DOI: http://dx.doi.org/10.1016/j.nanoen.2013.04.002).
7. Hui Wang, Yucheng Lan, Jiaming Zhang, Martin A. Crimp, and Zhifeng Ren, "Growth Mechanism and Elemental Distribution of β-Ga_2O_3 Crystalline Nanowires Synthesized by Cobalt-Assisted Chemical Vapor Deposition", *Journal of Nanoscience and Nanotechnology*, Vol. **12**, No. 4 (2012) pp. 3101-3107.
8. Hui Wang, Yucheng Lan, Martin A. Crimp, C. L. Lin, Nitin Shukla, Taofang Zeng, D. Z. Wang, K. C. Li, Zhifeng Ren, and G. Chen, "Paramagnetic microspheres with core-shell-ed structures", *Journal of Materials Science*, Vol. **47**, No. 16, (2012) pp. 5946-5954.
9. Yucheng Lan, Yang Wang, and Z.F. Ren, Physics and applications of aligned carbon nanotubes, *Advances in Physics*, Vol. **60**, No. 4 (2011), pp. 553-670.
10. Y. C. Lan, Hui Wang, Dezhi Wang, Gang Chen, and Z. F. Ren, "Grids for Applications in High-Temperature High-Resolution Transmission Electron Microscopy", *Journal of Nanotechnology* **2010** (2010), 279608.

BOOK

11. Zhifeng Ren, Yucheng Lan, and Yang Wang, (BOOK) *Aligned carbon nanotubes: physics, concepts, fabrication, and devices* (Springer, 2012) (ISSN: 1434-4909, ISBN: 978-3-642-30489-7).

Conferences

12. Nitin C. Shukla, Gang Chen, Taofang Zeng, Yucheng Lan, and Zhifeng Ren, Study of CdSe/ZnS Quantum Dots for Thermal History Sensing Application. 2011 MRS Fall Meeting November 28 - December 2, 2011 Hynes Convention Center, Boston, MA.
13. Nitin Shukla, Gang Chen, Zeng Taofang, Yucheng Lan and Zhifeng Ren, Nanocrystals for Thermal History Recording, 2011 MRS Fall Meeting November 29 - December 3, 2010 Hynes Convention Center, Boston, MA.

DEPARTMENT OF DEFENSE

DEFENSE THREAT REDUCTION
AGENCY
8725 JOHN J. KINGMAN ROAD
STOP 6201
FORT BELVOIR ,VA 22060
ATTN: S. PEIRIS

DEFENSE TECHNICAL
INFORMATION CENTER
8725 JOHN J. KINGMAN ROAD,
SUITE 0944
FT. BELVOIR, VA 22060-6201
ATTN: DTIC/OCA

DEPARTMENT OF DEFENSE
CONTRACTORS

EXELIS, INC.
1680 TEXAS STREET, SE
KIRTLAND AFB, NM 87117-5669
ATTN: DTRIAC